ABSTRACT

WHITE, REBEKAH DALE. Inferring the Microstructural Properties of Cortical Bone from Ultrasound Attenuation. (Under the direction of Alen Alexanderian.)

Mathematical models are widely used to represent physical and biological phenomena with the goal of better understanding such systems. Additionally, these models along with data can be used to formulate and solve inverse problems allowing us to infer specific information about the systems themselves. This approach is especially useful when the information we seek cannot be easily ascertained from experimentation. In this dissertation we use these mathematical tools to develop techniques for characterizing the microstructure of heterogeneous cortical bone. This is of interest as a quantitative characterization of cortical bone can aid in identifying and diagnosing degenerative bone diseases such as Osteoporosis. We focus on using ultrasonic attenuation data to infer the microstructural properties, pore size and pore density, thus providing a non-invasive, non-ionizing way of characterizing bone.

This work is conducted in stages, where every progression represents a more realistic version of the problem formulation, with the ultimate goal being able to infer microstructure *in-vivo*. The first phase involves determining if ultrasonic attenuation data is dependent upon the microstructural parameters of interest, pore size and pore density. This is necessary to establish in order to use ultrasound attenuation to infer microstructural properties. In this phase, we numerically generate data using simulated 2D monodisperse (pores of the same size) cortical bone-like structures. We choose an empirical relationship between frequency and attenuation that is based on the trends in simulated attenuation data. This results in a phenomenological mathematical model for attenuation. We show that model parameter estimates resulting from solving an inverse problem allow use to determine low, medium, or high porosity levels in the 2D cortical bone-like samples. The methods we use involve formulating and solving an Ordinary Least Squares inverse problem, performing local sensitivity analysis, calculating standard errors, and performing linear regression. This stage provides proof-of-concept for the more realistic problem formulations we discuss next.

In phase two of the work, we use two physics-based scattering attenuation models, the Independent Scattering Approximation (ISA) and the Waterman Truell (WT) model, to represent attenuation in heterogeneous cortical bone. These models are nested versions of one another, with the WT model being a higher order model in comparison to the ISA. Since both models are explicitly dependent upon both pore size and density, we can formulate and solve an inverse problem to directly estimate these parameters. We use more realistic 3D monodisperse cortical bone-like structures and numerically generate data using a Finite Difference Time Domain package. In the second phase of the work, we validate the use of both scattering models to represent attenuation in cortical bone as well as to infer microstructural properties of simulated samples.

The third phase of work builds on the second phase, but considers the more realistic problem formulation where the pores of the bone vary in size (polydisperse). This mimics the structure of real cortical bone and allows us to use ultrasound attenuation data gathered from *in-vitro* cortical bone samples taken from human cadavers. In this phase, we must reformulate our attenuation models to represent these polydisperse samples. We use a probabilistic approach and illustrate several ways this can be done. In this phase of work, the quantity of interest is the Probability Density Function (PDF) on pore size in the bone sample. This will allow us to better quantify osteoporosis levels in comparison to having only an average pore size estimate. Note that the inverse problem of estimating a PDF involves an infinite dimensional optimization problem. Thus, we use the Prohorov Metric Framework to make the inverse problem tractable. We implement regularization functions to address the ill-posed nature of the inverse problem. In this work, we show that we can predict attenuation in real cortical bone using these polydisperse models. Furthermore, using micro CT imaging to validate our results, we show we can accurately estimate the true PDF on pore size within these samples. Overall, the techniques provided in this work provide the foundation for solving the problem *in-vivo*.

Inferring the Microstructural Properties of Cortical Bone from Ultrasound Attenuation

by
Rebekah Dale White

A dissertation submitted to the Graduate Faculty of
North Carolina State University
in partial fulfillment of the
requirements for the Degree of
Doctor of Philosophy

Applied Mathematics

Raleigh, North Carolina

2021

APPROVED BY:

_____   _____
Hien Tran   Mansoor Haider

_____   _____
Marie Muller   Alen Alexanderian
                                                                   Chair of Advisory Committee

DEDICATION

To my parents for their support and love.

BIOGRAPHY

Rebekah White was born in Johnson City, TN. She received her B.S. in Mathematics from East Tennessee State University in December of 2015. The following year she began a PhD program in Applied Math at North Carolina State University. She worked with the late Dr. H.T. Banks for her first four years in the program. Following this she worked with Dr. Alen Alexanderian.

ACKNOWLEDGEMENTS

TABLE OF CONTENTS

LIST OF TABLES

LIST OF FIGURES

CHAPTER

1

INTRODUCTION

Quantifying physical or chemical properties of heterogeneous materials is of broad interest in geological, medical, and engineering applications. A major goal is often to answer questions regarding the structural or chemical composition of media for the purpose of monitoring material changes or identifying degradation. Non-invasive interrogation techniques have been widely used to characterize media such as cements and ceramic matrix composites, living tissues, and even geological samples [8, 45, 86, 91]. Frequently, the use of non-invasive and non-destructive interrogation tools is of interest to provide routine screening capabilities. This dissertation focuses on a specific biomedical application. Namely, we aim to develop methodology for inferring the microstructural properties of human cortical bone through the use of non-invasive and non-ionizing ultrasonic wave interrogation.

1.1 Motivation

The main motivation of the research in this dissertation is providing a quantitative tool to characterize the microstructure of cortical bone for the purpose of characterizing stages of osteoporosis in patients. Osteoporosis is a bone disease that degrades the cortical bone matrix, thus increasing patient susceptibility to fracture [38, 56]. The disease does so by increasing the size and density of the pores in the cortical bone [3, 80]. Approximately 70% of appendicular bone loss is cortical bone, making it the primary focus of our research [2]. To properly characterize the progression of the disease, one must be able to infer the microstructure of the bone. This disease affects large percentages of the population and on average results in 20% of men and 33% of women over the age 50 experiencing osteoporotic fractures [69, 70]. However, early diagnosis

and treatment can reduce the risk of osteoporosis related injuries [41]. This in turn requires routine patient screenings, which are only feasible with an approach that utilizes non-invasive, non-ionizing, and relatively cheap technology. As we will discuss in detail in Chapters 2, 3, and 4, current approaches are unable to provide this. Therefore, a new approach for characterizing the microstructural properties of cortical bone is needed. The proposed approach could be broadly applied the characterization of heterogeneous media, making it of interest in a variety of fields.

1.2 Previous Work

Here, we provide a brief review of literature relevant to this dissertation. We first discuss broadly the use of ultrasound interrogation to characterize heterogeneities. We then discuss some background for the physics-based models employed in Chapters 3 and 4. Lastly we discuss general schemes for inverse problems and how they relate to this work.

Although we are focused on quantifying cortical bone porosity using ultrasound attenuation, previous works have made use of ultrasound for inferring material properties in a variety of media. Geological research and oceanography readily employ ultrasound as a means of inference [51, 77, 100]. An interesting application analogous to our work includes the use of multiple scattering acoustic waves to estimate the density of fish in a shoal [100]. Rather than using the attenuation feature, this work uses information regarding the coherent backscattering of the wave and the mean free path (average distance between two scattering events) to characterize fish density. An example of the use of ultrasonics in geological applications includes using wave measurements to estimate the thickness and mechanical properties of ice sheet layers [77]. That work does not focus on wave scattering, as the waves are traveling through solid sheets of ice. Rather, the model for these so called Lamb waves (waves propagating in solid plates) determines the frequency-dependent wavenumbers. Whether dealing with geological samples or materials such as concrete, often times acoustic waves are used to identify sources or cracks, rather than evaluating characteristics of the heterogeneities. For example, the work [51] uses acoustic waves as a form of non-destructive evaluation of concrete damage in the containment walls in nuclear power plants.

In particular, the characterization of cements and concrete materials using ultrasonic attenuation share many similarities to the efforts of this work. The multiple scattering of acoustical waves has been used to characterize air voids in cement [86]. The work of [54] extends this work by considering samples with small-size and large-size air void ranges. In the aformentioned work they solve an inverse problem to estimate the parametric density functions for the discrete air void size, which are given by normal or log-normal distributions.

Similar approaches to those taken to evaluate concretes are taken in biological applications. Specifically, the work [78] studying trabecular bone suggest that microstructural parameters can be obtained from ultrasonic measurements. Trabecular bone differs significantly from cortical, in that the fluid filled pores allow for wave attenuation, while the solid bone matrix acts as scatters.

Multiple scattering ultrasound waves have also been used to investigate lung diseases, where here the microstructure is characterized by the scattered mean free path [45]. Classical approaches to diagnosing osteoporosis use what is known as Bone Mineral Density (BMD) evaluation to characterize osteoporosis. Established approaches using Quantitative Ultrasound empirically relate measured sound velocities and attenuation values with BMD and fracture risks [52, 63, 96]. Other popular routes of investigation include mathematically modeling the material properties, such as elasticity, in order to solve an inverse problem. These material model parameters can then be empirically related to properties such as porosity. This approach was taken in [22]. For a thorough background of Quantitative Ultrasound (QUS) to asses cortical bone see the review [53].

An underlying component in the various applications where ultrasound is used to infer material properties is the mathematical models representing wave propagation. Here, we discuss previous work related specifically to the physics-based mathematical modeling of ultrasonic attenuation. Ultimately, the goal is to model ultrasonic attenuation in a heterogeneous medium, which results from both scattering when the wave hits inclusions and absorption in the medium. In this work, the pores of the cortical bone act as inclusions or scatterers. The solid bone matrix, which is assumed to be isotropic and homogenous, is where the absorption occurs. We do not consider absorption within the fluid filled pores of the bone. Therefore, we aim to mathematically characterize a plane stress wave as it propagates through the heterogenous medium.

To begin, we consider the attenuation due to absorption. Mathematical derivations that result in equations representing the energy loss due to absorption in the matrix are given in [16, 17, 20]. To address the attenuation due to scattering, we rely on classical analysis given in [50, 64, 109, 117]. In 1955, [117] established the mathematical model for the scattering of a plane longitudinal wave by a spherical obstacle in an isotropically elastic solid. This work provides the mathematical derivation to determine quantities such as the scattering cross section for a spherical scatterer and is a first step towards solving the more complicated problem of multiple scattering. Addressing multiple scattering behavior followed in 1961 with the work of Waterman and Truell [109]. They determined that the behavior of the scattering medium, characterized by the complex wavenumber, can be determined explicitly by the number of scatters per unit volume and the individual scattering amplitudes for a single scatter of a fixed size given by radius r. The work [109] also provided a theoretical extension for determining the complex wavenumber when one removes the restriction of having identical scatters. There, a statistical approach is used to account for any number of distributed parameters (e.g., pore size, etc.), where an average far-field amplitude is calculated by taking the expected value with respect to the probability density functions of the distributed parameters. The work [58] also addresses what is referred to as distributed particle size. A theoretical forward model for total scattering cross section is given by taking an expectation with respect to a Probability Density Function (PDF) on on pore diameter. This approach is similar to the approaches taken in our work to formulate polydisperse models.

An important result of scattering theory is that the statistical average of the wavefield follows the Dyson equation [73]. Because the multiple scattering terms in Dyson's equation (i.e., the effective wave number representation) are written perturbatively, the order of the scattering model then depends on the order of the terms included. Including only the first order terms results in the Independent Scattering Approximation (ISA). Including the first and second order terms results in the Waterman Truell (WT) Model. Both models are considered in this work. Previously, the ISA has been used to model attenuation in trabecular bone [55, 72]. Additionally, the ISA has been used for wave propagation in a variety of media, such as cement [86], water with metallic rods acting as scatterers [42] as well as soft materials with magnetic fields [32]. The WT model has been used with soft 3D acoustic metamaterials [31].

In addition to the mathematical models for ultrasonic wave attenuation, an inverse problem formulation is also required to infer material properties. Here, we review approaches taken to solve inverse problems similar to the ones formulated in this dissertation. In general, there exist many ways to approach solving an inverse problem. When the aim is to estimate scalar or vector quantities of interest, frequentist and Bayesian approaches have been extensively and successfully applied to problems in physics and biology [12, 97]. In addition to model parameter estimates, these frameworks allow us to perform uncertainty quantification, providing information regarding our confidence in the estimates. When solving inverse problems (as in Chapter 4) where one aims to estimate a probability measure, one can employ a variety of approaches [10, 13]. For instance, one could aim to estimate the first and second moments of the corresponding distribution. However, this makes significant assumptions regarding the form of the probability distribution. Because our aim is to characterize osteoporosis in terms of the probability density on pore size, such an approach would be too restrictive. Thus, our aim is to nonparametrically estimate the probability measure. Although it is possible to formulate an appropriate Bayesian approach to such an inverse problem, there are certain challenges that arise. These include proper specification of the prior in order to satisfy inherent constraints. Additionally, computational issues arise as one cannot impose commonly used MCMC techniques directly in this infinite-dimensional setting [35, 39]. In this dissertation, we employ a frequentist approach under the Prohorov Metric Framework (PMF) [5, 84] to formulate and solve the inverse problem posed in Chapter 4. This approach has been widely used in biological applications where aggregate data is considered and population level parameters, given by random variables with associated PDFs, are estimated [6, 7, 9, 11, 14]. There do exists other approaches to nonparametric inverse problems, such as data-consistent inversion [33]. However, these are employed when the experimental data is given as a probability measure itself. Overall, the choice of inverse problem formulation depends heavily on the form of the mathematical model, type of data collection, and goal of the inverse problem.

There have been a number of previous effort on the use of ultrasound for characterizing material properties that involve formulating and solving inverse problems. Namely, [86] showed that ultrasonic attenuation could be used to characterize the entrained air voids in cement paste. Here, the ISA model and was used to estimate the average radius of the spherical air void and the

volume fraction within the cement. Additionally, the work of [54], which aimed to characterize air voids in concrete, used an inversion algorithm to estimate the parametric form of a PDF (i.e., the mean and variance parameters of the distribution). However, only discrete scatterer sizes were considered. Another work making use of inverse problems is that of [22], which examines cortical bone thickness and porosity using quantitative ultrasound (QUS). Their approach differs from ours in several ways. The ultrasonic parameter of interest in [22] is wave velocity, which is used to estimate material properties via a genetic algorithm optimization scheme. These estimated material properties are then related to porosity and bone thickness levels via regression. In contrast, our approach directly estimates the microstructural properties of interest, as there exists an explicit dependence on them in our attenuation model.

1.3   Approach

The research in this dissertation is done in stages, each progression representing a more realistic problem formulation, with an overarching theme of formulating and solving inverse problems to estimate microstructural properties. These inverse problems use some combination of attenuation data and mathematical modes for ultrasound attenuation. This general theme is depicted in Figure 1.1.
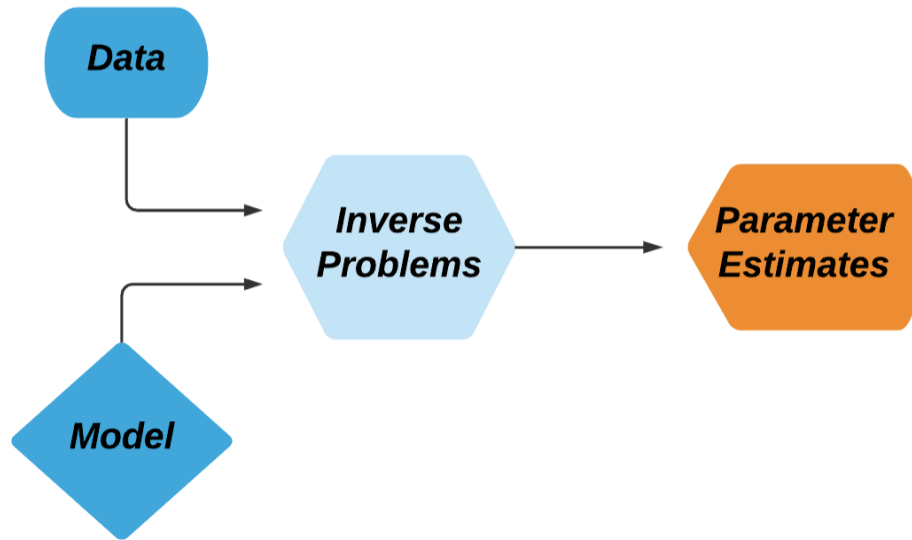
Figure 1.1 Diagram depicting how our approach utilizes experimental data and mathematical models to formulate and solve inverse problems resulting in microstructural parameter estimates

In each of the three phases of this work, we consider different cortical bone or cortical bone-like structures, mathematical models for ultrasound attenuation, and attenuation data. Thus, we

have different inverse problem formulations and results in each phase. Although fundamentally different, these phases do build on one another, each establishing proof-of-concept for the next, more realistic problem formulation. The phases of this work are outlined in Figure 1.2.
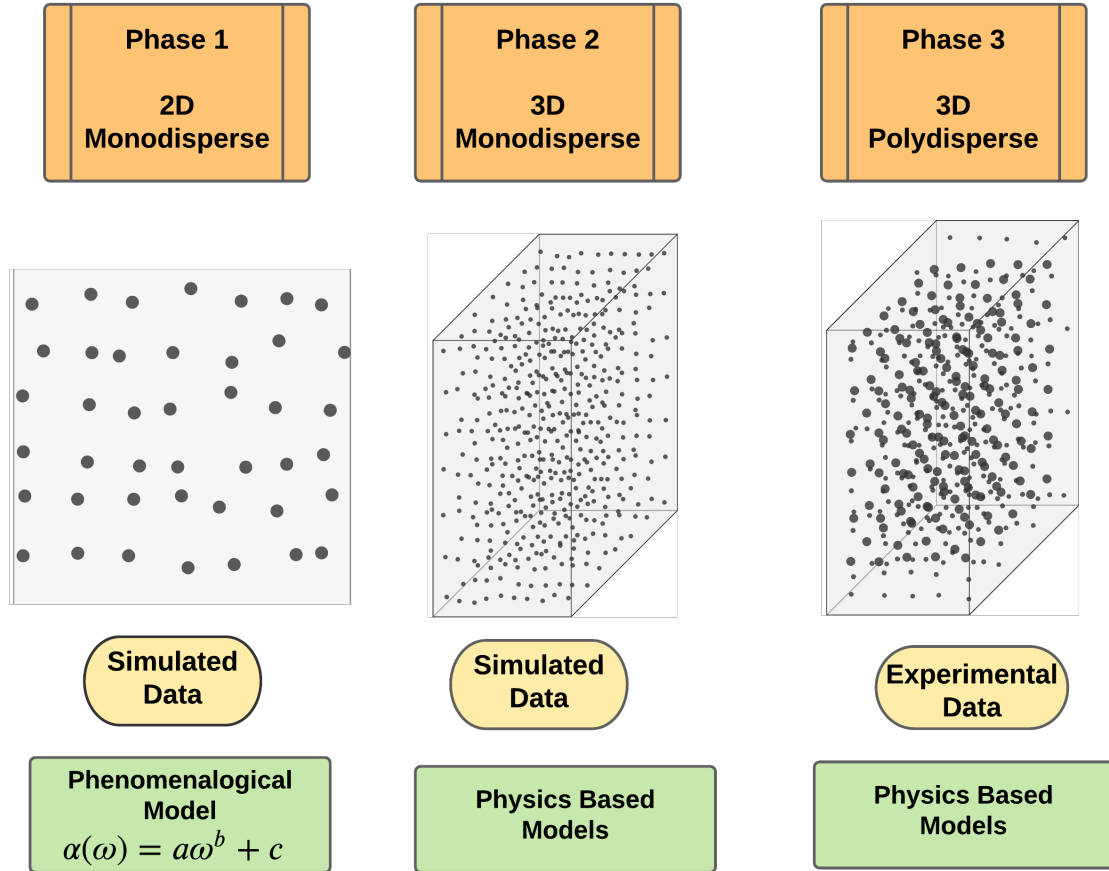
Figure 1.2 Diagram illustrating the three phases of this work. This includes the structures considered, the type of data used, and the mathematical model employed. In the structures, the dark circles/spheres represent the pores of the cortical bone and the light gray represents the solid bone matrix

In phase 1 of this work, we consider simplified, 2D cortical bone-like structures that are monodisperse—all pores are of the same fixed size. These structures are used to numerically generate attenuation data using a Finite-Difference Time-Domain (FDTD) package. Here, we also use a phenomenological mathematical model, known as the power law model. This was chosen simply because it represents the trends in the data, not because of any underlying physics. The goal of this phase is to establish that attenuation is dependent upon microstructure—defined by the pore radius r and density n_s—which is an important first step in validating our approach. We use inverse problems to do so by showing that the model parameter estimates, determined

by solving an OLS inverse problem, differ in relation to the pore size (r) and density (n_s) of the samples.

In the first phase of work, we established that attenuation data varies with changes in microstructure. The goal for the second phase of work is to determine a mathematical model for attenuation that is explicitly dependent upon the microstructural parameters of interest. This is referred to as a physics-based model. Here, we are modeling the loss of wave amplitude, which results from two sources, absorption in the solid bone matrix and scattering as the wave hits the pores of the bone. To model the contributions due to scattering, we borrow two models from classical scattering theory, the ISA and the WT models. These models are nested versions of one another, differing in the order of scattering they represent. The ISA models first order multiple scattering where a wave cannot revisit a pore/scatterer it has already visited. The WT models second order multiple scattering, where a wave can revisit a pore or scatterer it has already hit. This is depicted in Figure 1.3.
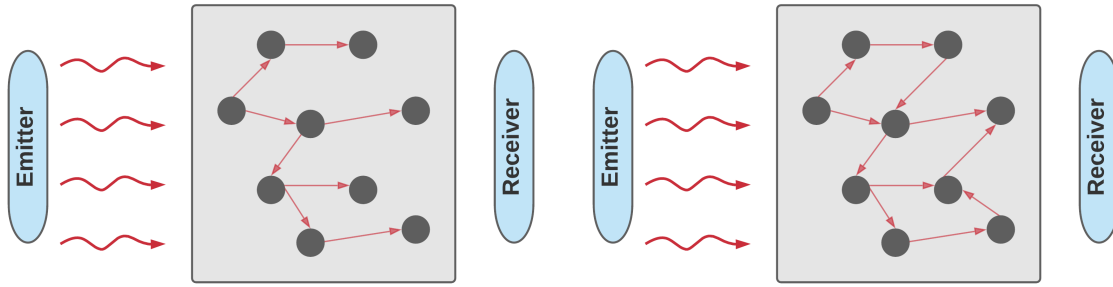
Figure 1.3 Visual comparison of the two physics-based models considered in this work. The Independent Scattering Approximation (Left) and the Waterman Truell (Right)

The main goal in the second phase of this work is to establish the use of one or both of these models for the purposes of 1) predicting attenuation in cortical bone and 2) estimating the microstructural properties. In phase two we consider 3D monodisperse structures and again simulate attenuation data using an FDTD package. Furthermore, we only consider attenuation due to scattering in this phase. We then aim to directly estimate the pore size (r) and density (n_s) using the physics-based model in our OLS inverse problem. Using asymptotic theory we can then answer questions regarding the confidence levels in these parameter estimates.

In the final phase of this work we aim to use experimental data taken from the femurs of human cadavers. However, differing from previous work, the pores in human bone are not all of the same size (monodisperse). Although one could still solve an inverse problem using the previously established models, this would amount to estimating an average pore size in the human samples. We, however, are interested in more information than the average pore size. Thus, we first aim to reformulate the ISA and WT models to represent polydisperse structures,

where pores are given by a statistical distribution. Here, the microstructural information we seek to estimate is the associated PDF on pore size ($\ell(r)$). Then our second goal is to formulate an inverse problem that allows us to nonparametrically estimate this PDF. Although one could impose a parametric density function, such as normal or beta, this would be overly restrictive as we expect variations in the shape of the PDF as the disease progresses. To accomplish this second aim, we rely on the Prohorov Metric Framework, which provides approximation schemes with asymptotic convergence properties. The adopted approximation scheme represents the PDF of interest using piecewise linear splines. This phase of work provides for a methodology that could potentially translate to a clinical setting. Although in that setting one must substitute a different attenuation model and a different form of attenuation data, the methodology of the inverse problem formulation would be the same and the results would provide quantitative information regarding microstructure. Each of the three phases comprise a chapter of this dissertation, respectively, Chapters 2, 3, and 4.

1.4 Contributions to the Field

The key contributions of this dissertation are as follows:

1. We establish that in cortical bone-like structures, ultrasonic wave attenuation is dependent on microstructure. This provides validation for the novel approach of using ultrasound to quantitatively characterize human cortical bone for the purpose of diagnosing levels of osteoporosis.

2. We establish the use of two physics-based models, the ISA and the WT model, for predicting scattering attenuation in 3D cortical bone mimicking structures. Prior to this, there was not a proposed mathematical model to represent scattering attenuation in human cortical bone. Establishing that these models cannot only accurately predict attenuation, but also allow us to infer microstructural properties of the bone itself provides a crucial step towards developing a quantitative diagnostic tool.

3. We formulated polydisperse models using a probabilistic approach. Although other works, such as [58, 109] had proposed how one may theoretically consider a distributed parameter in a scattering attenuation model, our work explicitly develops three polydisperse models dependent upon the distributed parameter, pore size, and compares these models in the context of solving an inverse problem.

4. We combined the PMF and the concept of variational regularization functions, which penalize various norms of the approximated PDF, in order to stabilize these often ill-posed inverse problems. Doing so provides a nonparametric approach to characterizing the underlying distribution on scatterer size in heterogenous materials.

5. We provide one of the few quantitative approaches to characterizing porosity in cortical bone using ultrasound. This provides broad contributions to the characterization of inclusion size in heterogenous materials in general.

CHAPTER

2

A PHENOMENOLOGICAL MODEL AND SIMULATED DATA

The work in this chapter is based on the published article [119]. The author shares first authorship with O. Yousefian. Specifically, O. Yousefian's contributions include Section 2.2 in addition to the mathematical model formulation given in Section 2.3. The author's contributions include the inverse problem formulation, the sensitivity and standard error analysis (Section 2.4), as well as determining the functional parameter representation (Section 2.6).

2.1 Introduction

Osteoporosis changes the micro-structure of both cortical and trabecular bone [38, 116] which leads to fragility fractures [93, 98], higher morbidity and mortality, and reduction of life expectancy by 1.8 years [29]. Because it constitutes 80 percent of the human skeleton [40], cortical bone supports the main load of the body and largely contributes to the skeletal mechanical competence. The micro-architecture of cortical porosity impacts the macroscopic mechanical properties of cortical bone, and is affected by osteoporosis [68, 92]. It is therefore highly relevant to develop methods for the quantitative assessment of the micro-architecture of cortical porosity, and we hypothesize that tracking the micro-structural changes in cortical bone could benefit the diagnosis of osteoporosis and may enable treatment monitoring [3, 38, 81]. High resolution peripheral quantitative CT (HR-pQCT) and MRI based techniques can be used for the characterization of bone, but MRI lacks resolution for imaging micro-structure of cortical bone ($200~\mu m$ according to [62]), and CT based methods are ionizing [28, 112]. Both methods have limitations associated

with cost and availability of the scanners. Quantitative ultrasonic techniques have the advantage of being relatively low cost and widely available. Additionally, the mechanical nature of ultrasonic waves makes them sensitive to micro- and macro- mechanical changes of cortical bone. The correlation between micro-architectural and ultrasonic parameters could be a key factor for the ultrasonic characterization of the micro-architecture of cortical bone.

A number of studies have been conducted to address the micro-architectural properties of bone using ultrasonic parameters. Most of them have been applied to the assessment of trabecular bone [18, 61, 72, 73, 78, 83, 111].Various techniques have been developed to quantify cortical thickness [49, 76] and speed of sound in cortical bone [26, 65, 89], which is related to the Young's modulus [23]. Mandarano-Fiho et al., [65] carried out an experimental study in vitro to evaluate the influence of cortical bone thickness on ultrasound wave velocity. Sievanen et al., [95] investigated the association between speed of sound and cortical density, cortical wall thickness, and the total cortical area. The interaction between ultrasonic waves and the micro-architecture of cortical bone has not been investigated as thoroughly as it has been for trabecular bone. A recent study has demonstrated a correlation between ultrasound backscatter and cortical porosity [46]. Among all ultrasonic parameters, ultrasonic attenuation, and its frequency dependence have been investigated the least. In a study by Zheng [122], the spectral ratio method was extended to estimate the broadband ultrasound attenuation (BUA) in cortical bone in axial transmission using the primary and multiple reflections between the material interfaces.

To support the aforementioned studies, and to enable a deeper understanding of which parameters of the micro-architecture can be measured when ultrasound propagates in cortical bone, an appropriate model describing the behavior of attenuation in cortical micro-structures remains to be proposed. Ideally, such a model would establish relationships between ultrasonic attenuation and its frequency dependence to micro-architectural parameters of cortical porosity, which include pore diameter and density. This would ultimately enable one to solve inverse problems to infer micro-structural properties of cortical porosity from ultrasound measurements. The study in this chapter focuses on pore diameter and pore density, which are known to be modified by osteoporosis [38, 116] and of which the mechanical competence of cortical bone strongly depends on [81]. However, the individual and independent effect of these two parameters on ultrasonic attenuation is still unclear.

In the present study we use finite differences numerical simulations to measure the attenuation and its frequency dependence in slabs of porous media simulating simplified cortical bone. Pore density and pore diameter are modified independently and ultrasound attenuation is measured in a range of frequencies going from 1 to 8 MHz. A power law model as proposed in [121] is assumed to describe the behavior of the attenuation as a function of frequency. The model parameter estimates are observed to change significantly and monotonically with pore density and pore diameter. The relative sensitivity of all model parameters is studied. This work is the first step towards the development of the solution to an inverse problem that would allow one to retrieve cortical pore density and average pore diameter from ultrasonic measurements in cortical bone.

In Section 2.2 we provide the methodology for the numerical simulations that generate the data. The mathematical and statistical models, which are used to fit this data, are given in Section 2.3. Section 2.4 details the standard error methodology and provides the sensitivity equations for the power law model. The results of this work are given in Section 2.5, and a conclusion follows in Section 2.7.

2.2 Methodology for Data Collection

2.2.1 Simulation Framework

The finite-difference, time domain (FDTD) SimSonic research freeware (www.simsonic.fr) [26] can simulate elastic waves propagating in heterogeneous media with finely controlled mechanical and architectural properties [25, 34, 82]. It is used to simulate wave propagation in porous media resembling cortical bone. The media are comprised of solid slabs containing a distribution of fluid-filled pores. The solid phase is given the material properties of pure bone and the fluid those of water [26]. The independently tunable material properties can be defined at all points in space, which enables a deep understanding of the specific individual effect of the different parameters of the porosity. The pore density (n_s) and diameter (ϕ) ranges are respectively chosen as $n_s \in [3, 16]$ pore/mm^2 and $\phi \in [20, 100]$ μm according to values found in literature [27, 46, 103]. The bone geometry is generated using a Monte Carlo method for a given pore density and pore size. Pores are randomly distributed in the solid bone matrix until the required pore density is reached. Pore volume fraction (ν) is expressed as a function of pore density and diameter:

$$\nu = \text{pore density} \times \text{area of a single pore} = n_s \times \frac{\pi \phi^2}{4} \qquad (2.1)$$

In other words, among the variables in (2.1), pore volume fraction can be derived from the two independent variables, pore diameter and density. Note that (2.1) holds true only if there is no intersection between pores, which was true here since the algorithm used to generate the geometry was not allowing any overlap between pores. Based upon (2.1) and pore density and diameter range, the pore volume fraction of the studied geometries varies between 0.1 to 13.0%.

Spectroscopy is performed in the 1-8 MHz range with 0.5 MHz frequency intervals. A plane wave constituted by a Gaussian ultrasonic pulse with a central frequency within the spectroscopy range and -6dB bandwidth of 20 percent is transmitted through the medium. Figure 2.1 illustrates an example of a medium geometry and the emitted pulse. The slab dimensions are 10mm by 10mm. Table 2.1 summarizes the material properties used in the simulations, where C_{11}, C_{22}, C_{12}, and C_{66} represent the isotropic elastic constants.

(a) Schematic bone geometry

(b) Emitted signal in time and frequency domain
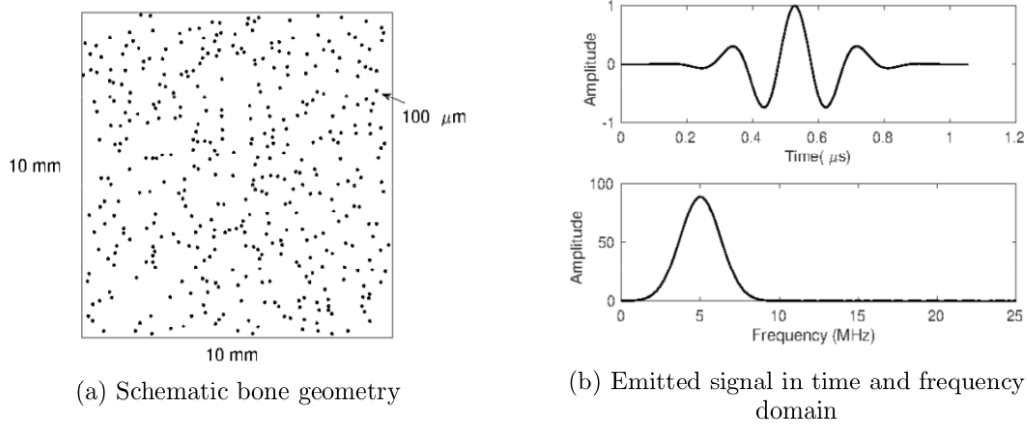
Figure 2.1 Input signal and schematic bone geometry; Pore size: 100 μm; Pore Density: 5 pore/mm^2

Table 2.1 Material properties of the solid and fluid phases [26]

Solid Properties	Value	Fluid Properties	Value
Wave speed C_b ($mm/\mu s$)	4	Wave speed C_b ($mm/\mu s$)	1.54
Density ρ_b (g/ml)	1.85	Density ρ_w (g/ml)	1.00
C_{11} (GPa)	29.60	C_{11} (GPa)	2.37
C_{22} (GPa)	29.60	C_{22} (GPa)	2.37
C_{12} (GPa)	17.60	C_{12} (GPa)	2.37
C_{66} (GPa)	6.00	C_{66} (GPa)	0.00

In all simulations, Perfectly Matched Layer (PML) boundary conditions are applied at both ends of the geometry in the direction of wave propagation with a thickness of 15 times that of the wavelength so that the effect of reflections at the ends of the slab can be ignored. Symmetry boundary conditions are chosen in the direction perpendicular to the direction of wave propagation so that the effect of diffraction can be avoided, and plane wave conditions are assumed. Simulations are run in 2D and the grid spacing is selected as 10 μm in both directions, enabling a spatial sampling of over 50 points per wavelength [76]. This is significantly higher than the minimum proposed value for the spatial-step size, wavelength/20 (i.e. 20 points per wavelength), which also satisfies the stability condition of the numerical scheme applied in elastodynamics by [105, 106].

2.2.2 Attenuation Measurement: Time-Distance Matrix Approach (TDMA)

SimSonic is used to transmit plane waves through the porous-liked media described above. The propagated signals are recorded at 30 consecutive longitudinal positions along the sample in the direction of wave propagation. The transducers used in the simulation are large and cover the whole geometry (the transducer length is the same as slab height). As a result, the signals measured on these transducers correspond to signals averaged over the whole height of each slab. Since the pores are uniformly distributed, averaging over multiple slabs is equivalent to averaging over large slabs using large transducers.

The time-domain recorded signals are stored in a time-distance matrix, $s(\tilde{t}, x)$. The matrix can be converted into the frequency domain, $S(\omega, x)$ through Fast Fourier Transform (FFT). Hence, each element in the frequency-distance matrix, $S(\omega, x)$ represents the spectrum at a given longitudinal position. To satisfy the Courant–Friedrichs–Lewy (CFL) stability condition for the SimSonic numerical scheme [105, 106] the sampling time step Δt was chosen as:

$$\Delta t = 0.99 \frac{1}{\sqrt{d}} \frac{\Delta x}{c_{max}} \tag{2.2}$$

where c_{max} is the greatest speed of sound in the simulation medium and d is the dimension of space ($d = 2$ for 2D simulation) [26]. A Gaussian window (window length = 200) is used over the signals in frequency domain $S(\omega, x)$.

By assuming an exponential decay for the propagated signal [73], the amplitude of the signals contained in the frequency-distance matrix can be approximated as:

$$|S(\omega, x)| = e^{-\alpha(\omega)x}. \tag{2.3}$$

Hence, for each frequency, if $\ln |S(\omega, x)|$ versus x_i is plotted, the absolute value for the slope of the linear fit to the data represents the attenuation coefficient, $\alpha(\omega)$. As an example, Figure 2.2 depicts the attenuation spectroscopy in 1-8 MHz frequency range for pore diameter: 100 μm and pore density: 5 pore/mm^2. For each plot of the attenuation versus frequency, the Root Mean Square Error (RMSE) values was calculated to estimate the goodness of the power law fit. For all fits, the RMSE values were in a range of 0.007 (Pore Density: 3 pore/mm^2 - Pore Diameter: 20 μm) to 3.013 (Pore Density: 16 pore/mm^2 - Pore Diameter: 120 μm).
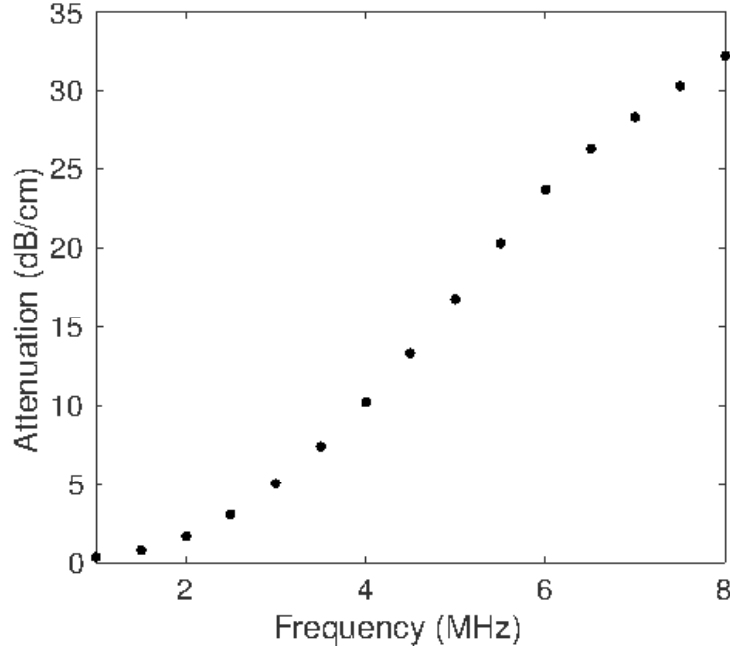
Figure 2.2 Attenuation spectroscopy; Pore size: 100 μm, Pore density: 5 pore/mm^2 RMSE value for power law fit: 1.441

2.3 Mathematical and Statistical Models

2.3.1 Effect of absorption on attenuation

Both scattering and absorption contribute to the total amount of attenuation. To study their effects independently, two different sets of simulations are run on 2D geometries with different pore diameters and pore densities: 1) Simulations that do not account for absorption and exclusively address the effect of scattering. 2) Simulations that take both absorption and scattering into account. To run the second group of simulations, the value for the absorption coefficient needs to be included in the material properties. To obtain this value a simple procedure is implemented. The total attenuation coefficient is the sum of absorption coefficient and scattering coefficient. By isolating the effect of scattering through running absorption-less simulations, the scattering coefficient is obtained. The experimentally measured value for the attenuation coefficient is reported in the literature to be 50 dB/cm [90] at 5 MHz. This value accounts for both scattering and absorption. The average attenuation coefficient from group 1 simulations for geometries with pore diameter of 60 μm and pore densities ranging from [5 25] pore/mm^2 is 11.9 dB/cm at 5 MHz. By subtracting this value, which is purely due to scattering (scattering attenuation coefficient), from the total value of 50 dB/cm, an absorption coefficient of 38.1 dB/cm is obtained at 5 MHz and used as an input parameter for simulations that take absorption into account. A linear dependence of absorption with respect to frequency is assumed. By employing the same approach, the absorption coefficient of 29 dB/cm is used for geometries with a constant pore

density of 10 pore/mm^2 and pore diameters ranging from [40 120] μm. The difference between absorption coefficients in groups 1 and 2 is due to the fact that the average scattering coefficient is different for the two groups. It was also assumed that the bone matrix is a homogeneous medium and the viscoelasticity of the matrix or the absorption coefficient is the same for both compressional and shear waves. The attenuation coefficient is plotted versus pore diameter and pore concentration for absorbing and non-absorbing simulations (Figure 2.3). An offset is observed in the plots where absorption is taken into account. The difference between the two cases is depicted in Figure 2.3 and suggests that although absorption significantly increases the overall value of attenuation, the offset is constant with respect to pore diameter and pore density.
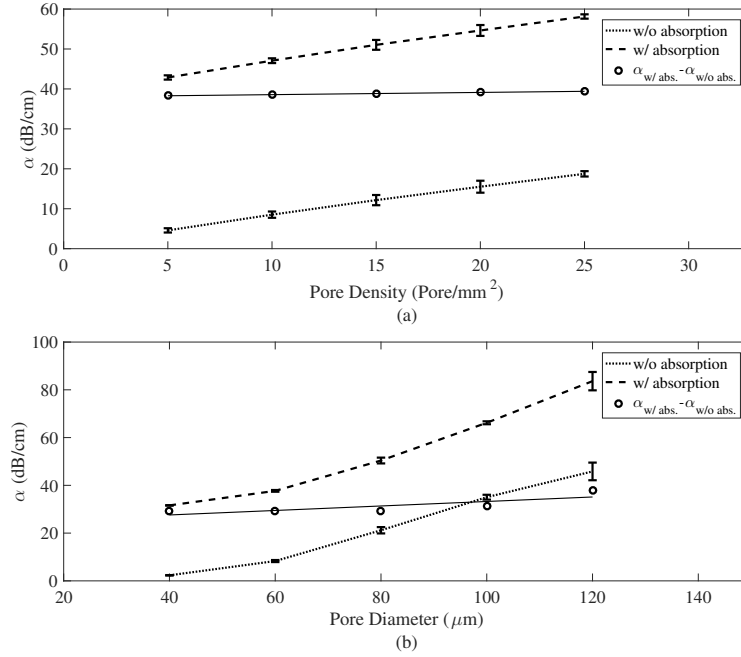
Figure 2.3 Attenuation coefficient versus (a) pore density and (b) pore diameter

The dotted line in Figure 2.3 shows the shift in attenuation due to absorption. It can be observed that the difference, $\alpha_{w/abs} - \alpha_{w/oabs}$, is approximately constant with respect to changing pore diameter or density. Based on the results shown in Figure 2.3, it can be concluded that the dependence of attenuation upon pore density and pore diameter is not affected by the inclusion of absorption. Therefore, the simulations presented in the rest of this article do not account for absorption.

2.3.2 Scattering Regime and choice of pore diameter and pore density as microstructural parameters of interest

Based on the values for pore size and the frequency range, the scattering regime is low to intermediate (wavelength > scatterer size). In this regime, some of the energy is lost during propagation can be attributed due to scattering. The elastic mean free path is the characteristic length describing the exponential decay of the wave, averaged over many realizations of scatterers distributions (coherent wave). Because the simulated transducers are so large and the pores uniformly distributed, it can be assumed that a sufficient number of realizations of scatterer distribution is taken into account in the average. The Coherent Potential Approximation [94] states the elastic mean free path is inversely proportional to the scatterer density and to the scattering cross section $l_s = (n_s\sigma)^{-1}$, with n_s the pore density and σ the scattering cross section [104]. The scattering cross section is a function of the pore diameter. Because pore density and pore diameter contribute to bone mechanical competence, and influence the elastic mean free path and therefore the scattering attenuation, they were chosen as parameters of interest for this study. The attenuation of elastic waves in porous media and its dependence on pore volume fraction parameters have been studied in seismology [30, 44, 108], civil-structure engineering [86] as well as biomedical ultrasound [48, 99, 101, 110]. These studies reveal that changes in porosity in media such as dry porous rock, porous sandstone containing gas and water, cement paste with entrained air voids and trabecular bone affect the scattering and attenuation of the propagated wave which can be used to characterize the porous medium.

2.3.3 Mathematical model for attenuation due to scattering

Mathematical models are used to represent physical and biological systems to investigate hypotheses regarding the underlying physical process. A *mechanistic model* hypothesizes the relationships between physically interpretable parameters and variables, while a *phenomenological model* captures the qualitative trends of the desired dynamics. Here, the physical process of interest is wave propagation in bone. We begin by developing a phenomenological model that describes the trends seen in numerical simulation for the attenuation in bone-mimicking porous media as a function of ultrasonic wave frequency. This mathematical model is given by

$$\alpha(\omega) = a\omega^b + c,$$

where α represents the attenuation coefficient, which is dependent on frequency, ω. The model parameters are given by $\boldsymbol{\theta} = [a \quad b \quad c]$.

To make meaningful inferences regarding parameter estimates, one must also take into account error incurred in the data collection process. One does so by specifying a statistical model, which represents the observation process regarding data collection. to account for the uncertainty we

would expect in observational data, we consider the following statistical error model

$$Y(\omega) = \alpha(\omega, \boldsymbol{\theta}_0) + \mathcal{E}(\omega), \tag{2.4}$$

where $Y(\omega)$ is a random variable, $\boldsymbol{\theta}_0$ is the nominal parameter vector, and the $\mathcal{E}$ are assumed to be independent and identically distributed with mean 0 and variance σ_0^2. A realization of this statistical error model is given by

$$y(\omega) = \alpha(\omega, \boldsymbol{\theta}_0) + \epsilon(\omega), \quad \omega \in [\omega_0, \omega_F], \tag{2.5}$$

where ϵ is a specific realization of the random variable $\mathcal{E}$. This is a reasonable specification of the statistical error model since the numerical simulation that generates the data likely allots the same error to each data point. It is important to note that both the mathematical and statistical model need to be correctly specified to make meaningful inferences regarding parameter estimates.

2.4 Sensitivity and Standard Error Methodology

Since we assume an absolute error statistical model, given in (3.21), we estimate the model parameters by solving an inverse problem with an ordinary least squares (OLS) formulation, following [12, 15]. Solving this inverse problem corresponds to minimizing the sum of squared errors between the data and the model output when we treat all observations as equally important.

The OLS estimator is given by

$$\boldsymbol{\Theta}_{OLS} = \boldsymbol{\Theta}_{OLS}^N = \operatorname{argmin}_{\boldsymbol{\theta}} \sum_{j=1}^{N} [Y_j - \alpha(\omega_j, \boldsymbol{\theta})]^2,$$

where Y_j is a random variable corresponding to the observation process and N represents the number of frequency points. A realization of the random variable, $\boldsymbol{\Theta}_{OLS}$, is given by

$$\hat{\boldsymbol{\theta}}_{OLS} = \hat{\boldsymbol{\theta}}_{OLS}^N = \operatorname{argmin}_{\boldsymbol{\theta}} \sum_{j=1}^{N} [y_j - \alpha(\omega_j, \boldsymbol{\theta})]^2,$$

where y_j is realization of Y_j. With the parameter estimate, $\hat{\boldsymbol{\theta}}$ (where we now suppress the dependence of the estimate on the OLS formulation), we can compute the sensitivity matrix as

$$\chi_{j,k} = \frac{\partial \alpha(\omega_j, \hat{\boldsymbol{\theta}})}{\partial \hat{\theta}_k}, \quad j = 1, \ldots, N, \quad k = 1, \ldots, p,$$

where $p = 3$ represents the number of model parameters. Specifically, since the model given in

(2.4) can be explicitly differentiated with respect to the parameters, we have that

$$\frac{\partial \alpha(\omega_j, \hat{\boldsymbol{\theta}})}{\partial a} = \omega_j^b, \tag{2.6}$$

$$\frac{\partial \alpha(\omega_j, \hat{\boldsymbol{\theta}})}{\partial b} = a \log(\omega_j) \omega_j^b, \tag{2.7}$$

$$\frac{\partial \alpha(\omega_j, \hat{\boldsymbol{\theta}})}{\partial c} = 1, \quad j = 1, \ldots, N. \tag{2.8}$$

Notice that $\chi = \chi^N \in \mathbb{R}^{N \times p}$ is dependent on the number of frequency points as well as the parameter estimate, $\hat{\boldsymbol{\theta}} = [\hat{a} \ \ \hat{b} \ \ \hat{c}]$. The true, constant variance is a random variable given by

$$\sigma_0^2 = \frac{1}{N} E \left[\sum_{j=1}^{N} [Y_j - \alpha(\omega_j, \boldsymbol{\theta}_0)]^2 \right],$$

where $E[\cdot]$ refers to the expected value. Then, we estimate this variance, adjusting for the bias, by

$$\hat{\sigma}^2 = \frac{1}{N - p} \left[\sum_{j=1}^{N} [y_j - \alpha(\omega_j, \hat{\boldsymbol{\theta}})]^2 \right].$$

We can then estimate the covariance matrix as

$$\hat{\Sigma}^N = \hat{\sigma}^2 \left[\chi(\hat{\boldsymbol{\theta}})^T \chi(\hat{\boldsymbol{\theta}}) \right]^{-1}.$$

Then, the asymptotic standard errors are given as

$$SE_k(\boldsymbol{\theta}_0) = \sqrt{(\Sigma_0^N)_{kk}}, \quad k = 1, \ldots, p,$$

which are estimated by

$$SE_k(\hat{\boldsymbol{\theta}}) = \sqrt{(\hat{\Sigma}^N(\hat{\boldsymbol{\theta}}))_{kk}}, \quad k = 1, \ldots, p.$$

The confidence interval for parameter estimate $\hat{\theta}_k$ with a confidence level of $100(1 - \alpha)\%$, is given by

$$[\hat{\theta}_k - t_{1-\alpha/2} SE_k(\hat{\boldsymbol{\theta}}), \hat{\theta}_k + t_{1-\alpha/2} SE_k(\hat{\boldsymbol{\theta}})],$$

where $\alpha \in [0, 1]$ and $t_{1-\alpha/2}$ is computed from the Student's t distribution with $N - p$ degrees of freedom [15].

2.5   Results and Discussion

The model parameter estimates ($\hat{\theta} = [\hat{a} \ \ \hat{b} \ \ \hat{c}]$) versus pore diameter ($\phi$) and pore density ($n_s$) are given in Figure 2.4. From these figures we see that there is a consistent trend relating the parameter estimates to pore diameter and density. For instance, Figure 2.4 shows that for all

densities and diameters $\leq 60\mu m$ the estimates for a and c are constant. Then, as diameter increases, the estimates for a increase while the estimates for c decrease. Similarly, in Figure 2.4 we see a somewhat linear relationship between the estimates for b and the pore diameter, where the estimates increase as diameter decreases. From this we gather how it may be possible to infer pore diameter and density from the estimates of the model parameters.
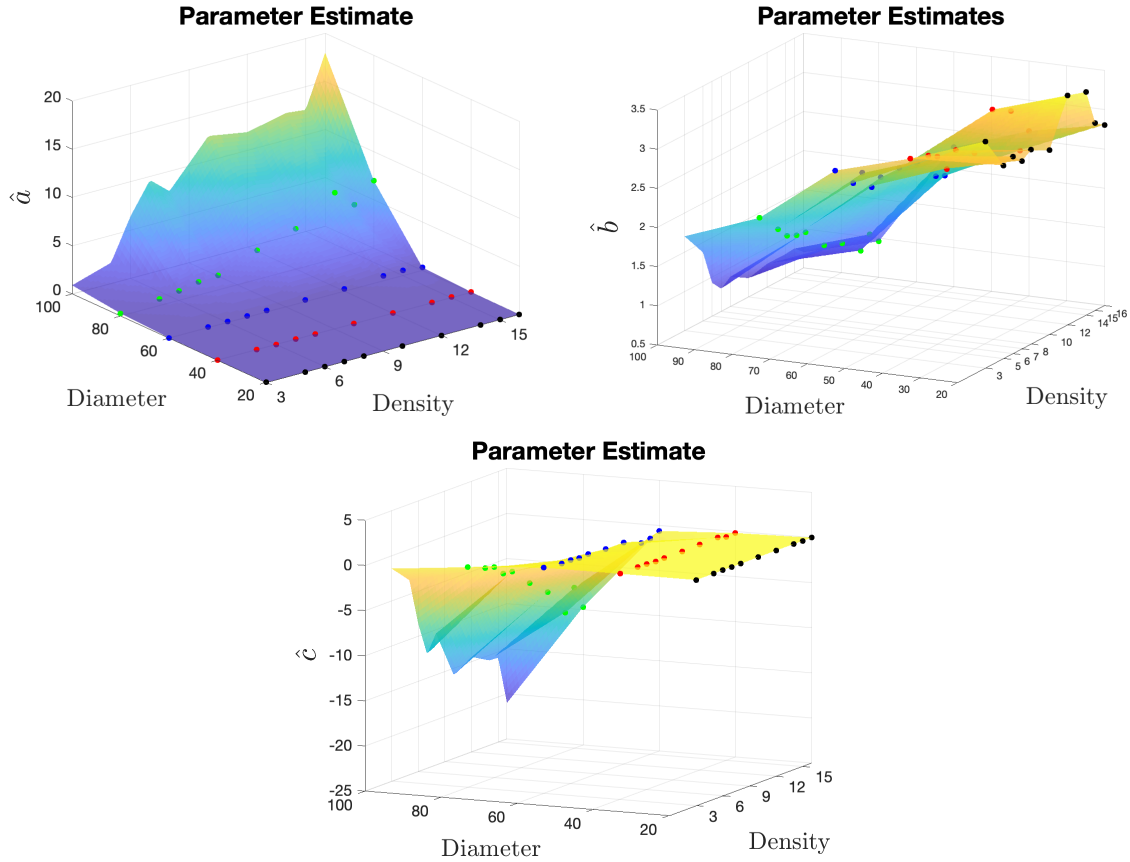
Figure 2.4 Parameter estimates versus pore diameter ([20 40 60 80 100] μm) and pore density ([3 5 6 7 8 10 12 14 15 16] pore/mm^2)

Since our goal is to infer micro-architectural information from these parameter estimates, we wish to determine which parameters have the most significant influence on the model solution. To do so, we use local sensitivity analysis to examine how the model output changes with respect to perturbations in the nominal parameter estimates for a given data set. That is, we use the methodology laid out in Section 2.4 to estimate model parameters for data sets corresponding to pore diameters [20 40 60 80 100] μm, and pore densities [3 5 6 7 8 10 12 14 15 16] pore/mm^2. We then calculate the sensitivity of the model with respect to these estimates using (2.6)-(2.8). These sensitivities are plotted versus frequency (MHz) for pore diameter 60 μm and given in Figure 2.5. The sensitivity plots for the other pore diameters considered follow a similar trend

20

and can be found in [120]. Note that the parameter estimates themselves are given in the legend. For a more convenient comparison, the sensitivities of the estimates for a and b have been plotted versus all densities and frequencies in Figure 2.6.

The parameter estimates and corresponding 95% confidence intervals are given in Figure 2.7. For comparison, 80% confidence intervals are given for pore diameter $60\mu m$ in Figure 2.8. To see confidence intervals for the other pore diameters considered see [120].

2.5.0.1 Pore Diameter $60\mu m$

Figure 2.5 Local model sensitivity to parameter estimates for pore diameter 60 μm, densities of [3 5 6 7 8 10 12 14 15 16] pore/mm^2, and frequency 1-8 MHz

Sensitivity
Density: 3 (pore/$(mm)^2$) Diameter: 60 (μm)

a = 0.0289	
b = 2.7806	
c = 0.014	

Sensitivity
Density: 5 (pore/$(mm)^2$) Diameter: 60 (μm)

a = 0.0833	
b = 2.4956	
c = -0.2738	

Sensitivity
Density: 6 (pore/$(mm)^2$) Diameter: 60 (μm)

a = 0.0873	
b = 2.5687	
c = -0.206	

Sensitivity
Density: 7 (pore/$(mm)^2$) Diameter: 60 (μm)

a = 0.1526	
b = 2.3264	
c = -0.3757	

Sensitivity
Density: 8 (pore/$(mm)^2$) Diameter: 60 (μm)

a = 0.1588	
b = 2.3889	
c = -0.3044	

Sensitivity
Density: 10 (pore/$(mm)^2$) Diameter: 60 (μm)

a = 0.1983	
b = 2.3832	
c = -0.4352	
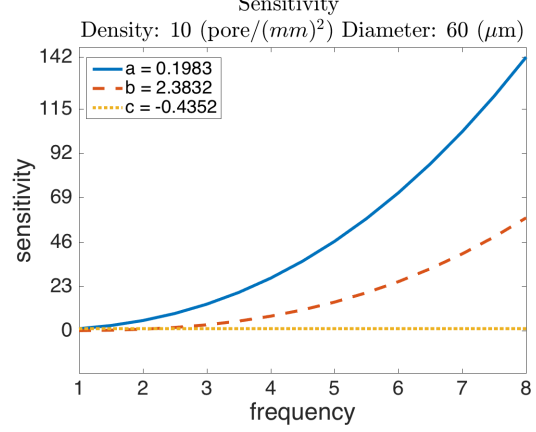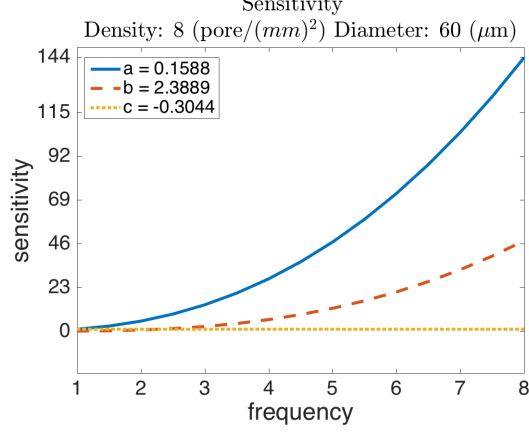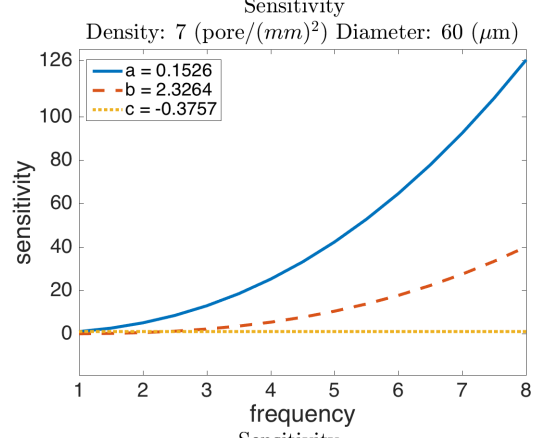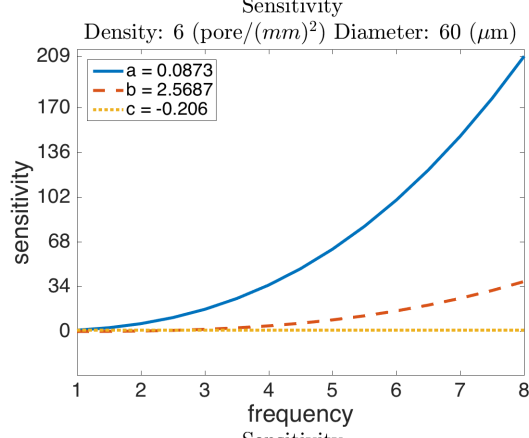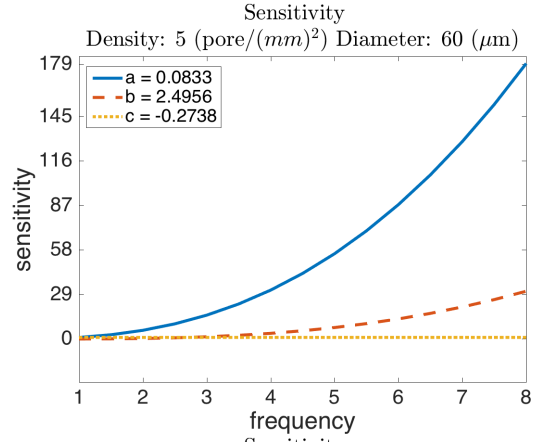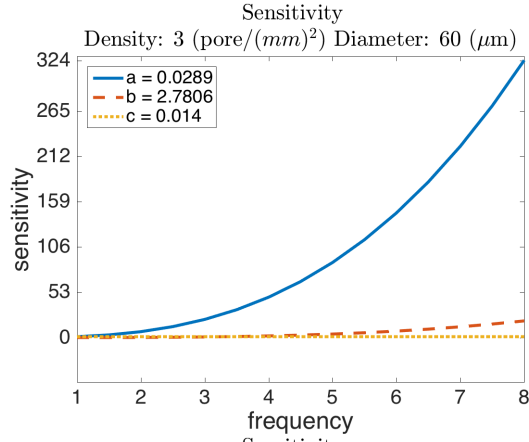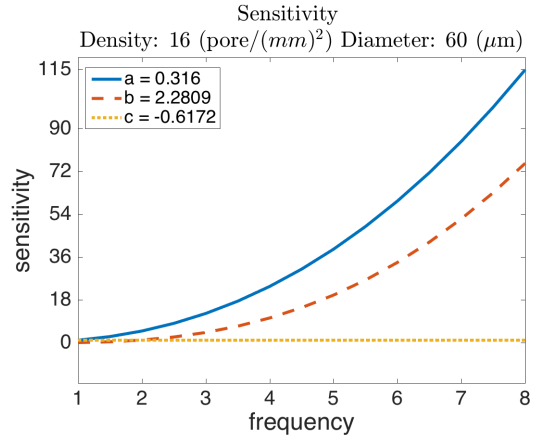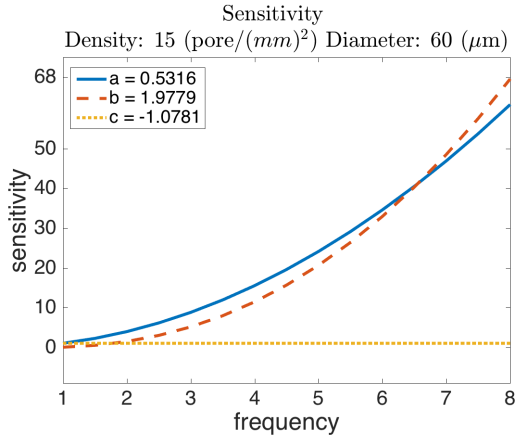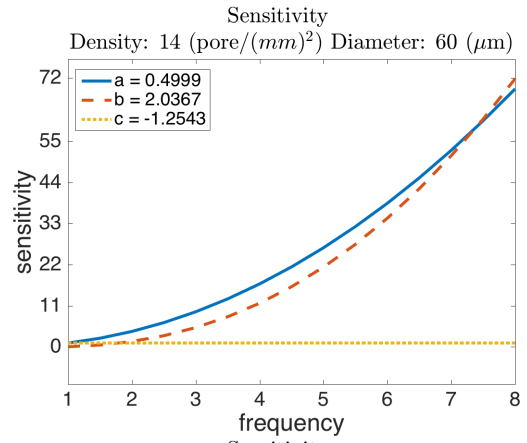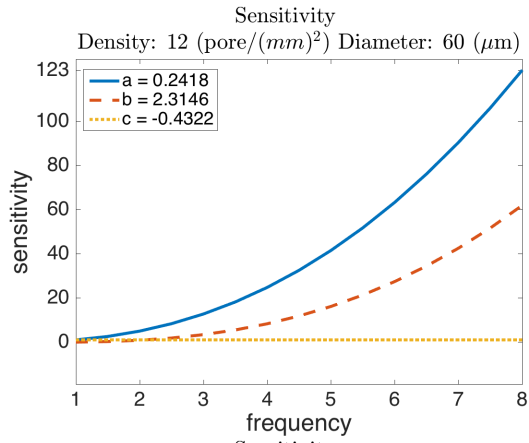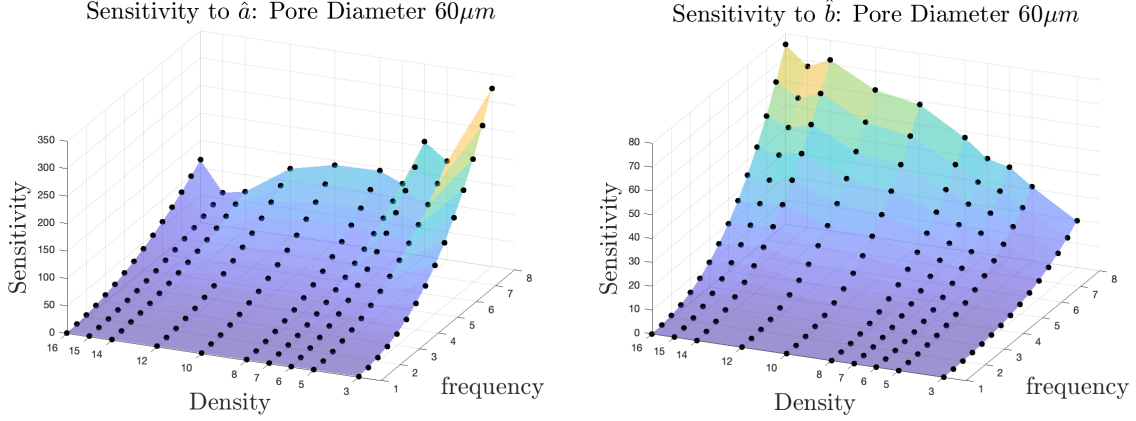
Figure 2.6 Local sensitivity to $\hat{a}$ and $\hat{b}$ for pore diameter 60 μm, densities of [3 5 6 7 8 10 12 14 15 16] pore/mm^2, and frequency 1-8 MHz

Notice that the sensitivity of the model with respect to estimates of c (denoted $\hat{c}$) will be constant and equal to 1 from (2.8). Furthermore, we see from the sensitivity figures that as frequency increases, so does the sensitivity of the model with respect to the estimates of a and b (denoted $\hat{a}$ and $\hat{b}$ respectively). This is intuitive looking at (2.6) and (2.7) as both are increasing functions of frequency. g We then observe that model sensitivity to $\hat{a}$ and $\hat{b}$ depends heavily on pore diameter. There is a general trend that for smaller diameters ($\phi = 20$ μm and $\phi = 40$ μm), the model is sensitive only to $\hat{a}$. Similarly, we see that the model is sensitive only to $\hat{b}$ for larger diameters ($\phi = 100$ μm) (see [120]). For intermediate pore diameters ($\phi = 60$ μm and $\phi = 80$ μm), model sensitivity to $\hat{a}$ and $\hat{b}$ depends on pore density. For instance, from Figure 2.5 we see that for $\phi = 60$ μm at low densities (3 and 5 pore/mm^2) the model is sensitive to $\hat{a}$. However, as density increases, model sensitivity to $\hat{b}$ increases while sensitivity to $\hat{a}$ decreases. For higher densities (≥ 14 pore/mm^2), model sensitivity to $\hat{a}$ and $\hat{b}$ are roughly the same. A similar trend is seen for $\phi = 80$ μm, except here the model is only slightly more sensitive to $\hat{a}$ as $\hat{b}$ for density 3 pore/mm^2. As density increases, sensitivity to $\hat{a}$ decreases while sensitivity to $\hat{b}$ increases. For high densities (≥ 14 pore/mm^2) the model is only sensitive to $\hat{b}$. For pore diameter $\phi = 100$ μm, the model is only sensitive to $\hat{b}$ (see [120]).

Next, we address the confidence interval figures. In general, the size of the confidence intervals depends on the level of confidence desired, the parameter estimates themselves, and the relative sensitivity of the model to these estimates. Notice that relative to parameter estimate size, the confidence intervals for $\hat{c}$ are significantly larger than for $\hat{a}$ and $\hat{b}$ for all diameters and densities. This is due to the fact that the model is not sensitive to $\hat{c}$, which makes difficult estimating this parameter with high confidence. Furthermore, we found there is not a strictly monotone trend in confidence interval width with respect to increasing density and diameter. This is due to the standard errors and resulting confidence interval widths' (see Section 2.4) dependence on multiple factors. We do, however, note that it is common for the confidence intervals for all
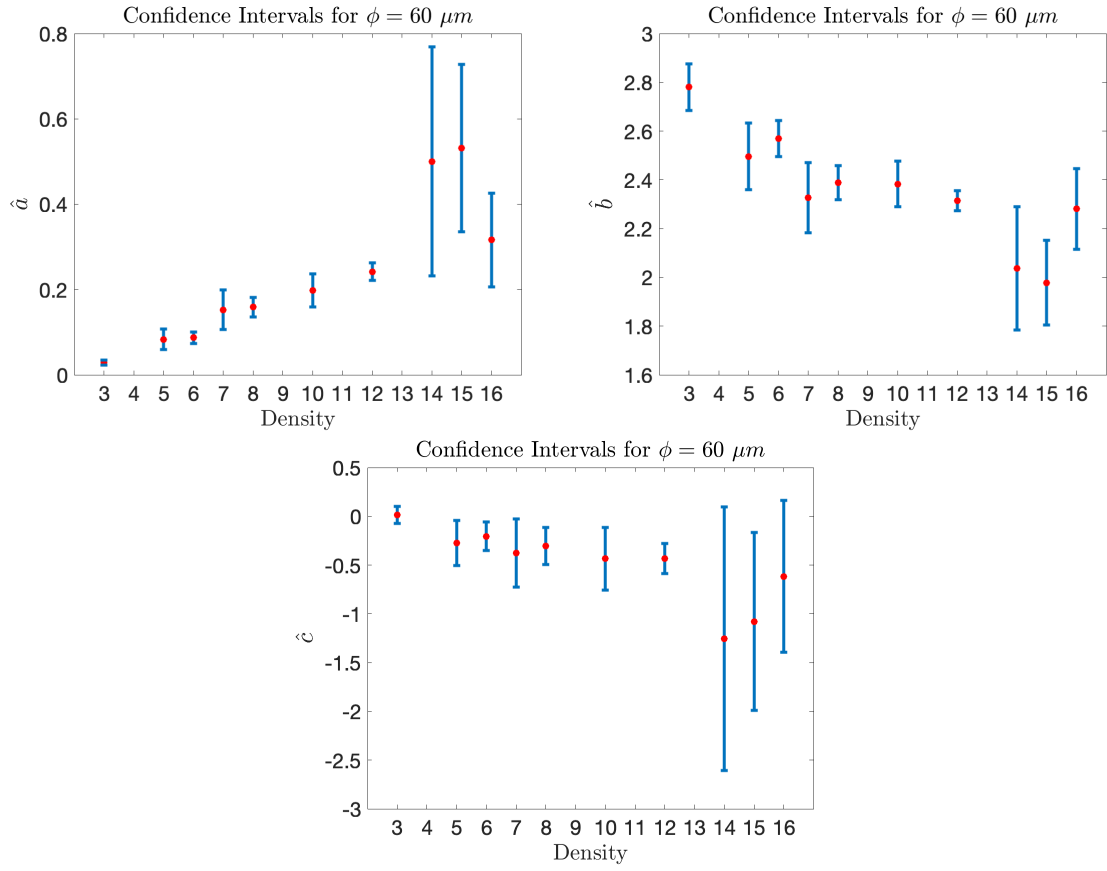
Figure 2.7 Parameter estimates and corresponding 95% confidence intervals for $\hat{a}$, $\hat{b}$, and $\hat{c}$ for pore diameter 60 μm and densities of [3 5 6 7 8 10 12 14 15 16] pore/mm^2
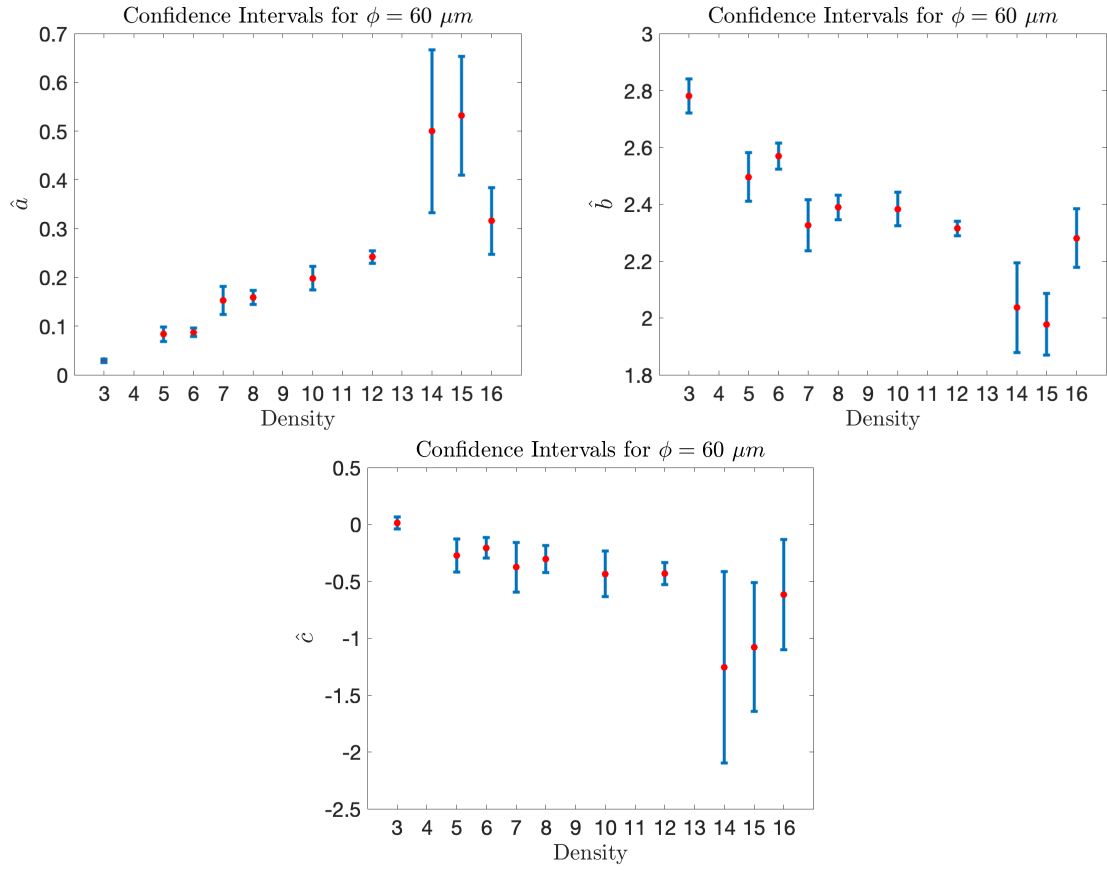
Figure 2.8 Parameter estimates and corresponding 80% confidence intervals for $\hat{a}$, $\hat{b}$, and $\hat{c}$ for pore diameter 60 μm and densities of [3 5 6 7 8 10 12 14 15 16] pore/mm^2

estimates to widen as density increases (e.g., see Figure 2.7). This could be an artifact of the numerical simulation that results in the data from which the parameter estimates are derived. Furthermore, as pore density increases the scattering regime changes. This affects the parameters estimated when fitting the power law model to data for these higher densities.

Since 95% confidence in parameter estimates may be higher than the acceptable level of confidence, 80% confidence intervals have been given for pore diameter 60 μm (see Figure 2.7 and Figure 2.8). As expected, the intervals are significantly wider when 95% confidence is desired. Furthermore, we still see the trend of wider intervals at higher densities in these figures.

2.6 Functional Parameters

Establishing that we can accurately and confidently estimate the parameters for the power law model allows us to address the next goal of relating the model parameters to the micro-architectural ones. In Figure 2.4 we see that there is a clear dependence of parameter estimates on diameter and density. Furthermore, we have established that there exist density and diameter ranges for which our model is more or less sensitive to certain parameters. With this in mind, we propose the following model

$$\alpha(\omega) = a(\phi, n_s)\omega^{b(\phi, n_s)} + c,$$

where the sensitive model parameters (a and b) are themselves a function of the micro-architectural ones. With a model of this form, we can infer pore diameter (ϕ) and density (n_s) from the estimates of a and b. We begin by noting the pattern between the estimates $\hat{b}$ and pore size (ϕ) and density (n_s) from Figure 2.4. We see a somewhat linear trend between the estimates $\hat{b}$ and pore diameter. However, from Figure 2.9, we note that this relationship is not bijective.
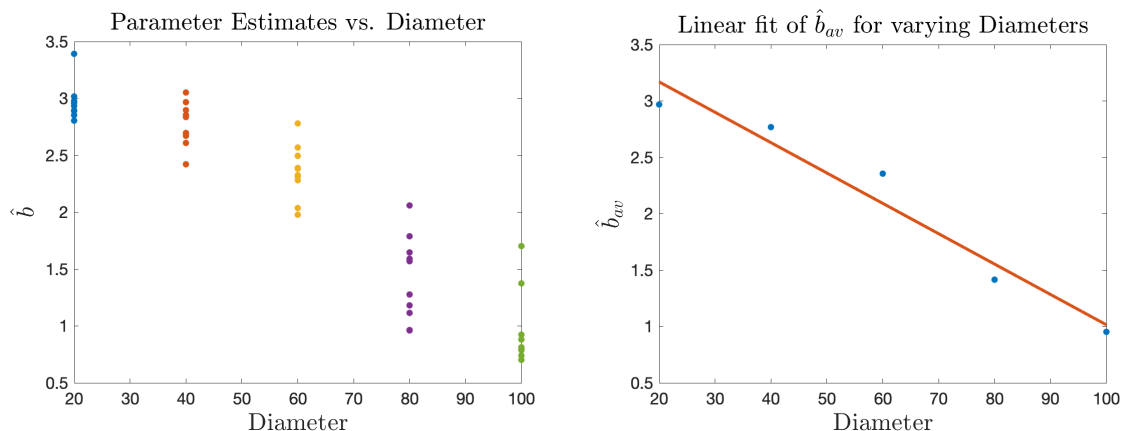
Figure 2.9 Left: Estimates $\hat{b}$ versus pore diameter for all densities considered. Right: Linear fit of $\hat{b}_{av}$ versus pore diameter

$$\hat{b}_{av} = -0.0269\phi + 3.7078 \tag{2.9}$$

Table 2.2 Nominal pore diameter versus estimated range based on the linear relationship (2.9)

ϕ_0	$\hat{\phi}$
20	11 - 33
40	24 - 47
60	34 - 64
80	61 - 102
100	74 - 111
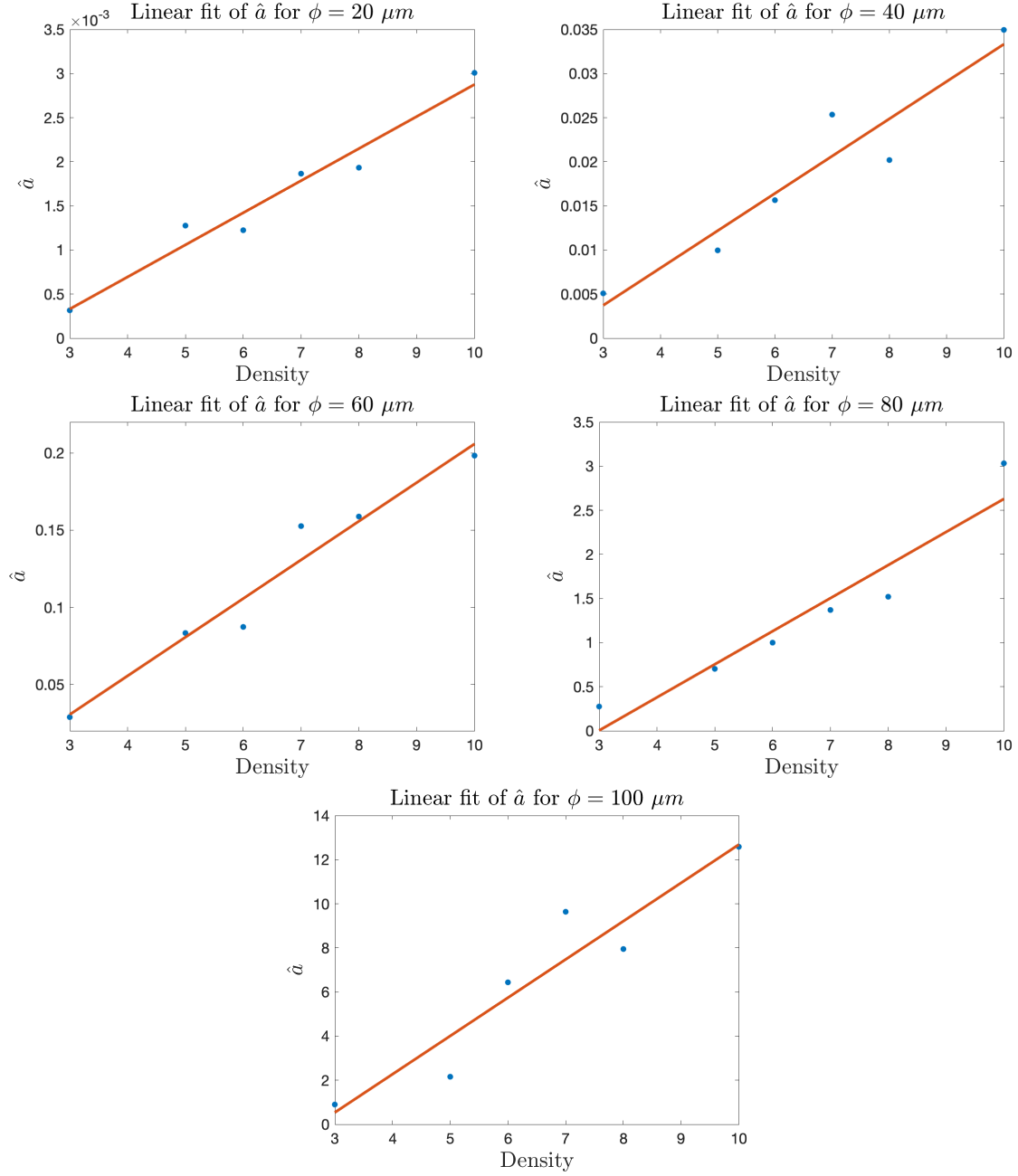
Figure 2.10 Linear fit of estimates $\hat{a}$ versus pore density for $\phi = [20 \ \ 40 \ \ 60 \ \ 80 \ \ 100] \ \mu m$

2.7 Conclusions

The overall goal of the research in this chapter was to investigate a phenomenological relationship between parameters of the porosity (pore density and diameter) and frequency dependent attenuation. To do this, we developed a phenomenological model that describes the attenuation of ultrasonic waves in a random, non-absorbing porous medium with controlled pore size and

pore density mimicking the simplified structure of cortical bone. Absorbing media were also considered, but it was shown that, although it did offset the overall values for attenuation, the attenuation due to absorption was not a function of pore density and pore diameter. We numerically generated data using a 2D finite-difference time domain SimSonic research freeware, which simulates elastic waves propagating in heterogeneous media. 2D simulations were chosen because of the high computational cost of 3D simulations. However to assess how the attenuation results might be different with more realistic pore shapes as well as due to out of plane diffraction, 3D simulations were also performed on a few cases. Spherical non overlapping pores, randomly distributed in a bone matrix, were chosen as a geometry map mimicking a simplified geometry of 3D cortical bone slabs. The location of emitter/receivers were chosen as in 2D simulations: a plane wave was transmitted through the porous medium and the propagated signals were recorded at 30 consecutive longitudinal positions along the sample in the direction of wave propagation. The transducers used in the simulation had the same height and depth as the slabs'. As a result, the signals measured on these transducers corresponded to signals averaged over the whole height and depth of each slab. Since the pores were uniformly distributed, averaging over multiple slabs is equivalent to averaging over large slabs using large transducers. The same boundary conditions and emitting signal as 2D simulations were chosen. The results revealed that the difference in attenuation between 2D and 3D models for a given structure was around 10 - 15 %. We then fit this model to the simulated data using an ordinary least squares framework for the inverse problem. With the resulting estimates, we performed local sensitivity analysis and calculated confidence intervals for the parameters estimated.

We determined that model sensitivity to parameter estimates depends on pore diameter and density. Namely, we determined via the analytical partial derivatives that the model is not sensitive to c. Furthermore, for small diameters ($\phi = 20 \ \mu m$ and $\phi = 40 \ \mu m$) the model is sensitive mainly to estimates of a; whereas for large diameters, ($\phi = 100 \ \mu m$) the model is sensitive mainly to estimates of b. For intermediate diameters ($\phi = 60 \ \mu m$ and $\phi = 80 \ \mu m$) sensitivity depends on pore density, where the model is more sensitive to $\hat{a}$ at low densities and more sensitive to $\hat{b}$ at high densities. We also calculated asymptotic standard errors and confidence intervals for the parameter estimates to determine for what diameters and densities we can accurately estimate the model parameters. We found that for parameter estimates the model was sensitive to (a and b) we could estimate parameters with a high level of confidence. In general, the 95% confidence intervals for these estimates were wider at high densities (≥ 14 pore/mm^2).

The model developed and analyzed in this study was based on 2D numerical simulations mimicking the wave propagation within the simplified models of cortical bone. Unlike an experimental study, the simulation tool enabled the independent control over the micro-structural parameters such as pore diameter and pore density, which was needed to establish the parametric model. This justifies the choice of simplified microstructures over real cortical microstructures. In subsequent chapters of this dissertation, efforts will be directed towards the development of an

inverse problem, which should enable to infer pore density and pore diameter from attenuation measurements. Possible dependence of the attenuation on porosity itself, rather than porosity parameters (pore density and diameter) will be studied in the future to determine the sensitivity of attenuation to pore volume fraction. In Chapter 4 we will study polydisperse pore distributions instead of the monodisperse case studied here, to describe more realistic cortical porosities.

Acknowledgments

CHAPTER

3

A 3D PHYSICS-BASED MODEL FOR MONODISPERSE SAMPLES AND SIMULATED DATA

This chapter is based on the work in [114]. The author was lead author on this article. Her contributions to this research include investigating the attenuation models, formulating the inverse problem (Section 3.4), solving the optimization problems (Section 3.5), and performing all numerical experiments.

3.1 Introduction

The work in this chapter aims to characterize the microstructure of complex heterogeneous media mimicking cortical bone using ultrasonic interrogation. This work is an improvement on the work in Chapter 2, which established that attenuation is affected by microstructure, as here we aim to mathematically model attenuation as explicitly dependent upon pore size and density. This allows us to infer directly the microstructural parameters by formulating and solving inverse problems. This provides a higher resolution technique for quantifying levels of osteoporosis present in cortical bone. As previously mentioned, Osteoporosis is one of the most common bone diseases and leads to the degradation of both trabecular and cortical bone, resulting in an on average increase in both pore size (radius) and the number of pores present (density) [38, 116], although for later stages, merging of very large pores can lead to a decrease in pore density [57].

This degradation results from aging, menopause, as well as certain medications and leads to an increase in susceptibility to fracture [38, 56]. On average, 20% of men and 33% of women over age 50 will experience osteoporotic fractures [69, 70], with more than 8.9 million fractures worldwide annually [60]. Furthermore, studies show that in women, 80% of appendicular bone loss during menopause is attributed to cortical bone degradation [21]. Early diagnosis and treatment can reduce the risk of osteoporosis related injuries [41].

The classical approach to quantifying markers of osteoporosis, such as Bone Mineral Density (BMD) evaluation has been shown to be inadequate in predicting fractures due to a significant BMD overlap between subjects who experienced a fracture and subjects who didn't [66]. Furthermore, magnetic resonance (MR) imaging can be used to characterize cortical bone porosity [88], but it is costly, has a poor resolution, and is infeasible in practice at large scales for screening purposes. Thus, a non-invasive, non-ionizing method for quantifying osteoporosis is needed. Quantitative ultrasound (QUS) can potentially provide just that. Furthermore, it has been shown in [36, 43] that ultrasound parameters such as speed of sound and backscattering coefficient relate to the microstructural parameters of bone including trabecular thickness and pore volume fraction albeit for trabecular bone [25, 79, 110]. Among all the QUS parameters, it has been shown that changes in pore size and density in cortical bone have a significant impact on attenuation as it affects the scattering of waves. This was done using phenomenological modeling of ultrasonic attenuation and provides information regarding porosity at the resolution of low, medium, or high porosity, but was unable to capture more detailed microstructural properties [119]. In comparison, physics-based models, such as the Independent Scattering Approximation (ISA) have been shown to predict attenuation in trabecular bone samples [74] as well as in simulated 2D cortical bone samples [118]. A higher order model used to calculate wave attenuation, the Waterman Truell (WT) model, has been used for heterogeneous structures such as 3D acoustic metamaterials [31]. Furthermore, quantifying the size and density of air voids entrapped in cement using ultrasonic attenuation has been researched. Specifically, simplex methods were used to calibrate the ISA to the experimental data and produce microstructural parameter estimates [85].

In this work we aim to quantify pore size and density for structures mimicking cortical bone using ultrasonic attenuation. To do so, we generate frequency dependent attenuation data using the *SimSonic* FDTD Matlab package [24] to simulate wave propagation in monodisperse structures with pores randomly distributed. We consider pore radii ranging from 50 to $100 \mu m$ and densities ranging from 20 to 50 pores/mm^3. These values correspond to porosity values reported in the literature for cortical bone [47, 103]. To retrieve the micro-architectural properties of porosity from attenuation data, we then formulate and solve an inverse problem, fitting the WT and ISA models to the simulated data sets. This produces estimates for pore radius and density, which are compared to the nominal values used to generate the data. Estimates closely matching the nominal values, indicate both models are capable of inferring the microstructural parameters associated with random heterogeneous media similar to that of cortical bone.

The ultimate goal is to infer the microstructure of cortical bones in humans *in vivo*. This

present work provides a crucial step towards being able to do so. We validate the use of the ISA along with the higher order WT model to estimate the microstructural parameters, pore radius and pore density, based solely on attenuation data, which had not been done for cortical bone-like samples. This is important as both models are explicitly dependent on pore radius and density, allowing them to be reformulated to consider polydisperse (pores of varying size) structures, which would be expected from *in vitro* experiments. Thus, this work provides the foundation for approaching such real world problems. Furthermore, validating the use of ultrasonic attenuation to perform this analysis is promising, as ultrasound is non-invasive, non-ionizing, and relatively cheap compared to typical bone imaging techniques such as MRI.

We begin by introducing both the ISA and the WT models in Section 3.2, explaining how they model attenuation that is dependent on frequency as well as microstructure. From here, we discuss in detail the numerical simulation that allows us to simulate attenuation data in heterogenous structures in Section 3.3. This is followed in Section 3.4 by the inverse problem formulation where our specific objective is to calibrate both models and estimate the "true" or nominal microstructure. Next, in Section 3.5 we provide the results of solving these inverse problems followed by a discussion. Final conclusions are then presented in Section 4.7.

3.2   Mathematical Models

We seek to infer the microstructure of cortical bone from ultrasonic attenuation data. This requires a mathematical model that relates the microstructural parameters of interest to attenuation measurements. Here we consider two such physics-based models that predict attenuation as a function of pore size and density. The first model considered is based on the Independent Scattering Approximation (ISA), which has been used to characterize trabecular bone [74] as well as air voids in cement [87]. The second, higher-order model, is based on the Waterman Truell approximation and has been used to describe soft 3D acoustic metamaterials [31]. We consider formulations of these models to describe 3D monodisperse structures (fixed pore radius). Here, we give a brief overview of wave propagation in heterogeneous media describing how attenuation is calculated and its dependence on the approximation (ISA or WT) scheme used.

Consider a time-harmonic wave propagating in the direction x. The energy density, $\langle e \rangle$, decays exponentially according to

$$\langle e \rangle(x) \propto e^{-\alpha x}, \tag{3.1}$$

where α is the attenuation coefficient, which we aim to model mathematically. The attenuation is comprised of energy loss due to both scattering when the wave hits a pore, and absorption in the solid bone. Thus,

$$\alpha = \alpha_{\text{abs}} + \alpha_{\text{scatt}}. \tag{3.2}$$

The energy loss due to absorption can be approximated as

$$\alpha_{\text{abs}} = (1 - \xi)\alpha_a(\omega), \tag{3.3}$$

where $\alpha_a(\omega)$ is the absorption coefficient for the matrix (solid bone), and ξ represents the volume fraction which is explicitly calculated using the microstructural parameters pore radius (r) and density (n_s). We see that as pore volume fraction decreases, there is more attenuation due to absorption as there is more solid bone matrix. The energy loss due to scattering can be approximated as

$$\alpha_{\text{scatt}} = -\text{Im}[k_{\text{eff}}], \tag{3.4}$$

where k_{eff} represents the complex, effective wavenumber. The ISA and WT models provide varying levels of approximations of this effective wavenumber. Following [74], consider that in a random scattering medium the coherent field, which is characterized by k_{eff}, is the solution of Dyson's equation. Specifically, the "self-energy" in Dyson's equation incorporates all multiple scattering terms. This is referred to a perturbative method resulting in a Taylor Series [37] solution given by

$$k_{\text{eff}}^2 \approx k_0^2 + 4\pi n_s f_0(\omega; r) + \frac{4\pi^2 n_s^2}{k_{l_0}^2}\left[f_0^2(\omega; r) - f_\pi^2(\omega; r) \right], \tag{3.5}$$

where k_0 is the wavenumber, and f_θ is a scattering function dependent directly on pore radius, r, and θ is the angle of incidence. The simplest approximation, the ISA, includes only the linear terms. The WT model is higher order, including the quadratic terms.

3.2.1 Independent Scattering Approximation

As mentioned, the ISA is considered a first-order approximation in that it considers only the first order terms in the Taylor series expansion. Thus, it estimates the effective wavenumber as

$$k_{\text{eff}}^2 \approx k_0^2 + 4\pi n_s f_0(\omega; r). \tag{3.6}$$

Notice, this representation describes the scattering of the wave as it hits a pore as being independent, i.e., once the wave hits a scatterer (pore), it never returns to the same scatterer. Furthermore by the Optical Theorem [59] we have that the forward scattering function, f_θ, can be related to the scattering cross section γ^{scatt} as

$$\gamma^{\text{scatt}} = \frac{-4\pi}{k}\text{Im}(f_0). \tag{3.7}$$

Thus, for the ISA we have that (see Appendix for details)

$$\frac{1}{2}n_s\gamma^{\text{scatt}}(\omega;r) \approx -\text{Im}\left[\left(k_0^2 + 4\pi n_s f_0(\omega;r)\right)^{1/2}\right], \qquad (3.8)$$

which gives the following ISA attenuation model

$$\alpha(\omega;n_s,r) = \left(1 - \xi\right)\alpha_a(\omega) + \frac{1}{2}n_s\gamma^{\text{scatt}}(\omega;r), \qquad (3.9)$$

where the volume fraction is explicitely calculated as $\xi = \frac{4}{3}\pi r^3 n_s$. Furthermore,

$$\gamma^{\text{scatt}}(\omega;r) = 4\pi \sum_{m=0}^{\infty} \frac{1}{2m+1}[|A_m|^2 + m(m+1)\frac{k_l}{k_s}|B_m|^2], \qquad (3.10)$$

where k_l and k_s are longitudinal and shear wave numbers respectively. The unknown coefficients, A_m and B_m, are determined by solving

$$\begin{bmatrix} H_{11} & H_{12} \\ H_{21} & H_{22} \end{bmatrix} \begin{bmatrix} A_m \\ B_m \end{bmatrix} = \frac{-1}{k_l}(-i)^{m+1}(2m+1)\begin{bmatrix} J_{11} \\ J_{21} \end{bmatrix}, \qquad (3.11)$$

where

$$H_{11} = -\left(m^2 - m - \frac{(k_s r)^2}{2}\right)h_m(k_l r) - 2(k_l r)h_{m+1}(k_l), \qquad (3.12)$$

$$H_{12} = m(m+1)\left[(m-1)h_m(k_s r) - (k_s r)h_{m+1}(k_s r)\right], \qquad (3.13)$$

$$H_{21} = (m-1)h_m(k_l r) - (k_l r)h_{m+1}(k_l r), \qquad (3.14)$$

$$H_{22} = -\left(m^2 - m - \frac{(k_s r)^2}{2}\right)h_m(k_s r) - (k_s r)h_{m+1}(k_s r), \qquad (3.15)$$

and

$$J_{11} = -\left(m^2 - m - \frac{(k_l r)^2}{2}\right)j_m(k_l r) - 2(k_l r)j_{m+1}(k_l r), \qquad (3.16)$$

$$J_{21} = (m-1)j_m(k_l r) - (k_l r)j_{m+1}(k_l r). \qquad (3.17)$$

Note that $j_m(\cdot)$ is the spherical Bessel function of the first kind of order m, and $h_m(\cdot)$ is the spherical Bessel function of the third kind of order m.

3.2.2 Waterman Truell Model

Recall that the Waterman Truell approximation is referred to as second-order due to the truncation of the Taylor series at the second-order terms. Thus, the effective wavenumber is

37

approximated as

$$k_{\text{eff}}^2 \approx k_0^2 + 4\pi n_s f_0(\omega; r) + \frac{4\pi^2 n_s^2}{k_0^2}\left[f_0^2(\omega; r) - f_\pi^2(\omega; r)\right]. \tag{3.18}$$

Notice here we allow for multiple scattering where a wave can revisit a scatter more than once. In far-field, scattering amplitude of the longitudinal wave f_θ is calculated as [85]

$$f_\theta(\omega; r) = \sum_{n=0}^{\infty} -A_m(i^m)P_m(\cos(\theta)), \tag{3.19}$$

where A_m is defined in (3.11), and P_m refers to the Legendre polynomial of degree m.

3.3   FDTD Simulation of Ultrasonic Attenuation Data

In the present work we consider numerically simulated frequency dependent attenuation data. This allows fine-tuned control of the microstructural parameters of interest as well as direct comparison with the monodisperse ISA and WT models' predictions for attenuation. Furthermore, it allows us to consider the attenuation only resulting from scattering. Having nominal or "true" pore radii and densities that we use to generate the data is essential for determining the efficacy of solving the inverse problem to infer these. We now discuss the specifics of this process.

The heterogeneous structure. To generate the random heterogenous structures for a given pore radius (r) and density (n_s), a Monte Carlo method [75] is implemented to randomly distribute pores throughout the media until the desired number of pores is achieved. The algorithm used to generate structures does not allow overlap between pores. The slab dimensions are $200\ mm \times 200\ mm \times 10\ mm$. Material properties of cortical bone and water are assigned to the solid and fluid phases respectively of the binary structures. Pore radius ranges from 50 to $100\mu m$ and pore density from 20 to 50 pores/mm^3.

Emitting pulse. To solve the inverse problem, a frequency sweep is needed to capture the frequency dependent attenuation. To do so, Gaussian pulses with a central frequency within the spectroscopy range of 1 to 8 MHz with 1 MHz intervals and -6 dB bandwidth of 20 percent are transmitted through the medium. We assume 30 receivers are placed throughout the depth of structure to record the signal as it propagates. The emitter and all of the receivers are large such that they cover the width of structure and the pores are uniformly distributed. Hence, the transmitted wave is a plane wave, and the recorded signals are averaged over the whole width of the structure.

Boundary conditions. Perfectly matched layers at the two ends of structure in the wave propagation direction, reduce reflections from those boundaries. Symmetric boundary conditions in the direction perpendicular to the wave propagation are implemented to eliminate diffraction and ensure plane wave transmission.

Simulation parameters. The grid step of $\Delta x = 20\mu m$ exceeds the 20 points per wavelength

spatial sampling requirement proposed by Bossy [24] ensuring the accuracy of the simulation results while keeping the computational costs sufficiently low. Choosing CFL = 0.99, temporal grid step is defined as:

$$\Delta t = 0.99 \frac{1}{\sqrt{d}} \frac{\Delta x}{c_{max}}, \tag{3.20}$$

where Δx is the spatial grid step, c_{max} is the highest speed of sound in the simulation medium and d is the dimension of space ($d = 3$ for 3D simulation). The procedure for measuring the attenuation and spectroscopy are given in [118, 119]. Figure 3.1 depicts the simulated 3D structure with monodisperse, randomly distributed pores.
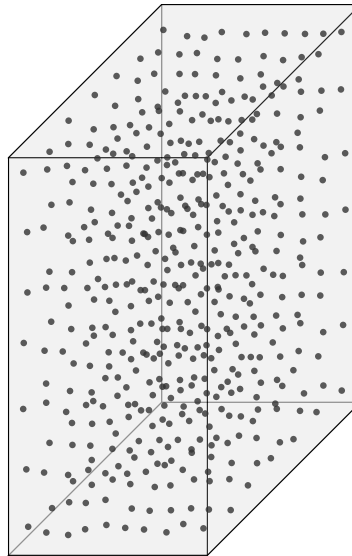
Figure 3.1 Schematic of 3D structures: dimensions 10mm × 20mm × 20mm

3.4 Inverse Problem

Solving the forward problem involves taking the microstructural parameters, pore radius and density, and using the mathematical models (i.e. ISA or WT based) to predict attenuation. Here, we are interested in solving the inverse problem, where one takes attenuation data along with a mathematical model and attempts to estimate the pore radius and density of a sample. To do so, we must formulate and then solve the inverse problem. The first step is to model the data observation process.

Here, we consider that a realization of the data generation procedure is given by

$$y_j = \alpha(\omega_j; n_{s_0}, r_0) + \epsilon_j, \quad j = 1, \dots, N \tag{3.21}$$

where N is the number of frequency points, and ϵ_j's are an i.i.d. error terms. This is referred to

as an absolute error model and results in an ordinary least squares (OLS) formulation [12, 15] of the inverse problem, where all data observations are treated as equally important. The cost function we wish to minimize is given by

$$J(n_s, r) = \sum_{j=1}^{N}[y_j - \alpha(\omega_j; n_s, r)]^2,$$

(3.22)

where y_j represents the attenuation data collected at frequency points ω_j, $j = 1, \ldots, N$, and α represents the corresponding model solution.

Solving this inverse problem results in estimates for pore radius and density, which allow the model to best fit the attenuation data (in terms of the summed squared errors), and are given by

$$(\hat{n}_s, \hat{r}) = \underset{(n_s, r)}{\arg\min} J(n_s, r).$$

(3.23)

3.5 Optimization Results and Discussion

We now present the results of calibrating both the ISA and WT models to the simulated data by solving the inverse problem laid out in Section 3.4. The optimization is done using Matlab's *fmincon*, an interior point algorithm. We considered eleven simulated 3D monodisperse structures with combinations of pore radii (r) ranging from 50 to $100\mu m$ and pore densities (n_s) ranging from 20 to 50 pores/mm^3. Figure 3.2 provides representative results for two specific datasets, where the nominal microstructural parameters are given in the titles and the resulting estimates for each model are given in the inlet boxes.
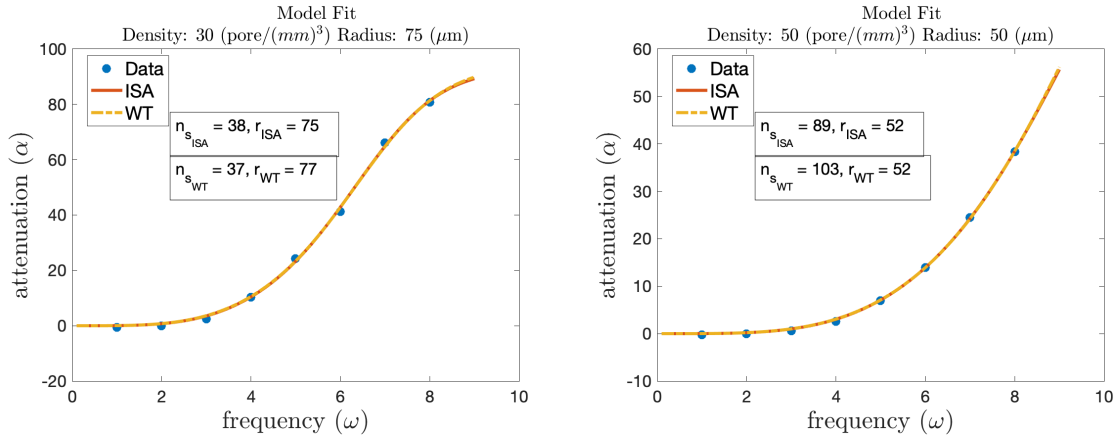
Figure 3.2 Optimized ISA vs WT based models and resulting parameter estimates for nominal pore density $n_s = 30$ pores/mm^3 and radius $r = 75\mu m$ (Left), and nominal pore density $n_s = 50$ pores/mm^3 and radius $r = 50\mu m$ (Right)

We see that the ISA and WT based models produce similar parameter estimates, which correspond well to the nominal parameter values. Furthermore, both calibrated models correspond to the simulated attenuation data. These results validate the use of both the ISA and the WT models for inferring pore radius and density from simulated attenuation data. To fully see how accurately each model predicts microstructure, Figures 3.3 and 3.4 contain comparisons of the nominal parameter values versus the estimates for each model. These result from optimizing both models to the eleven datasets generated from combinations of pore radiuses and densities given above. Notice we consider each parameter, either pore radius or density, separately and the closer the pattern lies to the line $y = x$, the more accurate the estimates.
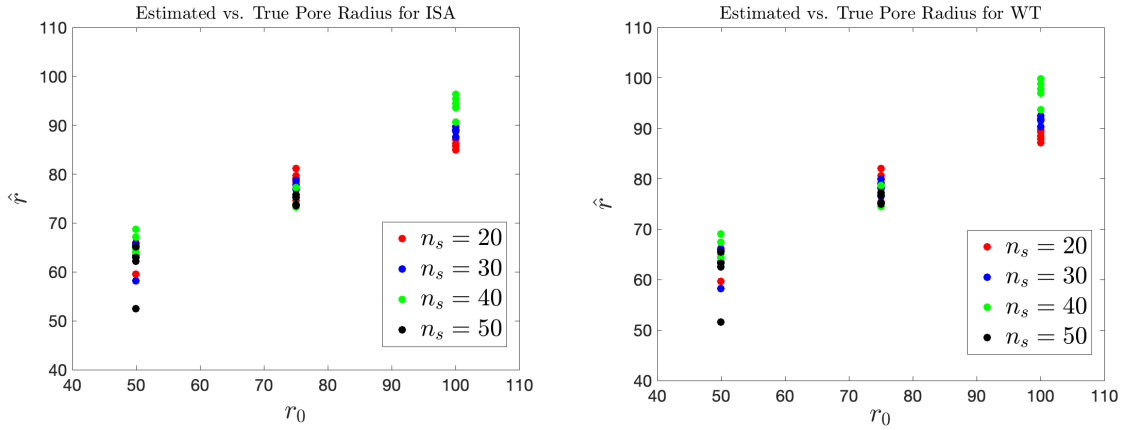
Figure 3.3 True pore radius (r_0) vs. estimated pore radius ($\hat{r}$) for the ISA model (Left) and WT model (Right). The corresponding nominal densities are given in the legend
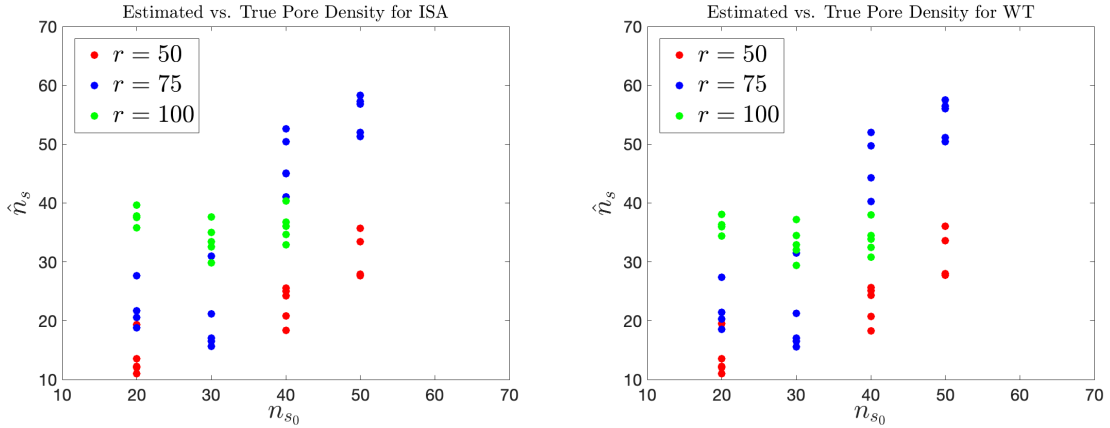
Figure 3.4 True pore density (n_{s_0}) vs. estimated pore density ($\hat{n}_s$) for the for the ISA model (Left) and WT model (Right). The corresponding nominal radii are given in the legend

41

We see from the patterns in Figure 3.3 that the estimates for both models not only align well with each other but also with the nominal pore radii. Figure 3.4 shows a less linear pattern, implying we are less accurate in inferring the nominal pore density. This difficulty in accurately estimating both pore density and pore radius simultaneously results from a high correlation between the two parameters. Correlation coefficients are calculated using the OLS estimate for the covariance matrix following [12], and for all the datasets fall in the interval $[-0.9986, \; -0.9584]$, implying a strong negative linear relationship. This is somewhat expected; notice when calculating the attenuation due to scattering, α_{scatt}, in (3.5), we have pore density (n_s) multiplied by forward scattering pressure (f_θ), which is explicitly a function of pore radius (r). This indicates there could be some tradeoff between these parameter values that result in the same overall attenuation value. However, studies show that pore density is less relevant in predicting fracture risk, due to the fact that for advanced bone porosity, merging of large pores leads to a decrease in pore density [57]. Overall, these results still show acceptable estimates that are informative regarding the microstructure of the simulated samples.

As noted above, both the ISA and WT models produce similar parameter estimates. This is in part due to the fact that their forward model attenuation predictions are similar for the radii, pore density levels, and frequencies considered in this work. Specifically, we see little effects due to second order scattering, and similar forward model predictions result in similar microstructural parameter estimates. It is worth noting that this may not be true in different regimes. Namely, if one expects large amounts of second order scattering, as is the case for high porosity mediums, there may be a more significant difference between the ISA and WT model predictions.

3.5.1 Consistency Across Multiple Realizations

As mentioned in Section 3.3, the data is numerically simulated using a Monte Carlo approach to arranging pores within the geometry. To ensure that the results presented in Section 3.5 aren't dependent on the random geometry, we generate multiple data realizations for a given pore radius and density combination. We can then compare across realizations the calibrated models' attenuation predictions and the resulting parameter estimates. We consider five realizations and provide representative results in Figure 3.5 for samples with a pore radius of $100\mu m$ and density of $40\text{pores}/mm^3$.

We see that the model fit to data as well as the accuracy of the resulting parameter estimates is not dependent upon the random geometry of the sample, as there is little variation across realizations. This further justifies the use of both models for inferring the microstructure of media mimicking cortical bone, by showing the results are not an artifact of the numerical simulation process, but rather dependent on the microstructure itself.
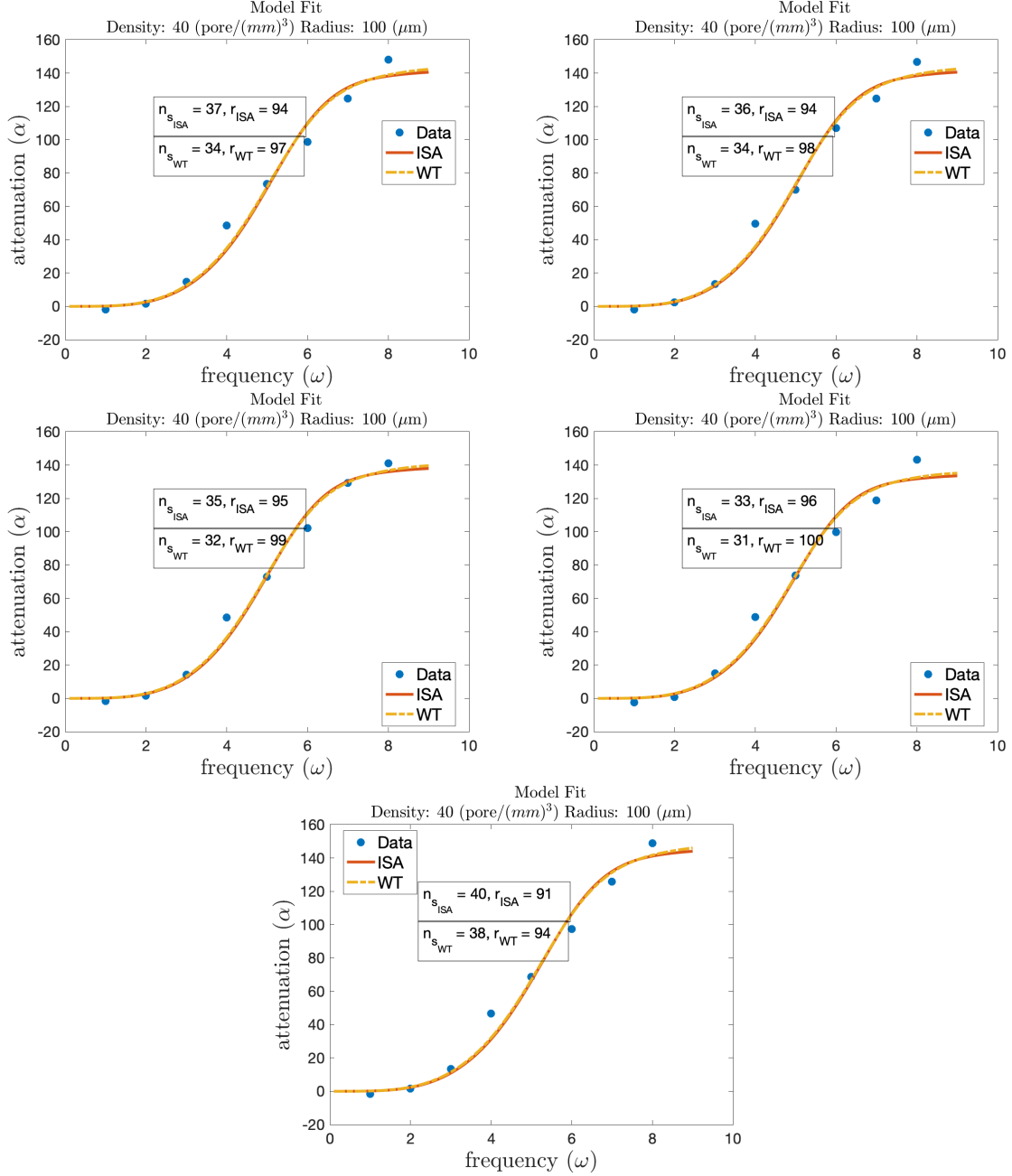
Figure 3.5 Comparison of model calibration across five random geometries with pore density $n_s = 40$ pores/mm^3 and radius $r = 100\mu m$

3.6 Conclusions

Previously used phenomenological modeling of attenuation is not capable of providing detailed information regarding microstructure, such as the distribution of pore radius, and thus cannot be applied to experimental samples. Therefore, physics-based models for attenuation are essential. As shown in the present work, such models can be used to infer porosity in structures mimicking

cortical bone.

We proposed the use of two physics-based models for frequency dependent attenuation, the Independent Scattering Approximation (ISA) and Waterman Truell (WT) models, to describe heterogeneous media mimicking cortical bone. Both models are based on approximation schemes for predicting effective wavenumbers, with the ISA describing independent scattering modes and the higher-order WT model describing higher order multiple scattering. We then generated attenuation data using a numerical FDTD package, allowing us to control the nominal microstructural parameters, pore size and density. The simulated structures contained pores arranged randomly within the 3D media mimicking cortical bone. Based on the data generation process, we formulated an inverse problem to infer the microstructure of samples from attenuation data.

We demonstrated that both calibrated models predicted attenuation values in line with data as well as parameter estimates that closely matched the nominal values. Despite the similar predictions given by the ISA and WT models, investigating both is still of interest, as we may not have this behavior in the next chapter we examine bone samples with varying pore sizes (i.e., polydisperse) are examined. Monodisperse models were chosen here as a first step. This also enabled us to investigate the contributions of pore radius and pore density to attenuation. This is critical because the evolution of these parameters with osteoporosis is not monotonic. In osteopenic bone and for early stages of osteoporosis, both radius and pore density begin to increase. However, at later stages of osteoporosis, pores start to merge into larger pores, which reduces pore density [1]. One of the results of the present study is to show that changes in pore density do not affect ultrasound attenuation as much as changes in pore radius.

We also verified that our results were consistent across realizations of the random geometry of the data simulation process. This validated the use of both models in predicting ultrasonic attenuation in cortical bone-like structures as well as in inferring the microstructure of these samples solely from ultrasound data. In doing so, this work provides a necessary step towards solving more complex, real-world problems, where experimental data is used. In Chapter 4 of this dissertation, we will consider such experimental cortical bone samples in addition to addressing the effects of absorption.

Acknowledgments

CHAPTER

4

A 3D PHYSICS-BASED MODEL FOR POLYDISPERSE SAMPLES AND EXPERIMENTAL DATA

4.1   Introduction

In Chapters 2 and 3 we have discussed in detail the motivation for establishing a quantitative approach for characterizing the cortical bone microstructure. Additionally, we have motivated the importance of this work in diagnosing osteoporosis, a degenerative bone disease affecting millions of people annually. The motivation behind the work in this chapter is to address a more realistic problem formulation. We aim to infer microstructure in a way that translates to to a clinical setting, where real human cortical bone will be evaluated. This results in several significant differences from the work previously done. The first is that we consider variations in pores in human bone. While one can model the pores as being approximately the same size, that

would not allow enough level of resolution to accurately diagnose stages of the disease. Therefore, one aim of this work is to consider polydisperse structures, where pores vary in size. To do so, we must formulate mathematical models for attenuation in these polydisperse structures. Additionally, unlike in numerically simulated structures, one cannot neglect absorption in human bone. Therefore, we account for attenuation due to absorption and scattering. These fundamental changes greatly affect the inverse problem, where we now need to estimate microstructural properties to a level that is adequate for diagnosing osteoporosis. This results in an inverse problem formulation that produces estimates of the Probability Density Function (PDF) on pore size and the scalar absorption coefficient. Ultimately, we wish to validate this methodology using experimental attenuation data gathered from human cadaver bone samples. Success in this phase of work, will provide strong proof-of-concept for applying this methodology to patients *in-vivo*, which is the end goal of this work.

The Independent Scattering Approximation (ISA) has been shown to accurately predict attenuation values in monodisperse 2D structures simulating cortical bone [118]. Additionally, the ISA and Waterman Truell (WT) models have been shown to accurately predict scattering attenuation in 3D simulated bone-like structures, as detailed in Chapter 3. There, both models were used to infer the microstructure of these monodisperse samples, validating their use in inferring pore radius and density from numerically generated (using Finite-Difference Time-Domain software) data. However, attenuation due to absorption was not considered. In dealing with air voids entrapped in cement, forward ISA model propagation using normal distributions on pore size and corresponding volume fractions were shown to align better with experimental data compared to monodisperse model inputs [85]. In formulating polydisperse theoretical models, a formulation for the WT model was provided in [31], however this model lacks dependence upon the PDF on pore size and is therefore not amenable to the inverse problem we wish to solve. Additionally, a probabilistic approach was taken in [50] to address the randomness in scatterer configuration by averaging the statistical ensemble of scatterers and thus deriving average values for wave functions. This is not amenable to our problem as we do not wish to address scatter configuration, but rather randomness in scatterer radius. Most similar to our work is the theoretical polydisperse extension for the WT model presented in [109]. This model introduces the idea of dependence upon a distributed parameter. However, the mathematical form of the polydisperse model differs from the models we implement (see Section 4.2.1), and there are no numerical results presented. This model was, however, used to study the influence of particle size on acoustic wave attenuation. In [71] it was found that the size distribution was an important characteristic that cannot be accounted for by simply substituting the mean of the distribution. The aforementioned work focused solely on forward model propagation for suspensions of solid particles in a fluid matrix. In terms of the inverse problem formulation, extensive analysis into the Prohorov Metric Framework has been done in [5, 9]. This inverse problem methodology was successfully used to detect degradation in ceramic matrix composites [8]. In estimating the air void size distribution in hardened concrete samples, the work [54]

estimated parametric density functions where there were two categories of void size, small and large, each with a normal or log-normal distribution. The previously mentioned work modeled solely ultrasonic scattering attenuation.

To solve a realistic problem of characterizing real human cortical bone, we first develop mathematical models for ultrasound attenuation in these structures. We do so by formulating what we refer to as polydisperse attenuation models, which are dependent upon a PDF on pore radius ($f(r)$) rather than a scalar value (r). There are multiple ways of formulating such models using a probabilistic approach. In this chapter, we highlight three such ways using the Waterman Truell (WT) scattering attenuation model. We also compare these three models in reference to the specific problem we wish to solve. Once we have established theoretical, physics-based models to represent attenuation in polydisperse structures, we can then formulate an appropriate inverse problem. Our approach differs significantly from previous work as we no longer wish to estimate a scalar model parameter, but rather a PDF. This results in an infinite dimensional optimization problem, for which we use the Prohorov Metric Framework to provide a meaningful approximations scheme to formulate a tractable inverse problem. Additionally, we use variational regularization functions to stabilize the ill-posed inverse problem. The last component needed to solve this problem then is the attenuation data. We begin by validating this approach using data generated with the mathematical models and parametric PDFs. We then consider experimental data taken from the femurs of human cadavers. We can establish baseline "true" microstructure (in terms of the PDF on pore radius) using microCT imaging of the bone samples and algorithm to approximate pore size and density within the sample. Subsequently, we solve the inverse problem using the experimental data to establish that we can infer the true PDF on pore size in human cortical bone samples with this approach.

The work in this chapter makes several key contributions. The first is in establishing how to formulate polydisperse models for heterogeneous media that capture the inherently distributed sizes on the heterogeneities. Although we focus on cortical bone, the proposed framework has broad applications to any media where the scatters are not assumed to be of the same size. Furthermore, we validated these formulations for two scattering models, the ISA and WT, which are widely used to model heterogeneous media via ultrasound. We illustrated that not only do these models allow us to predict attenuation in such structures, but also to infer microstructural properties by solving an inverse problem. Implementing the variational regularization in conjunction with the Prohorov Metric Framework is another area of novelty in this work and showed to be important in attaining accurate PDF estimates. As the Prohorov Metric Framework is widely used in formulating inverse problems for biological applications, this technique could be useful in addressing ill-posed problems and when we only have access to sparse noisy data. The level of resolution in inferring the microstructure of the cortical bone is also a key contribution. Not only do we attain distribution level information, but we do so in a nonparametric way that does not impose restrictive structures on the PDF (i.e., normal, beta, or log-normal distributions). Overall, we have developed an approach for inferring cortical bone microstructure at the level

required for diagnostic purposes. We validated these results using real human cortical bone data. This methodology has the potential to translate to clinical settings where patients can be assessed in real time *in-vivo* using non-invasive, non-ionizing, and widely available ultrasound. More broadly, this work has applications related to the quantification of nonhomogeneous media using ultrasound waves.

This chapter is organized as follows. We begin by introducing the required background from probability for modeling polydisperse structures in Section 4.2. We present various polydisperse formulations of the WT model for scattering attenuation in Section 4.2.1 and introduce the polydisperse WT and ISA models for total attenuation in Section 4.3.1. In Section 4.4 we lay out the inverse problem formulation and introduce both the approximation scheme and regularization functions considered in this work. Following this, we introduce the experimental setup used to collect *in-vitro* attenuation data from human cadaver cortical bone samples in Section 4.5. The computational results using both simulated and experimental data are presented in Section 4.6 Overall conclusions are given in Section 4.7.

4.2   Mathematical Models

We seek to model frequency dependent ultrasonic attenuation in polydisperse cortical bone. The ultimate goal is to infer bone microstructure, and therefore the formulation of our polydisperse model should be conducive for solving an inverse problem. We accomplish this by reformulating two previously established models for monodisperse cortical bone-like structures which were discussed in Chapter 3: the Independent Scattering Approximation (ISA) and the Waterman Truell (WT) models. Recall that these models are obtained via first and second order Taylor series approximations of the effective wave number. In Chapter 3, both of these models were shown to be effective in inferring microstructure for simulated structures with a fixed pore size. Our goal is to reformulate these models to predict attenuation in polydisperse structures.

First, note that for monodisperse samples the attenuation depends on a fixed pore radius r. In contrast, in polydisperse samples the pore radius is a random variable, $R : (\Omega, \mathscr{A}, \mathbb{P}) \to (\Omega_{\mathrm{R}}, \mathscr{B}(\Omega_{\mathrm{R}}))$. Here Ω is a sample space, $\mathscr{A}$ a sigma-algebra on Ω, and $\mathbb{P}$ a probability measure. Furthermore, Ω_{R} is a closed and bounded subset of $[0, \infty)$, and $\mathscr{B}(\Omega_{\mathrm{R}})$ the Borel sigma-algebra on Ω_{R}. The law of R is a probability measure $\mathscr{L}_{\mathrm{R}}$ on Ω_{R} defined by

$$\mathscr{L}_{\mathrm{R}}(E) = \mathbb{P}(R \in E), \quad E \in \mathscr{B}(\Omega_{\mathrm{R}}),$$

which is uniquely characterized by the corresponding cumulative distribution function (CDF), $\mathscr{F}_{\mathrm{R}}$, given by $\mathscr{F}_{\mathrm{R}}(r) = \mathscr{L}_{\mathrm{R}}([-\infty, r))$; see [115]. We consider a set of admissible probability laws on Ω_{R}, which we denote by $\mathscr{P}(\Omega_{\mathrm{R}})$ that describe plausible distribution laws for R. Each element of $\mathscr{P}(\Omega_{\mathrm{R}})$ has a corresponding CDF $\mathscr{F}_{\mathrm{R}}$. Assuming the elements of $\mathscr{P}(\Omega_{\mathrm{R}})$ are absolutely continuous with respect to the Lebesgue measure, they admit probability density functions (PDFs). That is,

for each $\mathscr{L}_R \in \mathscr{P}(\Omega_R)$, we have a density function f_R that satisfies,

$$\mathscr{L}_R(E) = \int_E f_R(r)\,dr, \quad E \in \mathscr{B}(\Omega_R).$$

Henceforth, we shall omit the subscript R from the CDFs and PDFs and, as is common, denote the values taken by R as r. Our goal is to formulate polydisperse attenuation models that depend upon a density function $f(r)$. Having such a model allows us to formulate and solve an inverse problem that uses the model and experimental data to estimate this PDF, providing valuable information about the microstructure of cortical bone.

There are several ways to reformulate a monodisperse model to represent the polydisperse structures depending on the level of averaging desired. In Section 4.2.1 we derive three polydisperse model formulations using the scattering portion of the WT attenuation model. Note that we only focus on scattering attenuation because this is where the differences in the various formulations arise. Then, in Section 4.3.1, we present the polydisperse formulation of the ISA model considered in this work.

4.2.1 Averaging Approaches for Deriving Polydisperse Models

To understand how polydisperse formulations can arise based on various levels of averaging, we first consider the monodisperse WT model form [109], which presents attenuation as a sum of contributions due to scattering and attenuation, and is given as follows,

$$\begin{aligned}
\alpha_{\mathrm{wt}}(\omega; n_s, \alpha_a, r) &= \alpha_{\mathrm{abs}} + \alpha_{\mathrm{scatt}} && (4.1) \\
&= (1 - \xi)\alpha_a\omega - \mathrm{Im}[k_{\mathrm{eff}}],
\end{aligned}$$

where ω is frequency, r is pore radius, α_a is the absorption coefficient, ξ is the volume fraction, and the complex effective wavenumber is approximated as

$$k_{\mathrm{eff}}^2 \approx k_0^2 + 4\pi n_s f_0(\omega; r) + \frac{4\pi^2 n_s^2}{k_0^2}\left[f_0^2(\omega; r) - f_\pi^2(\omega; r)\right].$$

Noting the definition of volume fraction, ξ, and incorporating the wavenumber approximation, we have the following attenuation model,

$$\alpha_{\mathrm{wt}}(\omega; n_s, \alpha_a, r) = \left(1 - \frac{4}{3}\pi r^3 n_s\right)\alpha_a\omega$$

$$-\mathrm{Im}\left[k_0^2 + 4\pi n_s f_0(\omega; r) + \frac{4\pi^2 n_s^2}{k_0^2}\left[f_0^2(\omega; r) - f_\pi^2(\omega; r)\right]\right]^{1/2}, \quad (4.2)$$

where k_0 is the reference wavenumber, n_s is pore density, and $f_\theta(\omega; r)$ is a scattering function. This scattering function is defined in (3.19) in Chapter 3.

Defining an average α_{abs} is straightforward—we can consider taking the expectation over r.

On the other hand, the scattering attenuation in (4.2) depends on pore radius r through the r-dependent scattering function. As a result, there are several ways to express the average effects of a randomly distributed pore radius on the scattering attenuation model. The first model we consider consists of taking the expected value of the monodisperse WT model with respect to the pore radius, distributed according to $f(r)$:

$$\bar{\alpha}_{\text{scatt}}^{(1)}(\omega; n_s, \alpha_a, f) = \int_{\Omega_{\text{R}}} \alpha_{\text{scatt}}(\omega; n_s, \alpha_a, r) f(r) dr$$

$$= \int_{\Omega_{\text{R}}} -\text{Im}\left[k_0^2 + 4\pi n_s f_0(\omega; r) + \frac{4\pi^2 n_s^2}{k_0^2}\left[f_0^2(\omega; r) - f_\pi^2(\omega; r) \right] \right]^{1/2} f(r) dr. \quad (4.3)$$

Here, Ω_{R} denotes the set of admissible pore radii.

One can also consider an average k_{eff}^2,

$$\langle k_{\text{eff}}^2 \rangle = \int_{\Omega_{\text{R}}} k_0^2 + 4\pi n_s f_0(\omega; r) + \frac{4\pi^2 n_s^2}{k_0^2}\left[f_0^2(\omega; r) - f_\pi^2(\omega; r) \right] f(r) dr,$$

which leads to the second formulation of the polydisperse WT model:

$$\begin{aligned}
\bar{\alpha}_{\text{scatt}}^{(2)}(\omega; n_s, \alpha_a, f) &= -\text{Im}\left[\langle k_{\text{eff}}^2 \rangle \right]^{1/2} \\
&= -\text{Im}\left[\int_{\Omega_{\text{R}}} k_0^2 + 4\pi n_s f_0(\omega; r) + \frac{4\pi^2 n_s^2}{k_0^2}\left[f_0^2(\omega; r) - f_\pi^2(\omega; r) \right] f(r) dr \right]^{1/2} \\
&= -\text{Im}\left[k_0^2 + \int_{\Omega_{\text{R}}} 4\pi n_s f_0(\omega; r) + \frac{4\pi^2 n_s^2}{k_0^2}\left[f_0^2(\omega; r) - f_\pi^2(\omega; r) \right] f(r) dr \right]^{1/2} (4.4)
\end{aligned}$$

Alternatively, one can consider an average scattering function,

$$\langle f_\theta \rangle = \int_{\Omega_{\text{R}}} f_\theta(\omega; r) f(r) dr.$$

This leads to the third formulation of the polydisperse model given as

$$\begin{aligned}
\bar{\alpha}_{\text{scatt}}^{(3)}(\omega; n_s, \alpha_a, f) &= -\text{Im}\left[k_0^2 + 4\pi n_s \langle f_0 \rangle + \frac{4\pi^2 n_s^2}{k_0^2}\left[\langle f_0 \rangle^2 - \langle f_\pi \rangle^2 \right] \right]^{1/2} \\
&= -\text{Im}\left[k_0^2 + 4\pi n_s \int_{\Omega_{\text{R}}} f_0(\omega; r) f(r) dr \right. \\
&\quad + \left. \frac{4\pi^2 n_s^2}{k_0^2}\left[\left(\int_{\Omega_{\text{R}}} f_0(\omega; r) f(r) dr \right)^2 - \left(\int_{\Omega_{\text{R}}} f_\pi(\omega; r) f(r) dr \right)^2 \right] \right]^{1/2},
\end{aligned}$$

which is the formulation proposed by [109].

The choice of the polydisperse model formulation is at the discretion of the modeler. Although all three models represent valid polydisperse formulations, differing only in the method of

averaging over r, one model may be more or less conducive to solving a specific problem. For example, one model may better allow us to solve the forward or inverse problems, relative to the other models. In the following Section, (4.3), we examine how these models differ in the regime of our problem.

4.3 Comparison of Polydisperse WT Scattering Attenuation Models

Recall that our goal is to estimate the nominal PDF on pore radius. Here, we investigate the viability of these models in solving this estimation problem. We do so by comparing the respective forward model solutions as well as their sensitivities. In general, the sensitivity of the model with respect to this quantity of interest affects the confidence one has in the resulting estimate. Thus, one question of interest is how sensitive are the WT polydisperse models (4.3) - (4.5) to the PDF of interest. To investigate the models' forward solutions as well as their sensitivity with respect to the PDF of interest, we consider a parametric Beta density function given as

$$f_{\text{Beta}}(r) = \frac{(r-a)^{p-1}(b-r)^{q-1}}{B(p,q)(b-a)^{p+q-1}}, \quad a \leq r \leq b; \quad p, q > 0, \tag{4.5}$$

where p, q are referred to as the shape parameters and $B(p,q) = \int_0^1 t^{p-1}(1-t)^{q-1}\, dt$. We then perform local sensitivity analysis of the models with respect to the Beta parameters p and q. First, Figure 4.1 shows the difference in forward model $(\alpha_{\text{scatt}}^{(i)})$ solution with an input Beta density function with $p = 2$ and $q = 4$, where $\alpha_a = 0$ and $n_s = 150$ pore$/(mm^3)$. We see that all three model formulations produce very similar forward model solutions.
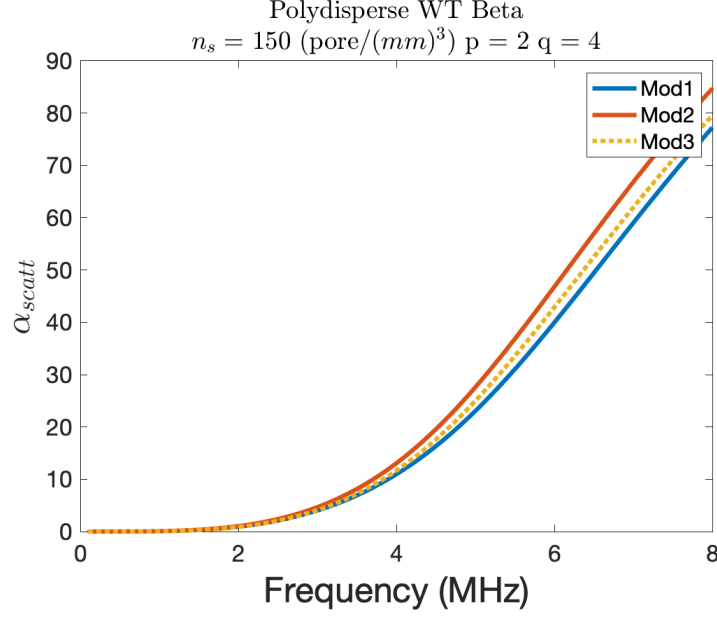
Figure 4.1 Comparison of forward model solutions with an input Beta distribution with p (Left) and q (right)

Next, we determine the models' sensitivity with respect to the Beta parameters. Using finite differences we can calculate the sensitivity of the model with respect to the Beta distribution parameters as

$$
\frac{\partial \alpha^{(i)}(\omega; \alpha_a, f_{\text{Beta}}(r, p, q))}{\partial p} \approx \frac{\alpha^{(i)}(\omega; \alpha_a, f_{\text{Beta}}(r, p + \delta p, q)) - \alpha^{(i)}(\omega; \alpha_a, f_{\text{Beta}}(r, p, q))}{\delta p}
$$
$$
\frac{\partial \alpha^{(i)}(\omega; \alpha_a, f_{\text{Beta}}(r, p, q))}{\partial p} \approx \frac{\alpha^{(i)}(\omega; \alpha_a, f_{\text{Beta}}(r, p, q + \delta q)) - \alpha^{(i)}(\omega; \alpha_a, f_{\text{Beta}}(r, p, q))}{\delta q},
$$

where δp and δq are strictly positive step lengths for p and q respectively. Figure 4.2 shows sensitivities of each of the three models with respect to the Beta distribution parameters, where $p = 2$, $q = 4$, and $\delta p = \delta q = 1e - 04$.
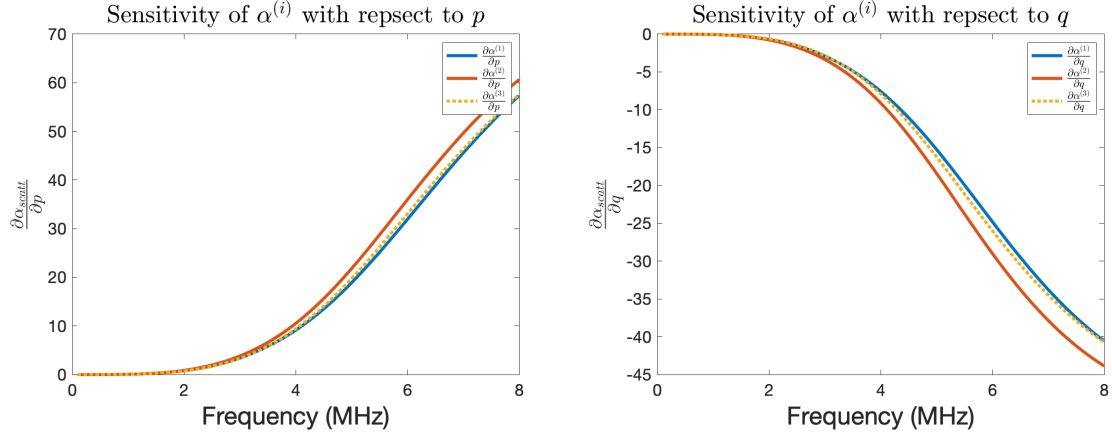
Figure 4.2 Comparison of model sensitivity versus frequency with respect to p (Left) and q (right)

Although all three models show similar sensitivity with respect to the Beta distribution parameters, we see a slight increase in sensitivity for Model 2 formulation (4.4).

In our computations we have performed the parameter inversion for the ISA, which is equivalent to Model 1 formulation of the WT without the quadratic terms in k_{eff}. Furthermore, the inverse problem has been solved using Model 2 formulation of the WT. Both produced very similar estimates of the PDF, indicating that the estimation of the PDF is not dependent upon the model formulation, in the present application. However, the pros and cons of the different model formulations in different scenarios is an interesting avenue for future work.

4.3.1 Polydisperse ISA and WT Model Formulation

Here, we provide both the ISA and WT models for total attenuation ($\alpha_{\text{scatt}} + \alpha_{\text{abs}}$) that are considered in this work. First, in formulating the polydisperse version of the ISA, we rely on the monodisperse equations given in [114]. Specifically, we use $\alpha_{\text{scatt}}(\omega; n_s, r) = n_s \gamma_{\text{scatt}}(\omega; r)/2$, where γ^{scatt} is the scattering cross section. We note that in this case, the polydisperse reformulation is straightforward and mirrors that in (4.3). The polydisperse ISA model is given as

$$\bar{\alpha}_{isa}(\omega; \alpha_a, f) \;=\; \alpha_a \omega \left(1 - \int_{\Omega_R} \frac{4}{3} \pi r^3 n_s f(r) dr \right) + \frac{1}{2} \int_{\Omega_R} \gamma^{\text{scatt}}(\omega; r) n_s f(r) dr, \qquad (4.6)$$

where $\gamma^{\text{scatt}}(\omega; r)$ was previously defined in (3.10) of Chapter 3.

Next, we present the WT polydisperse model for total attenuation. We note that the derivation for the scattering attenuation is given above and concludes with (4.4). Thus, our WT model is

given as

$$\bar{\alpha}_{wt}(\omega; \alpha_a, f) = \alpha_a \omega \left(1 - \int_{\Omega_R} \frac{4}{3} \pi r^3 n_s f(r) dr \right)$$

$$- \text{Im} \left[k_0^2 + \int_{\Omega_R} 4\pi n_s f_0(\omega; r) + \frac{4\pi^2 n_s^2}{k_0^2} \left[f_0^2(\omega; r) - f_\pi^2(\omega; r) \right] f(r) dr \right]^{1/2}. \tag{4.7}$$

Note that in the polydisperse models given by (4.6) and (4.7), the dependence on pore density n_s has been omitted, as this parameter will be fixed when solving the inverse problems. The choice to fix this parameter is due to identifiability issues when trying to simultaneously estimate both n_s and f. Furthermore, previous studies show that pore density is not significant in determining osteoporosis levels [57, 102].

Figure 4.3 illustrates the forward model solutions of both the polydisperse ISA and WT models. On the left is a graph of the input PDF, $f_{\text{beta}}(r)$, which is given by a beta density function with shape parameters $p = 3$ and $q = 8$ (see Section 4.6.1 for more details). The right figure provides the forward model solutions in the case where pore density is $n_s = 130$ pores/mm^3 and $\alpha_a = 9.99$ dB/(cm MHz).
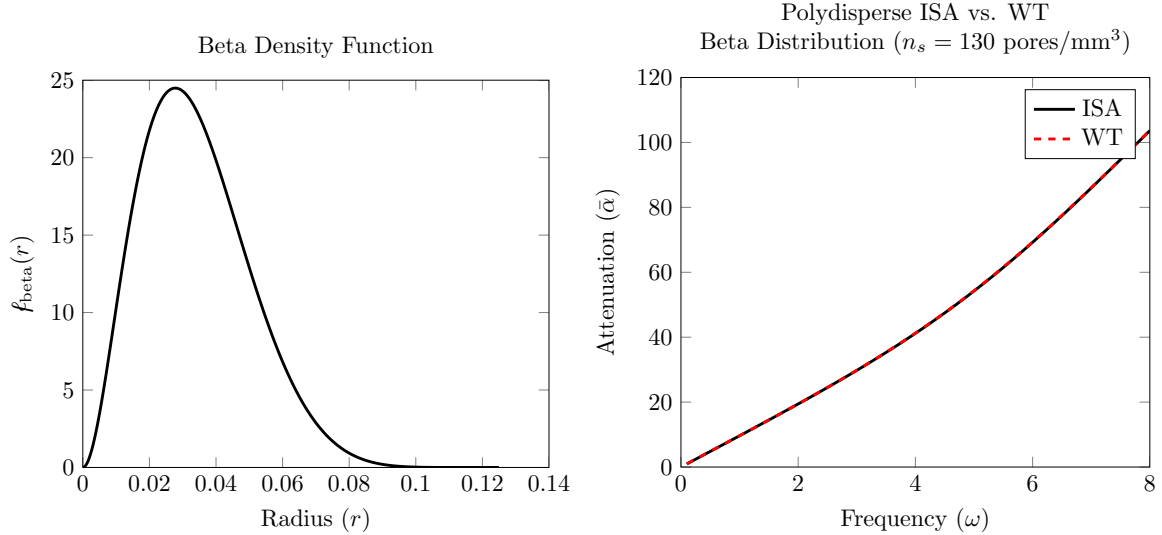
Figure 4.3 Left: $f_{\text{beta}}(r)$ Right: Resulting forward model solutions of the polydisperse ISA and WT models

We see from Figure 4.3 that in this example, the ISA and WT forward model solutions produce nearly identical results. This is a notable observation as this indicates that both models may produce similar inverse problem estimates. As a result, it is helpful to understand why the correspondence between these two models exists. The main reason is that attenuation due to absorption (α_{abs}) dominates in the regime of our problem, and this term is identical for both the

ISA and WT models. However, the attenuation due to scattering is not negligible. In comparing the scattering term (α_{scatt}) for the ISA and WT, we see that these values are similar. The reason for this correspondence is that second order multiple scattering is insignificant in this example. We note this may not always be the case as the scattering regime is dependent upon the specific microstructure. Therefore, we cannot yet conclude that the higher order terms of the WT provide no additional information in terms of reconstructing the nominal PDF on pore size. Thus, a full comparison of the two models' inverse problem solutions will be examined in this work.

4.4   Inverse Problem

We use the mathematical models described in Section 4.2 along with measurement data to solve inverse problems, producing estimates of the underlying PDF for pore radius along with the scalar absorption coefficient (α_{abs}). To facilitate the estimation of this PDF, we rely on the Prohorov Metric Framework (PMF) [5, 12, 84], which is discussed briefly in Section 4.4.1. Following that in Section 4.4.2 we discuss the inverse problem formulation using our adopted approximation scheme, along with all relevant constraints. Lastly, in Section 4.4.3, we discuss a regularization technique to address the ill-posed nature of the inverse problem.

4.4.1   The Prohorov Metric Framework

Recall that the distribution law of the pore radius is an element of the set $\mathscr{P}(\Omega_{\text{R}})$ of admissible probability measures on $(\Omega_{\text{R}}, \mathscr{B}(\Omega_{\text{R}}))$. As mentioned before, we consider the case where elements of $\mathscr{P}(\Omega_{\text{R}})$ are absolutely continuous with respect to the the Lebesgue measure. Therefore, each element of $\mathscr{P}(\Omega_{\text{R}})$ is fully described by its CDF, which has an associated PDF. The inverse problem is then formulated by seeking a PDF for the pore size, which is consistent with the governing model and measurement data. Notice that the set of admissible PDFs being a subset of $L^1(\Omega_{\text{R}})$, we have an infinite-dimensional optimization problem. The PMF provides a rigorous approximation scheme for tackling such inverse problems. Namely, assuming existence of an underlying PDF, $f_0(r)$, that generates the data, one can prove convergence of the solution of the discretized problem to $f_0(r)$ in the limit as the number of data points and dimension of the discretization go to infinity [5, 12, 84]. In this work, we adopt the discretization of $\mathscr{P}(\Omega_{\text{R}})$, from the PMF and consider

$$\mathscr{P}_n(\Omega_{\text{R}}) = \left\{ \mathscr{L} \in \mathscr{P}(\Omega_{\text{R}}) \middle| \frac{d\mathscr{L}}{d\lambda} = \sum_{m=1}^{n} c_m l_m(r), c_m \geq 0 \text{ and } \sum_{m=1}^{n} c_m \int_{\Omega_{\text{R}}} l_m(r) dr = 1 \right\},$$

where for each $\mathscr{L} \in \mathscr{P}_n(\Omega_{\text{R}})$ we consider the corresponding PDF $f = \frac{d\mathscr{L}}{d\lambda}$, which is the Radon–Nikodym derivative of $\mathscr{L}$ with respect to the Lebesgue measure, λ. Here, c_m's represent the spline coefficients and l_m's are the linear splines (see Section 4.4.3).

In the PMF, convergence of probability measures is studied with respect to the Prohorov Metric, which we briefly recall here, for readers convenience. For every closed subset $\mathbb{F}$ of Ω_{R},

we denote $\mathbb{F}^\epsilon = \{r \in \Omega_R : \inf_{\hat{r} \in \mathbb{F}} |r - \hat{r}| < \epsilon\}$. The Prohorov distance between two probability measures P and G is defined as

$$\rho(P, G) = \inf \{\epsilon > 0 : G(\mathbb{F}) \leq P(\mathbb{F}^\epsilon) + \epsilon \text{ and } P(\mathbb{F}) \leq G(\mathbb{F}^\epsilon) + \epsilon, \text{ for all } \mathbb{F} \text{ closed in } \Omega_R\}.$$

While the definition of the Prohorov metric is rather abstract, it does have desirable theoretical properties. Specifically, we have that convergence in Prohorov metric is equivalent to weak* convergence. That is, if for all n we have $G_n, G \in \mathscr{P}(\Omega_R)$, then $\lim_{n \to \infty} \rho(G_n, G) = 0$ if and only if

$$\int_{\Omega_R} h(r) dG_n(r) \to \int_{\Omega_R} h(r) dG(r), \text{ for any } h \in C_B(\Omega_R),$$

see, e.g., [5, 12, 19], for details. Additionally, we note that in this application we are specifically interested in the PDF, $f(r)$. The discretization we adopt directly approximates the PDF and provides convergence of both the PDF and CDF; whereas other approximation schemes may only provide convergence in CDF; see [9].

4.4.2 Inverse Problem Formulation

We use the mathematical models given in Section 4.2 to approximate the physical process of attenuation. However, one must also model the observation process to account for errors in data acquisition. This is done using a statistical model. We use an absolute error model

$$y_j = \bar{\alpha}(\omega_j; \alpha_a, f) + \epsilon_j, \quad j = 1, \dots, N, \tag{4.8}$$

where ω_j's are frequencies, y_j are the corresponding attenuation measurements, N represents the number of frequency points, and ϵ_j's are independent and identically distributed (iid) error terms. This leads to an Ordinary Least Squares (OLS) formulation of the inverse problem [12, 15], which we discuss next. The inverse problem uses (4.8) to estimate the unknown absorption coefficient α_a and the PDF, $f(r)$, of pore radii.

As mentioned above, we derive our approximation scheme from the PMF. Thus, our density function is approximated using piecewise linear splines as

$$f(r) \approx f_n(r) = \sum_{m=1}^n c_m l_m(r), \tag{4.9}$$

where again c_m represent the spline coefficients, l_m represent the basis functions given by linear splines, and n represents the number of basis functions. Thus, the inverse problem is to determine

$$(\hat{\alpha}_a, \hat{\mathbf{c}}) = \underset{(\alpha_a, \mathbf{c}) \in (0, \infty) \times \mathscr{R}_s^n}{\arg \min} J(\alpha_a, \mathbf{c}),$$

where J is the cost functional

$$J(\alpha_a, \mathbf{c}) = \sum_j (\bar{\alpha}(\omega_j; \alpha_a, \mathbf{c}) - y_j)^2 + \gamma G(\mathbf{c}). \tag{4.10}$$

Here $G(\mathbf{c})$ is a regularizing penalty function, which we discuss in more detail in Section 4.4.3, and $\gamma > 0$ is a regularization parameter. Furthermore,

$$\mathscr{R}_s^n = \left\{ \mathbf{c} \in \mathbb{R}_{\geq 0}^n : \sum_{m=1}^n c_m \int_{\Omega_R} l_m(\xi) d\xi = 1 \right\}.$$

Notice this results in an optimization problem with linear equality constraints.

4.4.3 Regularization Functions

The regularization function $G(\boldsymbol{c})$ in (4.10) is included to address the ill-posed nature of the problem. In this work, we consider two types of regularizations based on L^2 and H^1 penalties, which we describe next. Let us first consider the linear splines used to approximate the PDF. We use a uniform partition of Ω_R. Namely, we consider grid points $\{r_0, \ldots, r_{n+1}\} \subset \Omega_R$, where our fixed step is given by $h = r_{i+1} - r_i$ for $i = 1, \ldots, n$. Then we use

$$l_i(r) = \begin{cases} \frac{r - r_{i-1}}{h}, & r \in [r_{i-1}, r_i], \\ \frac{r_{i+1} - r}{h}, & r \in [r_i, r_{i+1}], \\ 0, & \text{elsewhere}, \end{cases} \tag{4.11}$$

for $i = 1, \ldots, n$. In the present work, we assume the PDF vanishes on the end-points, i.e., $c_0 = c_{n+1} = 0$. Therefore, we do not consider the half-splines $l_0(r)$ and $l_{n+1}(r)$.

Identifying the vector $\boldsymbol{c}$ with the corresponding f_n, we write the L^2 regularization function as

$$G_{l^2}(\boldsymbol{c}) := G_{l^2}(f_n) = \int_{\Omega_R} |f_n(r)|^2 \, dr = \mathbf{c}^T \mathbf{M} \mathbf{c}, \tag{4.12}$$

where the mass matrix $\mathbf{M}$ is defined according to $M_{ij} = \int_{\Omega_R} l_i(r) l_j(r) \, dr$, $i, j = 1, \ldots, n$. Lastly, we consider an H^1 regularization to enforce smoothness in the estimated PDF, which is reasonable as we would expect the nominal PDF on pore radius to be differentiable. This regularization function is given as

$$G_{h^1}(\boldsymbol{c}) := G_{h^1}(f_n) = \int_{\Omega_R} |\nabla f_n(r)|^2 dr = \mathbf{c}^T \mathbf{K} \mathbf{c}, \tag{4.13}$$

where the stiffness matrix $\boldsymbol{K}$ is defined according to $K_{ij} = \int_{\Omega_R} l_i'(r) l_{i+1}'(r) dr$.

It is worth noting that these penalties can be combined. For example, we can consider

$$\gamma_{l^2} G_{l^2}(f_n) + \gamma_{h^1} G_{h^1}(f_n). \tag{4.14}$$

which encourages smoothness in the estimated PDF in addition to penalizing its L^2 norm. The derivations of each of these regularization functions is provided in Appendix B.

4.5 Experimental Data Acquisition

To validate the use of the polydisperse models for predicting both attenuation and the distribution on pore radius in human cortical bone samples, experimental data is needed. In addition to acquiring experimental attenuation data, CT scans of the bone samples are also taken, allowing us to determine the "true" or nominal distribution on pore radius for each sample. This allows evaluating the accuracy of our estimated PDFs and aids in calibrating the regularization parameters, γ. We provide brief overview of this experimental setup in Section 4.5.1. Following this, we discuss how the CT images of the samples are processed and provide the algorithm we developed to determine the porosity of the 3D sample from the 2D CT scans in Section 4.5.2. We provide the computational results of using this experimental data to solve inverse problems in Section 4.6.2.

4.5.1 Experimental Setup

We have cortical bone samples from the femurs of eight human cadavers. We cut these bone samples in $5 \times 4 \times 3$mm cubes; see Figure 4.4 (Left). Transducers with central frequencies of 5 and 10 MHz are used to transmit the ultrasonic pulse through the bone sample (Figure 4.4 Right). The amplitude of the wave after traveling through the bone sample is then measured. One can then calculate attenuation. A Fast Fourier Transform with a Gaussian window is then used to convert the attenuation to the time domain. A schematic of this is given in Figure 4.5.
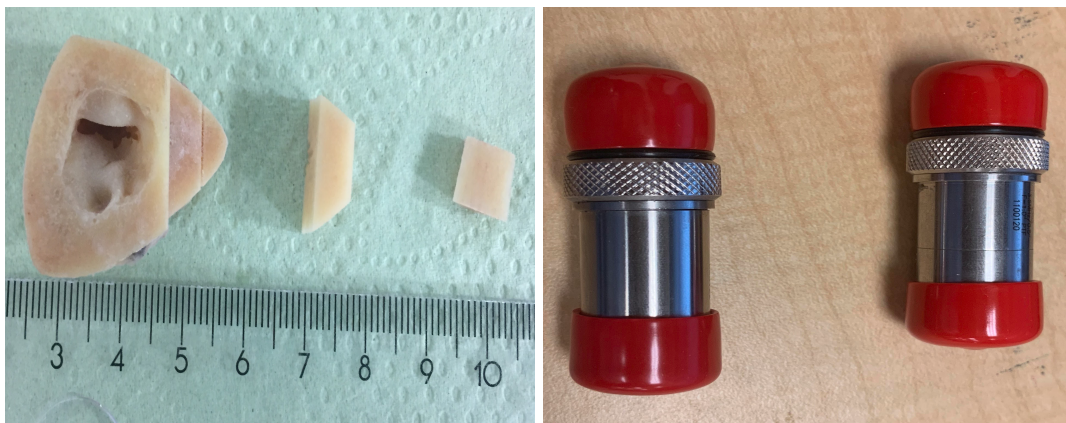
Figure 4.4 Left: Experimental cortical bone samples. Right: transducers
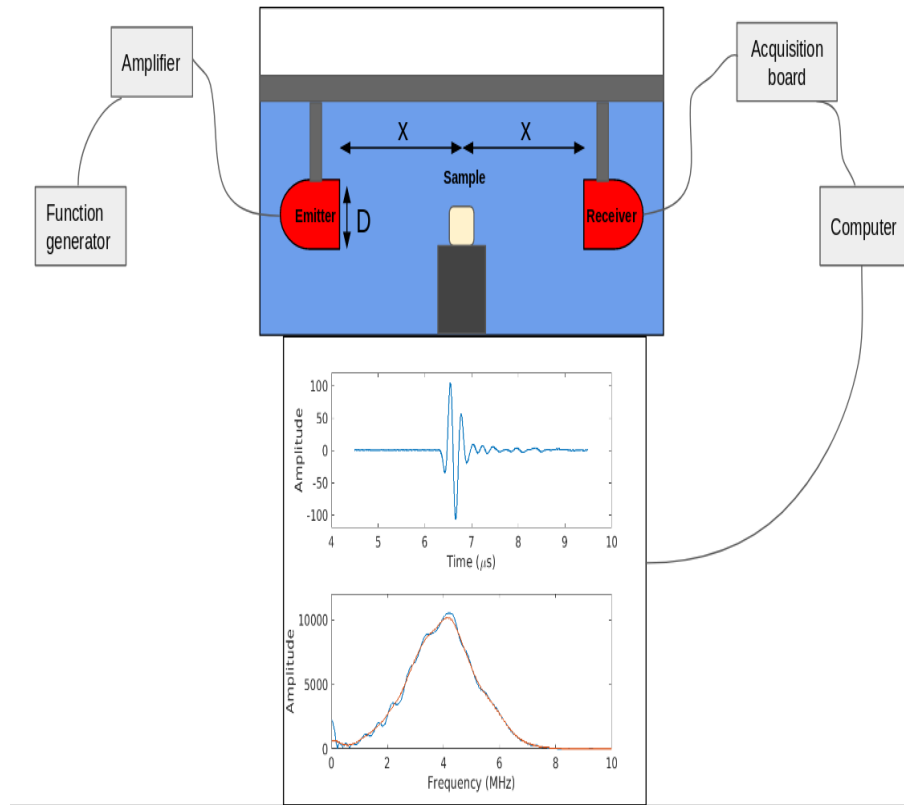
Figure 4.5 Schematic for experimental setup

4.5.2   Image Processing of CT Scans

Here, we discuss how the 2D CT scans of the cortical bone samples are processed to determine a nominal or "true" distribution on pore radius. This is not essential to solving the inverse problem but is done to provide a way of examining the effectiveness of the estimation strategy. Suppose that a result scan produces a bone image like that given in Figure 4.6.
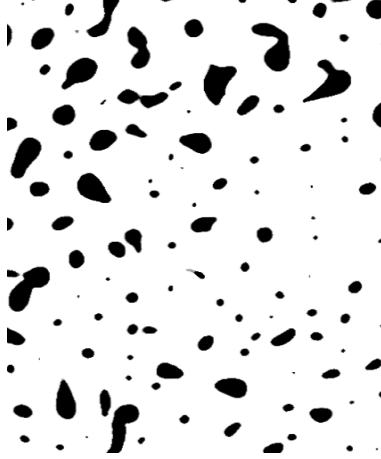
Figure 4.6 2D micro CT image of experimental cortical bone sample

We convert each 2D scan into a binary structure, differentiating between pixels corresponding to bone versus pixels corresponding to pores [67]. Then, pore volume fraction (ξ) can be obtained by dividing the pore volume (the summation of all the pore pixels) by the total volume (number of pixels) of the sample. Next, we estimate the radius of every pore within the sample by determining the number of 3D pores (or objects) from the binary structures. In cortical bone, we see the phenomenon of having one large interconnected pore, resembling a scaffold with numerous branches. We set a volume threshold of 20000 pixels, such that any object with smaller volume is considered a separate pore. Using this threshold, first, the independent pores that do not belong to any larger network are automatically detected based on the connectivity of the pixels in the 3D structure. As the interconnected network of pores cannot be estimated as an individual object, an algorithm based on the connectivity of pore cross sections between the 2D layers of the bone samples must recognize the branches as separate objects and find the equivalent pore size for each branch. We proceed as follows:

1. Consider 2D transverse layers ($\text{layer}_1, \dots, \text{layer}_i$) of the 3D sample, where i is the number of 2D slices.

2. Beginning at layer 1, label each pore cross section $\text{pore}_1, \dots, \text{pore}_j$, where j is the total number of pore cross sections in that layer.

3. Consider layer 2 and compare the pore cross sections of that layer to those of the same location in the previous layer.

4. Repeat steps 1 and 2 for all i layers of the sample.

5. If a given layer, $x + 1$, contains bone pixels at the same location the previous layer, x, reports pore pixels, we say an individual pore has completely been detected.

6. After detection of each pore, the location of the corresponding pixels is saved and then the pixels are nullified (changed to bone tissue) to avoid over-counting. In the case that the pore pixels corresponding to a label on layer x are associated with two or more pore labels on layer $x + 1$, only one of the multiple cross sections (on layer $x + 1$) is chosen as part of the initial object. The others are counted as parts of other objects in later iterations of the algorithm.

7. Repeat the previous steps for all j pores until all the pore pixels are changed to bone.

8. We have now detected every object in the sample and labeled them as individual pores or branches

Once this procedure is complete, we can determine the number of pores as well as the size of each pore in the 3D sample. To begin, we assume pores have either a spherical or cylindrical shape. This assumption simplifies the calculations to obtain the effective radii and can be justified by semi-cylindrical shape of the pores in cortical bone. We categorize the pores in our sample as either based on their aspect ratio, i.e., the ratio of the length of the pore (transverse direction) to the maximum radii of the cross sections. Any pore with an aspect ratio of 3 or larger is assumed to be cylindrical. All others are assumed to be spherical. Thus, based on the assumed shape of an individual object and the volume (sum of pixels in object), the radius of the object is determined as:

$$
\begin{aligned}
r_{sph} &= (1/2) \times \left(\frac{6 V_{sph}}{\pi} \right)^{1/3} \\
r_{cyl} &= (1/2) \times \left(\frac{4 V_{cyl}}{h \pi} \right)^{1/2}.
\end{aligned}
$$

Here, V_{sph}, V_{cyl} are volume of the spherical pores and cylindrical pores respectively. The maximum length of the cylindrical pores is given by h. With the set of the radii measurements, one can use a Kernel Density Estimate (KDE) to approximate the true distribution on pore size in a given sample.

4.6 Computational Results

In this section we provide the computational results of solving the inverse problems laid out in Section 4.4. We begin in Section 4.6.1 with a numerical illustration that provides a proof-of-concept of our inverse problem formulation. There, we generate synthetic, noisy data using the WT forward model with an input Beta distribution for the pore radius. We then solve the inverse problem with both the ISA and WT models to verify we can reconstruct the analytical Beta density function. We use the regularization approach to stabilize the inverse problem. Additionally, we compare the resulting reconstructions across various approximation dimensions, i.e. values of n in (4.9). In Section 4.6.2 inverse problems are solved using the experimental

data, producing estimates of the underlying PDF on pore radius in the human cortical bone samples. These estimates are constructed nonparametrically and their accuracy is determined by comparison with the "true" density functions determined according to Section 4.5.2. We also illustrate the effects various choices of regularization have on the reconstructed PDFs.

4.6.1 Proof-of-Concept Illustrations

To provide a proof-of-concept, we aim to reconstruct the PDF in the simplified case where data is simulated using the WT model and the pore radius is assumed to be distributed according to a Beta distribution. We then use both the ISA and WT models to solve the inverse problem laid out in Section 4.4 and compare the estimated PDFs to the analytical PDF.

To begin, we simulate data using the WT model with an input PDF given by a Beta density function given in (4.5). We then produce simulated data using the model

$$y_j = \bar{\alpha}_{wt}(\omega_j; \alpha_a, f_{\text{Beta}}(p, q, r)) + \varepsilon_j, \quad j = 1, \dots, N,$$

where ε_j's are realizations of iid $\mathcal{N}(0, s^2)$ random variables. This Beta distribution was chosen as it mimics an observed distribution on pore radius based on CT images from cadaver samples. With this data, we solve the inverse problem to reconstruct $f_{\text{Beta}}(r)$ using the PMF as described earlier. Here, we choose shape parameters $p = 2$ and $q = 4$. The noise level is chosen to be $s = 4$. This corresponds to a percentage noise level of 7% the average attenuation value. Representative results are given in Figure 4.7 for $n = 21$ splines and $n_s = 150$ pores/mm^3. Here, we use regularization of the form (4.14) with parameters, $\gamma_{l^2} = 1$ and $\gamma_{h^1} = 0.05$, which were chosen based on numerical experimentations.
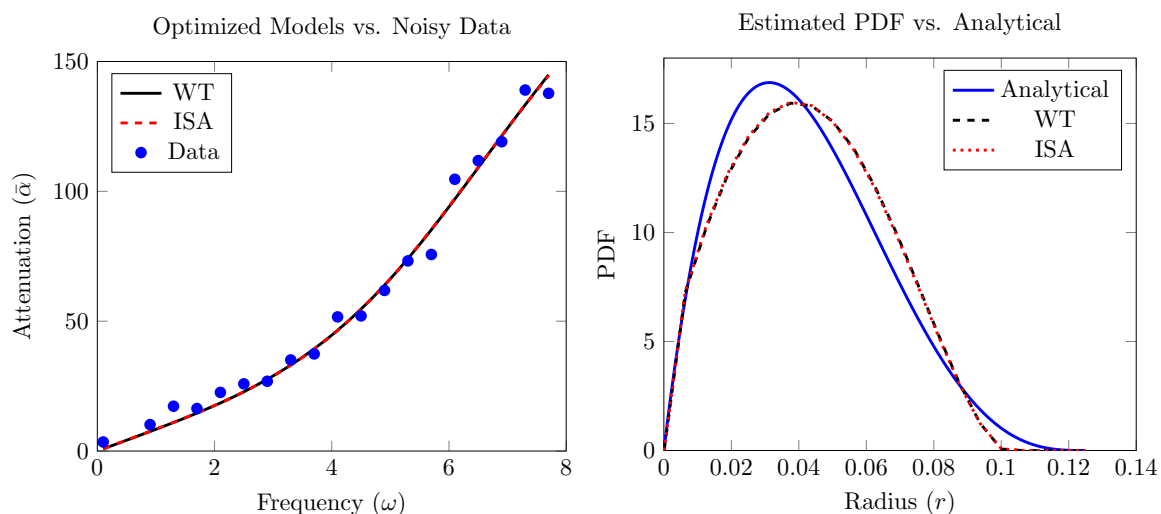

Figure 4.7 Left: ISA and WT model solutions versus simulated data. Right: The estimated ISA and WT PDFs versus the analytical beta density function

Figure 4.7 shows that resulting estimated PDFs for the ISA and WT models are nearly identical and consistent with the "true" input PDF. This indicates that we can reconstruct an input PDF from noisy simulated data using the proposed framework. Furthermore, we estimated $\hat{\alpha}_{a,\text{ISA}} = 9.19$ dB/(cm MHz) and $\hat{\alpha}_{a,\text{WT}} = 9.15$ dB/(cm MHz), which are close to the true value of $\alpha_a = 9.99$ dB/(cm MHz) used in generating the data.

Additionally, we examine if this approach can differentiate between varying levels of bone degradation. To do so, we simulate data using the higher order WT attenuation model with input PDFs given by Beta density functions. We consider two input Beta density functions. One has shape parameters $p = 2$ and $q = 5$ and results in an expected value of pore radius as 0.2857. The other has shape parameters $p = 5$ and $q = 3$ and results in a higher expected value of 0.6250. These two cases allow us to represent varying levels of bone degradation. Figure 4.8 provides the results of solving the inverse problem using $n = 27$ spline bases functions and a regularization term to stabilize the reconstructions. We see from this figure that using the polydisperse ISA model we are able to reconstruct the analytical input density functions using piecewise linear splines. Furthermore, we do so for varying pore radius distributions.
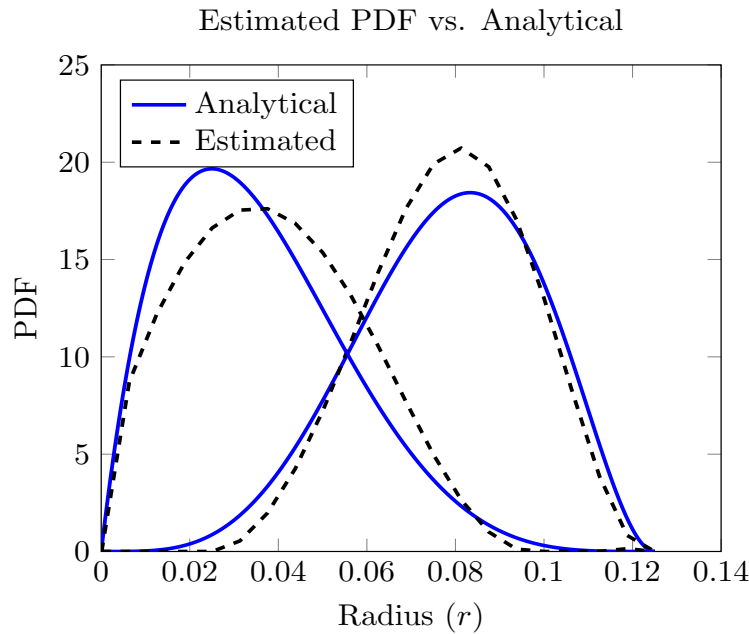
Figure 4.8 The ISA estimated PDFs vs. the analytical Beta PDFs for cases of low and high bone degradation

Overall, the results depicted in Figures 4.7 an 4.8 provide proof-of-concept for the inverse problem formulation where we aim to non-parametrically estimate an underlying PDF as well as scalar absorption coefficient from attenuation data.

We also investigate the impact of the approximation dimension n in (4.9) on the reconstruction.

In theory, increasing n provides more accurate estimates (see Section 4.4.1). However, one must take into account the increase in computational costs as well as numerical errors incurred in doing so. Therefore, we wish to empirically determine an appropriate value for n, such that further increases in the dimension provide negligible improvements in the reconstructions. The grid refinement study in Figure 4.9 provides representative results of the estimated PDF for various values of n. We see that increasing n beyond 20 has a negligible impact on the estimated PDF.
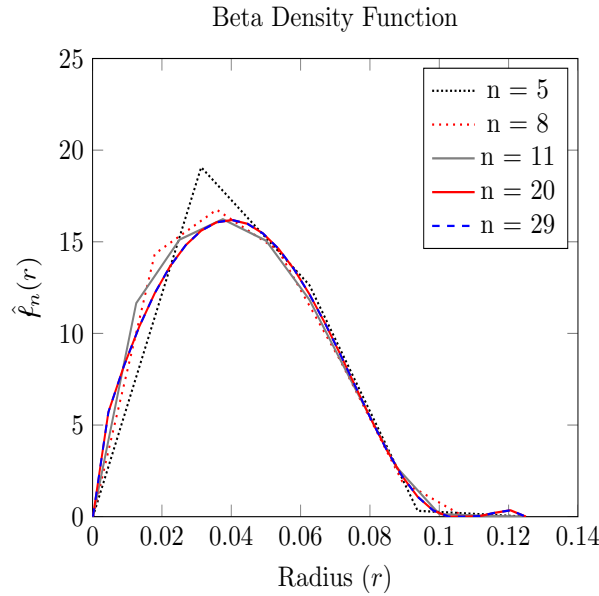
Figure 4.9 Comparison of the resulting PDF estimate ($\hat{f}_n$) for different values of n

4.6.2 Solving the Inverse Problem Using Experimental Data

In this section, we use experimental attenuation data, described in Section 4.5 to solve the inverse problem laid out in Section 4.4. To provide a means of assessing the reliability of estimated PDFs on pore radius, we approximate the nominal underlying PDF by calculating the Kernel Density Estimate (KDE) of the radii data gathered using the CT scans and the algorithm laid out in Section 4.5.2. The KDE is constructed using an empirical sample of pore radii with approximately 6,000 realizations per bone sample. Additionally, the CT scans are used to obtain a nominal value for the pore density, n_s, for each dataset. We have an average pore density of 156 pores/mm^3, where the variance is ($\sigma = 33$ pores/mm^3). As previously mentioned, the pore density will be fixed when solving the inverse problem. Here, we fix pore density to the nominal value determined by the CT scans. In general, one would not have a nominal pore density and would need to fix this parameter at an acceptable value, often determined from literature or experimentation.

We first consider the effects of various regularizations on the reconstructed PDFs. To do so, we compare the approximated PDFs to the KDEs for various regularization parameter values $(\gamma_{l_2}, \gamma_{h_1})$. Representative results using Dataset 2 are depicted in Figure 4.11. Here, we consider: no regularization, L^2 regularization, and a combination of L^2 and H^1 regularizations. Note that the specific regularization parameter values are chosen empirically through trial and error. In these results, we used $n = 27$ linear splines for approximating the PDFs (see (4.9)); this was observed to provide a good balance between quality of the estimated PDFs and the computational cost of solving the inverse problem.
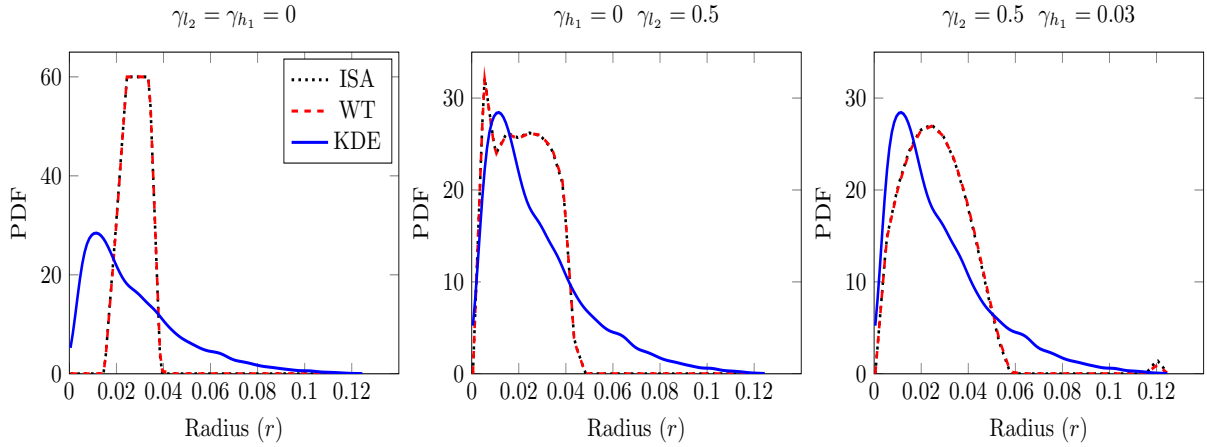
Figure 4.10 Comparison of reconstructed PDF for various regularization parameters for Dataset 2

We notice from Figure 4.10 (left) that without any regularization, the reconstructed PDFs do not accurately capture the shape of the "true" density function. However, from the middle graph, we see that using an L^2 regularization improves this reconstruction. Ultimately, we see that incorporating an H^1 regularization (right) results in much better reconstructions in this case. Specifically, we see that using a combination of L^2 and H^1 terms provides a reconstruction that is clearly superior to ones obtained by using no regularization or L^2 regularization only. In our numerical experiments, we find that using the H^1 regularization alone provided sufficiently accurate reconstructions (see below). To provide a full picture, we used only an H^1 regularization on all eight datasets; see Figure 4.11.
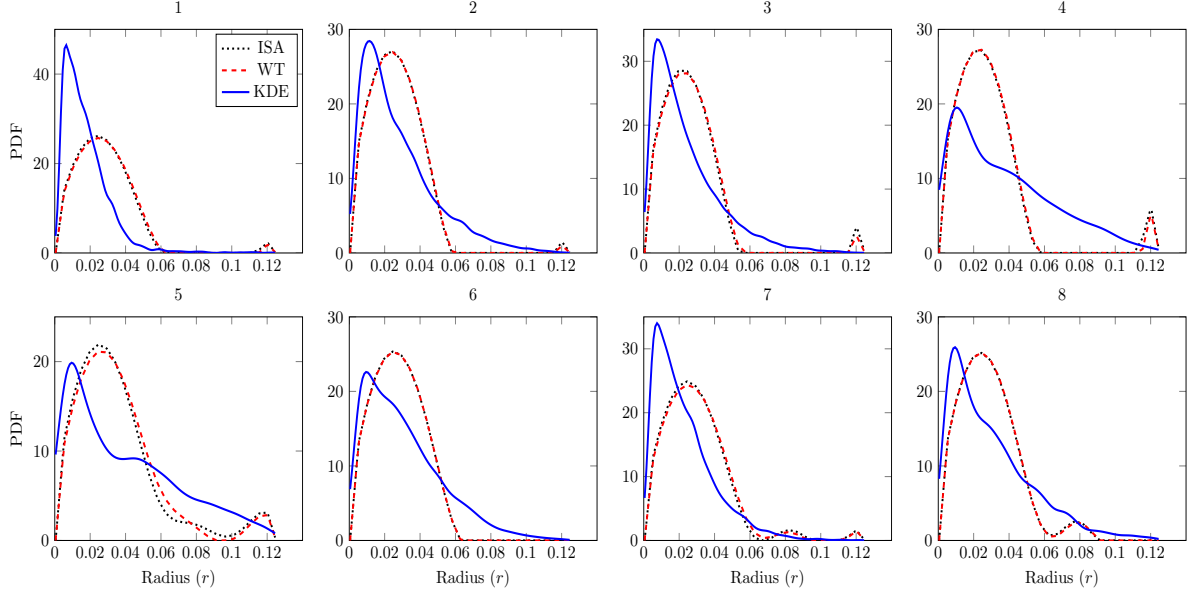
Figure 4.11 Comparison of $\hat{f}_n(r)$ versus the KDE using both the ISA and WT models across eight datasets for: $\gamma_{l^2} = 0$, $\gamma_{h^1} = 0.03$, $n = 27$

We see by comparing the Dataset 2 graph in Figure 4.11 to the far right graph in Figure 4.10, the combination L^2 and H^1 regularization provides negligible improvement over only an H^1 penalty. Overall, we find that it is necessary to have an H^1 penalty to have a smooth approximation to the KDE. It should be noted, that in solving this inverse problem, we do not seek an exact reconstruction of the KDEs. Specifically, these KDEs only provide a rough approximation to the true PDF due to errors in the CT scans, and from assumptions made in the algorithm that processes the CT scans. With this in mind, the nonparametric estimates, $\hat{f}_n$, given in 4.11 are considered to infer the true microstructure of the bone samples well.

Next, using the PDF reconstruction corresponding to dataset 2 and obtained via the H^1 regularization, we examine the model fit and also compare the estimated cumulative distribution function (CDF) with the corresponding "true" CDF. The estimated CDF is obtained by integrating the estimated PDF. Figure 4.12 provides the model (both ISA and WT) fit to the experimental data as well as the estimated PDFs and CDFs.
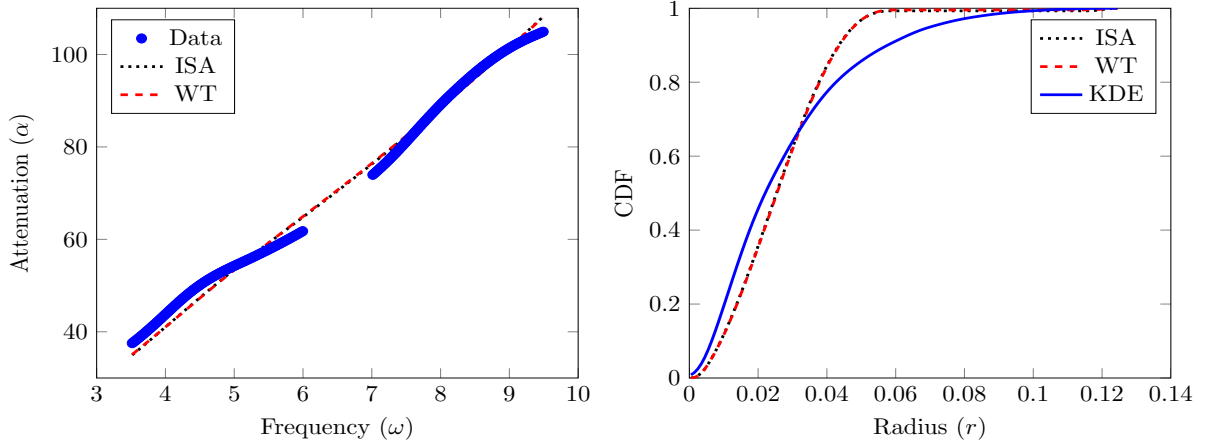
Figure 4.12 Left: model predictions versus experimental data; right: CDF versus KDE (we used $\gamma_{l^2} = 0$, $\gamma_{h^1} = 0.03$, $n = 27$). The CDF estimate corresponds to the PDF estimate 2 in top row of Figure 4.11

From Figure 4.12 (left) we note that we do not have experimental data in the frequency range 6–7 Mhz due to the bandwidth of the transducers. However, the attenuation data aligns well at the endpoints of these frequency ranges. Despite this, we see that both the ISA and WT model solutions fit the attenuation data well and closely match one another. We are able to nonparametrically estimate $f(r)$, capturing both the mean of the function ($\bar{r}_{\text{isa}} = \bar{r}_{\text{wt}} = 0.026$ mm and $\bar{r}_{\text{dat}} = 0.028$ mm) as well as the overall shape. Similarly, we see accurate predictions of the underlying CDF for both the ISA and WT. The negligible difference between results obtained using the two models indicates the higher order terms of the WT model do not increase the accuracy of the reconstructions. Also, in estimating the absorption coefficient, we see both models provide similar estimates ($\hat{\alpha}_{a,\text{ISA}} = 9.27$ dB/(cm MHz) and $\hat{\alpha}_{a,\text{WT}} = 9.37$ dB/(cm MHz)). However, the nominal value of this parameter from experimentation is not known, and therefore we cannot compare the models' accuracy in determining this.

4.7 Conclusions

In this work we discussed several ways of formulating polydisperse attenuation models using probabilistic approximations. We then introduced polydisperse formulations of the previously established Independent Scattering Approximation (ISA) and the Waterman Truell (WT) models and compared their forward model predictions with an input analytical Beta density function. We then formulated an inverse problem and approximation scheme using the Prohorov Metric Framework (PMF) and introduced regularization functions to address the ill-posed nature of the inverse problem. We then provided illustrative results by solving the inverse problem using simulated noisy data and reconstructed the input Beta density function using the piecewise linear spline approximation scheme. Following this, we performed experiments to measure the

attenuation *in-vitro* from human cadaver cortical bone samples. We used micro CT to determine the baseline "true" microstructure of the samples in the form of a Kernel Density Estimate. We then solved the inverse problem using the experimental data and compared the reconstructed probability density functions (PDFs) to the KDE.

We were able to obtain close estimates of the underlying PDF on pore radius from the attenuation data in all eight cortical bone samples considered. We found that an H^1 regularization function was required to stabilize the inverse problem and provide accurate estimates. We also found little variation between the ISA and WT models' forward predictions and estimated PDFs. This indicates that the higher order terms of the WT model are not necessary for predicting information regarding the underlying microstructure of cortical bone in our specific application.

In future work, we will adapt the proposed methodology to backscattering attenuation models to predict microstructures *in-vivo*. Doing so could enable diagnosing osteoporosis in human patients using non-invasive, non-ionizing ultrasound interrogation.

Aknowledgements

CHAPTER

5

CONCLUSIONS

This dissertation provides a quantitative tool for characterizing the microstructure of cortical bone using ultrasound attenuation data. To characterize bone diseases, one must be able to infer the microstructure of the cortical bone. Many current approaches are invasive, ionizing, or generally infeasible for the routine screening of patients. Because of this, an approach that utilized ultrasound interrogation to determine the size and density of pores within the cortical bone was desired. To provide a quantitative tool, we took an inverse problems approach, which uses data along with mathematical models to estimate the microstructural parameters.

In Chapter 2, we began by establishing that ultrasound attenuation is dependent upon the microstructural parameters, pore size and density. This was done using 2D monodisperse, cortical bone-like structures. Simulating attenuation data and physically modeling attenuation using the phenomenological, power-law model allowed us to formulate and solve an Ordinary Least Squares (OLS) inverse problem. Analyzing the resulting parameter estimates' standard errors showed we could estimate the model parameters with a high degree of confidence. We then determined, using linear regression, invertible relationships between these model parameter estimates and the microstructural parameters. Ultimately, this methodology provided a low resolution approach to characterize porosity of the 2D monodisperse samples from ultrasound data. This provided proof-of-concept for inferring microstructural information using ultrasound waves.

We built on this work in Chapter 3. There we used two physics-based models for wave attenuation, the Independent Scattering Approximation (ISA) and the Waterman Truell (WT) model, as these explicitly model the dependence of wave attenuation on pore size and density. We also considered more realistic 3D monodisperse structures, which were used to numerically generate data. We again used the models and data to solve an OLS inverse problem. Doing

so showed that we could estimate the pore size and density in the 3D monodisperse samples, providing a higher resolution approach to characterize microstructure than in Chapter 2 work. The major contribution of the work in Chapter 3 was establishing both the ISA and WT models for not only predicting wave attenuation in cortical bone, but also for the purpose of inferring microstructure. Doing so provides the foundation for considering more realistic problem formulations.

The final phase of the work in this dissertation was detailed in Chapter 4 where we considered polydisperse samples in which the pores varied in size. Thus, the pore size had an inherent statistical distribution with an associated PDF. Characterizing microstructure in terms of the PDF on pore size provides more diagnostic information than the average pore size estimates of previous work. To solve this more realistic problem, we reformulated the two models (ISA and WT) from Chapter 3 to represent the polydisperse structures. We used the Prohorov Metric Framework to make this infinite-dimensional inverse problem tractable and implemented variational regularization functions to stabilize the inverse problem. There, we gathered experimental attenuation data using bone samples taken from human cadavers. MicroCT imaging allowed us to establish a baseline or "true" PDF on pore size within the samples. In solving the inverse problem, we showed that we are able to accurately reconstruct the nominal PDF on pore size. Thus, the approach taken in Chapter 4 provided a high resolution approach for inferring the microstructure of real human cortical bone samples, solely from attenuation data. Overall, the methodology given in this dissertation provides a quantitative tool for characterizing *in-vitro* cortical bone microstructure using non-invasive, non-ionizing ultrasound.

In future work, we aim to apply the methodology laid out in this dissertation to the scenario where data is taken in-vivo, which would be the case when characterizing the microstructure of the cortical bone in a living patient. To do so, one would need a mathematical model for attenuation that took into account backscattering as well as the layered tissues that the wave must pass through prior to the cortical bone. Another point of difference would be the aggregate nature of the experimental data in the *in-vivo* setting [15]. In the current work, we focus on cubic cortical bone sections, for which emitting and receiving transducers cover the entire area of the incident faces of the cube. Thus, we account for the entire geometry of the bone sample. When considering this experiment on a live patient, one would not be able to fully characterize the entire geometry of the cortical bone. Rather one would have multiple realizations of that geometry dependent on where, physically, the ultrasonic pulse was emitted relative to the patient. Because of this, the aggregate nature of the attenuation data would need to be accounted for when solving the inverse problem.

Other areas of future work involve improving the methodology in the last phase of this work (Chapter 4). Investigating the effects of various boundary conditions on the PDF could be of interest. Also, using the techniques in [4] to more accurately specify the form of the error in the data observations could be investigated in the future. Furthermore, using more rigorous ways of determining the optimal regularization function tuning parameter, such as L-curve [107] is

another area of future work to better fine tune the result.

BIBLIOGRAPHY

[1] Andreasen, C. M., Bakalova, L. P., Brüel, A., Hauge, E. M., Kiil, B. J., Delaisse, J.-M., Kersh, M. E., Thomsen, J. S. & Andersen, T. L. "The generation of enlarged eroded pores upon existing intracortical canals is a major contributor to endocortical trabecularization." *Bone* **130** (2020), p. 115127.

[2] Augat, P., Reeb, H. & Claes, L. "Prediction of fracture load at different skeletal sites by geometric properties of the cortical shell." *Journal of bone and mineral research : the official journal of the American Society for Bone and Mineral Research* **11** (2009), pp. 1356–63.

[3] Bala, Y., Zebaze, R., Ghasem-Zadeh, A., Atkinson, E., Iuliano, S., Peterson, J., Amin, S., Melton, L., Johansson, H., Kanis, J., Khosla, S. & Seeman, E. "Cortical porosity identifies women with osteopenia at increased risk for forearm fractures." *Journal of bone and mineral research : the official journal of the American Society for Bone and Mineral Research* **29**.6 (2014), pp. 1356–62.

[4] Banks, H., Catenacci, J. & Hu, S. "Use of difference-based methods to explore statistical and mathematical model discrepancy in inverse problems." *Journal of Inverse and Ill-posed Problems* **24** (2016).

[5] Banks, H. T. *A functional analysis framework for modeling, estimation and control in science and engineering*. CRC Press, 2012.

[6] Banks, H. T., Banks, J., Cody, N., Hoddle, M. & Meade, A. "Population model for the decline of Homalodisca vitripennis (Hemiptera: Cicadellidae) over a ten-year period." *Journal of Biological Dynamics* **13** (2019), pp. 422–446.

[7] Banks, H. T. & Bortz, D. "Inverse problems for a class of measure dependent dynamical systems." *Journal of Inverse and Ill-Posed Problems* **13** (2005), pp. 103–121.

[8] Banks, H. T., Catenacci, J. & Criner, A. "Quantifying the degradation in thermally treated ceramic matrix composites." *International Journal of Applied Electromagnetics and Mechanics* **52** (2016), pp. 1–22.

[9] Banks, H. T. & Davis, J. L. "A comparison of approximation methods for the estimation of probability distributions on parameters." *Applied Numerical Mathematics* **57**.5 (2007). Special Issue for the International Conference on Scientific Computing, pp. 753 –777.

[10] Banks, H. T., Flores, K., Rosen, I., Rutter, E., Sirlanci, M. & Thompson, W. C. "The prohorov metric framework and aggregate data inverse problems for random PDEs." *Communications in Applied Analysis* **22** (2018).

[11] Banks, H. T. & Gibson, N. L. "Electromagnetic inverse problems involving distributions of dielectric mechanisms and parameters." *Quarterly of Applied Mathematics* **64** (2006).

[12] Banks, H. T., Hu, S. & Thompson, W. C. *Modeling and inverse problems in the presence of uncertainty*. CRC Press, Taylor and Francis, 2014.

[13] Banks, H. T., Kenz, Z. & Thompson, W. "A review of selected techniques in inverse problem nonparametric probability distribution estimation." *Journal of Inverse and Ill-Posed Problems* **20** (2012).

[14] Banks, H. T. & Pinter, G. "A probabilistic multiscale approach to hysteresis in shear wave propagation in biotissue." *Multiscale Modeling & Simulation* **3** (2004), p. 21.

[15] Banks, H. T. & Tran, H. T. *Mathematical and experimental modeling of physical and biological processes*. CRC Press, 2009.

[16] Beltzer, A. & Brauner, N. "Wave propagation in random participate composites: a modification of the Foldy-Lax theory." *Acta Acustica united with Acustica* **65** (1988), pp. 156–162.

[17] Beltzer, A. I. "The effective dynamic response of random composites and polycrystals—a survey of the causal approach." *Wave Motion* **11**.3 (1989), pp. 211 –229.

[18] Bennamane, A. & Boutkedjirt, T. "Theoretical and experimental study of the ultrasonic attenuation in bovine cancellous bone." *Applied Acoustics* **115** (2017), pp. 50–60.

[19] Billingsley, P. *Convergence of probability measures*. Wiley & Sons, New York, 1968.

[20] Biwa, S. "Independent scattering and wave attenuation in viscoelastic composites." *Mechanics of Materials* **33**.11 (2001), pp. 635 –647.

[21] Bjørnerem, Wang, X., Bui, M., Ghasem-Zadeh, A., Hopper, J. L., Zebaze, R. & Seeman, E. "Menopause-related appendicular bone loss is mainly cortical and results in increased cortical porosity." *Journal of Bone and Mineral Research* **33**.4 (2018), pp. 598–605.

[22] Bochud, N., Vallet, Q., Bala, Y., Follet, H., Minonzio, J.-G. & Laugier, P. "Genetic algorithms-based inversion of multimode guided waves for cortical bone characterization." *Physics in Medicine and Biology* **61**.19 (2016), pp. 6953–6974.

[23] Bosisio, M., Talmant, M., Skalli, W., Laugier, P. & Mitton, D. "Apparent Young's modulus of human radius using inverse finite-element method." *Journal of Biomechanics* **40**.9 (2007), pp. 2022–2028.

[24] Bossy, E. "SimSonic suite user's guide for SimSonic2D." (2012).

[25] Bossy, E., Padilla, F., Peyrin, F. & P., L. "Three-dimensional simulation of ultrasound propagation through trabecular bone structures measured by synchrotron microtomography." *Physics in Medicine and Biology* **23**.50 (2005), pp. 5545–5556.

[26] Bossy, E., Talmant, M. & Laugier, P. "Three-dimensional simulations of ultrasonic axial transmission velocity measurement on cortical bone models." *The Journal of the Acoustical Society of America* **115**.5 (2004), pp. 2314–2324.

[27] Bousson, V., Meunier, A., Bergot, C., Vicaut, É., Rocha, M. A., Morais, M. H., Laval-Jeantet, A. & Laredo, J. "Distribution of intracortical porosity in human midfemoral cortex by age and gender." *Journal of Bone and Mineral Research* **16**.7 (2001), pp. 1308–1317.

[28] Boutroy, S., Bouxsein, M. L., Munoz, F. & Delmas, P. D. "In vivo assessment of trabecular bone microarchitecture by high-resolution peripheral quantitative computed tomography." *Journal of Clinical Endocrinology and Metabolism* **90**.12 (2005), pp. 6508–6515.

[29] Braithwaite, R. S., Col, N. F. & Wong, J. B. "Estimating hip fracture morbidity, mortality and costs." *Journal of the American Geriatrics Society* **51**.3 (2003), pp. 364–370.

[30] Brajanovski, M., Gurevich, B. & Schoenberg, M. "A model for P-wave attenuation and dispersion in a porous medium permeated by aligned fractures." *Geophysical Journal International* **1**.163 (2005).

[31] Brunet, T., Merlin A.and Mascaro, B., Zimny, K., Leng, J., Poncelet, O., Aristégui, C. & Mondain-Monval, O. "Soft 3D acoustic metamaterial with negative index." *Nature Materials* **14**.4 (2015), pp. 384–388.

[32] Brunet, T., Zimny, K., Mascaro, B., Sandre, O., Poncelet, O., Aristégui, C. & Mondain-Monval, O. "Tuning Mie scattering resonances in soft materials with magnetic fields." *Physical Revew Letters* **111** (26 2013), p. 264301.

[33] Butler T.and Wildey, T. & Yen, T. Y. "Data-consistent inversion for stochastic input-to-output maps". *Inverse Problems* **36**.8 (2020).

[34] Cassereau, D., Nauleau, P., Grimal, Q., Minonzio, J., Bendjoudi, A., Bossy, E. & Laugier, P. "Coupling of finite difference elastodynamic and semi-analytic Rayleigh integral codes for the modeling of ultrasound propagation at the hip." *The Journal of the Acoustical Society of America* **5**.133 (2013), pp. 3498–3498.

[35] Catenacci, J. "Quantifying degradation in ceramic matrix composites through electromagnetic interrogation and the related estimation techniques." PhD thesis. 2016.

[36] Chaffaî, S., Peyrin, F., Nuzzo, S., Porcher, R., Berger, G. & Laugier, P. "Ultrasonic characterization of human cancellous bone using transmission and backscatter measurements: relationships to density and microstructure." *Bone* **30**.1 (2002), pp. 229–37.

[37] Chekroun, M., Le Marrec, L., Lombard, B. & Piraux, J. "Time-domain numerical simulations of multiple scattering to extract elastic effective wavenumbers." *Waves in Random and Complex Media* **22**.3 (2012), pp. 398–422.

[38] Chen, H., Zhou X.and Fujita, H., Onozuka, M. & Kubo, K. "Age-related changes in trabecular and cortical bone microstructure." *International Journal of Endocrinology* **2013** (2013), pp. 1–9.

[39] Choudhuri, N., Ghosal, S. & Roy, A. "Bayesian methods for function estimation." *Handbook of Statistics* **25** (2005), pp. 373–414.

[40] Clarke, B. "Normal bone anatomy and physiology." *Clinical journal of the American Society of Nephrology : CJASN* **3 Suppl 3** (2008), S131–9.

[41] Delmas, P. D. "The treatment of postmenopausal osteoporosis." *Prevention and treatment of Osteoporosis in the high-risk patient: A clinician's guide, ch. 5.* Ed. by Cooper, C. & Gehlback, S. Taylor & Francis, 2005, pp. 58–82.

[42] Derode A.and Mamou, V. & Tourin, A. "Influence of correlations between scatterers on the attenuation of the coherent wave in a random medium." *Physics Review E* **74** (3 2006), p. 036606.

[43] Du, H., Mohanty, K. & Muller, M. "Microstructural characterization of trabecular bone using ultrasonic backscattering and diffusion parameters." *The Journal of the Acoustical Society of America* **141**.5 (2017), EL445–EL451.

[44] Duitama Leal, A., Almanza, O. & Montes Vides, L. A. "Modeling attenuation and dispersion of acoustic waves in porous media containing immiscible non viscous fluids." *DYNA* **83**.199 (2016), p. 78.

[45] Egan, T. M., Mohanty, K., Ali, M., Blackwell, J., Ulrich, M. & Muller, M. "Novel uses of ultrasound in various lung diseases." *The Journal of the Acoustical Society of America* **148**.4 (2020), pp. 2690–2690.

[46] Eneh, C. T. M., Afara, I. O., Malo, M. K. H., Jurvelin, J. S. & Töyräs, J. "Porosity predicted from ultrasound backscatter using multivariate analysis can improve accuracy of cortical bone thickness assessment." *The Journal of the Acoustical Society of America* **141**.1 (2017), pp. 575–585.

[47] Evans, F. G. & Bang, S. "Differences and relationships between the physical properties and the microscopic structure of human femoral, tibial and fibular cortical bone." *American Journal of Anatomy* **120**.1 (1967), pp. 79–88.

[48] Evans, J. A. & Tavakoli, M. B. "Ultrasonic attenuation and velocity in bone." *Physics in Medicine and Biology* **35**.10 (1990), pp. 1387–1396.

[49] Foiret, J., Minonzio, J., Chappard, C., Talmant, M. & Laugier, P. "Combined estimation of thickness and velocities using ultrasound guided waves: a pioneering study on in vitro cortical bone samples." *IEEE Transactions on Ultrasonics, Ferroelectrics, and Frequency Control* **61**.9 (2014), pp. 1478–1488.

[50] Foldy, L. L. "The multiple scattering of waves. I. general theory of isotropic scattering by randomly distributed scatterers." *Physics Review* **67** (3-4 1945), pp. 107–119.

[51] Garnier, V., Payan, C., Martin, L., Ranaivomanana, N., Balayssac, J., Verdier, J., Larose, E., Zhang, Y., Saliba, J., Boniface, A., Sbartaï, Z. M., Piwakowski, B., Ciccarone, C., Hafid, H., Jean-Marie, H. & Ouvrier-Buffet, F. "Non-destructive evaluation of containment walls in nuclear power plants." Vol. 1806. 2017, p. 080018.

[52] Gluer, C. C. "A new quality of bone ultrasound research." *IEEE transactions on ultrasonics, ferroelectrics, and frequency control* **55**.7 (2008), 1524—1528.

[53] Grimal, Q. & Laugier, P. "Quantitative ultrasound assessment of cortical bone properties beyond bone mineral density." *Innovation and Research in BioMedical engineering* **40**.1 (2019), pp. 16–24.

[54] Guo, S., Dai, Q., Sun, X. & Sun, Y. "Ultrasonic scattering measurement of air void size distribution in hardened concrete samples." *Construction and Building Materials* **113** (2016), pp. 415 –422.

[55] Haïat, G. & Naili, S. "Independent scattering model and velocity dispersion in trabecular bone: comparison with a multiple scattering model." *Biomech Model Mechanobiol* **10** (2010), pp. 95–108.

[56] Hoc, T., Henry, L., Verdier, M., Aubry, D., Sedel, L. & Meunier, A. "Effect of microstructure on the mechanical properties of Haversian cortical bone." *Bone* **38**.4 (2006), pp. 466 –474.

[57] Iori, G., Schneider, J., Reisinger, A., Heyer, F., Peralta, L., Wyers, C., Gräsel, M., Barkmann, R., Glüer, C. C., Bergh, J. P. van den, Pahr, D. & Raum, K. "Large cortical bone pores in the tibia are associated with proximal femur strength." *PLOS ONE* **14**.4 (2019), pp. 1–18.

[58] Ishimaru, A. *Wave propagation and scattering in random media. Volume 1 - Single scattering and transport theory*. Vol. 1. 1978, pp. 36 –37.

[59] Jackson, J. D. *Classical electrodynamics (3rd ed.)* John Wiley & Sons, 1999, pp. 500–510.

[60] Johnell, O. & Kanis, J. A. "An estimate of the worldwide prevalence and disability associated with osteoporotic fractures." *Osteoporosis International* **17**.12 (2006), pp. 1726–1733.

[61] Karjalainen, J. P., Töyräs, J., Riekkinen, O., Hakulinen, M. & Jurvelin, J. S. "Ultrasound backscatter imaging provides frequency-dependent information on structure, composition and mechanical properties of human trabecular Bone." *Ultrasound in Medicine & Biology* **35**.8 (2009), pp. 1376–1384.

[62] Krug, R., Burghardt, A. J., Majumdar, S. & Link, T. M. "High-resolution imaging techniques for the assessment of osteoporosis." *Radiologic clinics of North America* **48**.3 (2010), pp. 601–21.

[63] Laugier, P. "Instrumentation for in vivo ultrasonic characterization of bone strength." *IEEE Transactions on Ultrasonics, Ferroelectrics and Frequency Control* **55** (2008).

[64] Lax, M. "Multiple Scattering of Waves. II. The Effective Field in Dense Systems". *Physical Review* **85** (1952), pp. 621–629.

[65] Mandarano-Filho, L. G., Bezuti, M. T., Mazzer, N. & Barbieri, C. H. "Influence of cortical bone thickness on the ultrasound velocity." *Acta ortopedica brasileira* **20**.3 (2012), pp. 184–90.

[66] Marshall, D., Johnell, O. & Wedel, H. "Meta-analysis of how well measures of bone mineral density predict occurrence of osteoporotic fractures." *British Medical Journal* **312**.7041 (1996), pp. 1254–1259.

[67] MATLAB. Natick, Massachusetts: The MathWorks Inc., 2016.

[68] McCalden, R. W., McGeough, J. A., Barker, M. B. & Court-Brown, C. M. "Age-related changes in the tensile properties of cortical bone. The relative importance of changes in porosity, mineralization, and microstructure." *The Journal of bone and joint surgery. American volume* **75**.8 (1993), pp. 1193–205.

[69] Melton, L. J., Atkinson, E. J., O 'connor, M. K., O 'fallon, W. M. & Riggs, B. L. "Bone density and fracture risk in men." *Journal of Bone Mineral Research* **13**.12 (1998), pp. 1915–1923.

[70] Melton, L. J., Chrischilles, E. A., Cooper, C., Lane, A. W. & Riggs, B. L. "Perspective. how many women have osteoporosis?" *Journal of Bone and Mineral Research* **7**.9 (1992), pp. 1005–1010.

[71] Meulen, F., Feuillard, G., Bou Matar, O., Levassort, F. & Lethiecq, M. "Theoretical and experimental study of the influence of the particle size distribution on acoustic wave properties of strongly inhomogeneous media." *The Journal of the Acoustical Society of America* **110** (2001), pp. 2301–7.

[72] Mézière, F., Muller, M., Bossy, E. & Derode, A. "Modeling ultrasound interaction with cancellous bone: investigation on the nature of the two compressional waves." *The Journal of the Acoustical Society of America* **131**.4 (2012), pp. 3460–3460.

[73] Mézière, F., Muller, M., Bossy, E. & Derode, A. "Measurements of ultrasound velocity and attenuation in numerical anisotropic porous media compared to Biot's and multiple scattering models." *Ultrasonics* **54**.5 (2014), pp. 1146–1154.

[74] Méziére, F., Muller, M., Bossy, E. & Derode, A. "Measurements of ultrasound velocity and attenuation in numerical anisotropic porous media compared to Biot's and multiple scattering models." *Ultrasonics* **54**.5 (2014), pp. 1146–1154.

[75] Mohanty, K., Yousefian, O., Karbalaeisadegh, Y., Ulrich, M., Grimal, Q. & Muller, M. "Artificial neural network to estimate micro-architectural properties of cortical bone using ultrasonic attenuation: A 2-D numerical study." *Computers in Biology and Medicine* (2019), p. 103457.

[76] Moilanen, P., Nicholson, P. H. F., Kilappa, V., Cheng, S. & Timonen, J. "Assessment of the cortical bone thickness using ultrasonic guided waves: Modelling and in vitro study." *Ultrasound in Medicine & Biology* **33**.2 (2007), pp. 254–262.

[77] Moreau, L., Lachaud, C., Théry, R., Predoi, M. V., Marsan, D., Larose, E., Weiss, J. & Montagnat, M. "Monitoring ice thickness and elastic properties from the measurement of leaky guided waves: A laboratory experiment." *The Journal of the Acoustical Society of America* **142**.5 (2017), pp. 2873–2880.

[78] Muller, M., Dobigny, B., Bossy, E. & Derode, A. "Two-dimensional simulations of ultrasound propagation in random anisotropic media: Application to trabecular bone assessment." *The Journal of the Acoustical Society of America* **129**.4 (2011), p. 2611.

[79] Nguyen Minh, H., Du, J. & Raum, K. "Estimation of thickness and speed of sound in cortical bone using multifocus pulse-echo ultrasound." *IEEE Transactions on Ultrasonics, Ferroelectrics, and Frequency Control* **67**.3 (2020), pp. 568–579.

[80] Nishiyama, K. K., Macdonald, H. M., Buie, H. R., Hanley, D. A. & Boyd, S. K. "Postmenopausal women with Osteopenia have higher cortical porosity and thinner cortices at the distal radius and tibia than women with normal aBMD: An in vivo HR-pQCT study." *Journal of Bone and Mineral Research* **25**.4 (2009).

[81] Osterhoff, G., Morgan, E. F., Shefelbine, S. J., Karim, L., Mcnamara, L. M. & Augat, P. "Bone mechanical properties and changes with osteoporosis." *Injury, International Journal of the Care of the Injured* **47** (2016), S11–S20.

[82] Padilla, F., Bossy, E., Haiat, G., Jenson, F. & Laugier, P. "Numerical simulation of wave propagation in cancellous bone." *Ultrasonics* **44** (2006), e239 –e243.

[83] Padilla, F. & Laugier, P. "Recent developments in trabecular bone characterization using ultrasound." *Current Osteoporosis Reports* **3**.2 (2005), pp. 64–69.

[84] Prokhorov, Y. V. "Convergence of random processes and limit theorems in probability theory." *Theory of Probability & Its Applications* **1**.2 (1956), pp. 157–214.

[85] Punurai, W. "Cement-based materials' characterization using ultrasonic attenuation." PhD thesis. 2006.

[86] Punurai, W., Jarzynski, J., Qu, J., Kurtis, K. E. & Jacobs, L. J. "Characterization of entrained air voids in cement paste with scattered ultrasound." *Nondestructive Testing & Evaluation International* **39**.6 (2006), pp. 514 –524.

[87] Punurai, W., Jarzynski, J., Qu, J., Kurtis, K. E. & Jacobs, L. J. "Characterization of dissipation losses in cement paste with diffuse ultrasound." *Mechanics Research Communications* **34**.3 (2007), pp. 289–294.

[88] Rajapakse, C. S., Bashoor-Zadeh, M., Li, C., Sun, W., Wright, A. C. & Wehrli, F. W. "Volumetric cortical bone porosity assessment with MR imaging: validation and clinical feasibility." *Radiology* **276**.2 (2015), pp. 526–535.

[89] Rose, E. C., Hagenmüller, M., Jonas, I. E. & Rahn, B. A. "Validation of speed of sound for the assessment of cortical bone maturity." *European Journal of Orthodontics* **27**.2 (2005), pp. 190–195.

[90] Sasso, M., Haïat, G., Yamato, Y., Naili, S. & Matsukawa, M. "Frequency dependence of ultrasonic attenuation in bovine cortical bone: An in vitro study." *Ultrasound in Medicine & Biology* **33**.12 (2007), pp. 1933–1942.

[91] Sato, H. & Fehler, M. *Seismic wave propagation and scattering in the heterogeneous earth.* Springer, 1998.

[92] Schaffler, M. B. & Burr, D. B. "Stiffness of compact bone: effects of porosity and density." *Journal of biomechanics* **21**.1 (1988), pp. 13–6.

[93] Schuit, S. C. E., Klift, M. van der, Weel, A. E. A. M., Laet, C. E. D. H. de, Burger, H., Seeman, E., Hofman, A., Uitterlinden, A. G., Leeuwen, J. P. T. M. van & Pols, H. A. P. "Fracture incidence and association with bone mineral density in elderly men and women: the Rotterdam Study." *Bone* **34**.1 (2004), pp. 195–202.

[94] Sheng, P. *Introduction to wave scattering, localization and mesoscopic phenomena.* Springer, 2011.

[95] Sievänen, H., Cheng, S., Ollikainen, S. & Uusi-Rasi, K. "Ultrasound velocity and cortical bone characteristics in vivo." *Osteoporosis international : a journal established as result of cooperation between the European Foundation for Osteoporosis and the National Osteoporosis Foundation of the USA* **12**.5 (2001), pp. 399–405.

[96] Sievänen, H., Cheng, S., Ollikainen, S & Uusi-Rasi, K. "Ultrasound Velocity and Cortical Bone Characteristics In Vivo." *Osteoporosis international : a journal established as result of cooperation between the European Foundation for Osteoporosis and the National Osteoporosis Foundation of the USA* **12** (2001), pp. 399–405.

[97] Smith, R. *Uncertainty quantification: theory, implementation, and applications.* USA: Society for Industrial and Applied Mathematics, 2013.

[98] Sornay-Rendu, E., Munoz, F., Duboeuf, F. & Delmas, P. D. "Rate of forearm bone loss is associated with an increased risk of fracture independently of bone mass in postmenopausal women: The OFELY study." *Journal of Bone and Mineral Research* **20**.11 (2005), pp. 1929–1935.

[99] Strelitzki, R., Evans, J. A. & Clarke, A. J. "The influence of porosity and pore size on the ultrasonic properties of bone investigated using a phantom material." *Osteoporosis International* **7**.4 (1997), pp. 370–375.

[100] Tallon, B., Roux, P., Matte, G., Guillard, J. & Skipetrov, S. "Acoustic density estimation of dense fish shoals." *The Journal of the Acoustical Society of America* **148** (2020).

[101] Tavakoli, M. B. & Evans, J. A. "The effect of bone structure on ultrasonic attenuation and velocity." *Ultrasonics* (1992), pp. 389–395.

[102] Thomas, C., Feik, S. & Clement, J. "Increase in pore area, and not pore density, is the main determinant in the development of porosity in human cortical bone." *Journal of anatomy* **209** (2006), pp. 219–30.

[103] Thomas, C. D., Feik, S. A & Clement, J. G. "Increase in pore area, and not pore density, is the main determinant in the development of porosity in human cortical bone." *Journal of anatomy* **209**.2 (2006), pp. 219–30.

[104] Tourin, A., Derode, A. & Fink, M. "Transport parameters for an ultrasonic pulsed wave propagating in a multiple scattering medium." *1999 IEEE International Ultrasonics Symposium (IUS)*. IEEE, 2000, pp. 711–714.

[105] Virieux, J. "SH wave propagation in heterogeneous media: Velocity-stress finite-difference method." *Geophysics* **49**.11 (1984), pp. 1933–1942.

[106] Virieux, J. "P-SV wave propagation in heterogeneous media: Velocity-stress finite-difference method." *Geophysics* **51**.4 (1986), pp. 889–901.

[107] Vogel, C. R. *Computational Methods for Inverse Problems*. Society for Industrial and Applied Mathematics, 2002.

[108] Wang, Z., Wang, R., Li, T., Qiu, H. & Wang, F. "Pore-scale bodeling of pore structure effects on P-Wave scattering Attenuation in Dry Rocks." *PLOS ONE* **10**.4 (2015), pp. 1–15.

[109] Waterman, P. C. & Truell, R. "Multiple scattering of waves." *Journal of Mathematical Physics* **2**.4 (1961), pp. 512–537.

[110] Wear, K. A. "Ultrasonic scattering from cancellous bone: A review." *IEEE Transactions on Ultrasonics, Ferroelectrics and Frequency Control* **55**.7 (2008), pp. 1432–1441.

[111] Wear, K. A., Nagaraja, S., Dreher, M. L. & Gibson, S. L. "Relationships of quantitative ultrasound parameters with cancellous bone microstructure in human calcaneus in vitro." *The Journal of the Acoustical Society of America* **2**.131 (2012), pp. 1605 –1612.

[112] Wehrli, F. W., Song, H. K., Saha, P. K & Wright, A. C. "Quantitative MRI for the assessment of bone structure and function." *NMR in biomedicine* **19**.7 (2006), pp. 731–64.

[113] White, R. D., Alexanderian, A., Yousefian, O., Karbalaeisadegh, Y., Bekele-Maxwell, K., Kasali, A., Banks, H. T., Talmant, M., Grimal, Q. & Muller, M. "Using ultrasonic attenuation in cortical bone to infer distributions on pore size." *In preparation* (2021).

[114] White, R. D., Yousefian, O., Alexanderian, A., Banks, H. T. & Muller, M. "Inferring pore radius and density from ultrasonic attenuation using physics-based modeling." *Journal of the Acoustical Society of America* (2021).

[115] Williams, D. *Probability with martingales*. Cambridge university press, 1991.

[116] Yerramshetty, J. & Akkus, O. "Changes in cortical bone mineral and microstructure with aging and Osteoporosis." Springer, Berlin, Heidelberg, 2012, pp. 105–131.

[117] Ying, C. F. & Truell, R. "Scattering of a plane longitudinal wave by a spherical obstacle in an isotropically elastic solid." *Journal of Applied Physics* **27**.9 (1956), pp. 1086–1097.

[118] Yousefian, O., Karbalaeisadegh, Y. & Muller, M. "Modeling ultrasound attenuation in porous structures with mono-disperse random pore distributions using the independent scattering approximation: A 2D simulation study." *Physics in Medicine and Biology* **64**.15 (2019).

[119]   Yousefian, O., White, R. D., Karbalaeisadegh, Y., Banks, H. T. & Muller, M. "The effect of pore size and density on ultrasonic attenuation in porous structures with monodisperse random pore distribution: A two-dimensional in-silico study." *The Journal of the Acoustical Society of America* **144**.2 (2018), pp. 709–719.

[120]   Yousefian, O., White, R. D., Banks, H. T. & Muller, M. *Inferring Micro-Architecture from the Ultrasonic Attenuation in Cortical Bone.* Tech. rep. Raleigh, NC: Center for Research in Scientific Computation, N. C. State University, 2017.

[121]   Yousefian, O., White, R., Banks, H. T. & Muller, M. "Ultrasonic attenuation spectroscopy and dispersion characteristics in cortical bone." *2017 IEEE International Ultrasonics Symposium (IUS).* IEEE, 2017, pp. 1–4.

[122]   Zheng, R., Le, L. H., Sacchi, M. D., Ta, D. & Lou, E. "Spectral ratio method to estimate broadband ultrasound attenuation of cortical bones in vitro using multiple reflections." *Physics in medicine and biology* **52** (2007), pp. 5855–5869.

APPENDICES

APPENDIX

$$\text{A}$$

RELATIONSHIP BETWEEN ISA AND WT VIA THE OPTICAL THEOREM

Here we address the mathematical relationship between the ISA and the WT model formulations. The Optical Theorem [59] says

$$\gamma^{scatt} = \frac{-4\pi}{k_0} \text{Im}[f_0(\omega; r)], \tag{A.1}$$

where ω is frequency, r is radius, and k_0, γ^{scatt}, and f_0 were previously defined in (3.19) and (3.10). The ISA uses the following effective wavenumber approximation

$$k_{\text{eff}}^2 \approx k_0^2 + 4\pi n_s f_0(\omega; r). \tag{A.2}$$

We wish to show that $\frac{1}{2} n_s \gamma^{scatt}$ is an approximation to $-\text{Im}(k_{\text{eff}})$ up to a linearization. We thus need to show,

$$n_s \frac{2\pi}{k_0} \text{Im}[f_0(\omega; r)] \approx \text{Im}\left(k_0^2 + 4\pi n_s f_0(\omega; r) \right)^{1/2}. \tag{A.3}$$

Note the following Taylor Series approximation

$$(1+y)^{1/2} = 1 + \frac{y}{2} + \mathcal{O}(y^2). \tag{A.4}$$

83

Furthermore,

$$(k_0^2 + 4\pi n_s f_0(\omega; r))^{1/2} = k_0 \left(1 + n_s \frac{4\pi}{k_0^2} f_0(\omega; r)\right)^{1/2} \tag{A.5}$$

Equations (A.4) and (A.5) imply

$$k_0 \left(1 + \frac{4\pi}{k_0^2} n_s f_0(\omega; r)\right)^{1/2} \approx k_0 \left(1 + n_s \frac{2\pi}{k_0^2} f_0(\omega; r)\right) = k_0 + n_s \frac{2\pi}{k_0} f_0(\omega; r).$$

Thus, considering the right-hand side of (A.3)

$$\text{Im}(k_{\text{eff}}) = \text{Im}\left(k_0^2 + 4\pi n_s f_0(\omega; r)\right)^{1/2} \approx \text{Im}\left[k_0 + n_s \frac{2\pi}{k_0} f_0(\omega; r)\right],$$

and since k_0 is real,

$$\text{Im}\left[k_0 + n_s \frac{2\pi}{k_0} f_0(\omega; r)\right] = n_s \frac{2\pi}{k_0} \text{Im}[f_0(\omega; r)].$$

Thus, we have shown (A.3), up to a linearization as seen above.

APPENDIX

B

PENALTY FUNCTION DERIVATION

Here, we discuss the derivations of the three regularization functions given in Chapter 4, Section 4.4.3.

We begin with the penalization on the L^2 norm of the estimated PDF, which is given as

$$
\begin{aligned}
\int_{\Omega_{\mathrm{R}}} |f_n(r)|^2 dr &= \int_{\Omega_{\mathrm{R}}} f_n(r) \cdot f_n(r) dr = \int_{\Omega_{\mathrm{R}}} \sum_i \sum_j c_i c_j l_i(r) \cdot l_j(r) dr \\
&= \sum_i \sum_j c_i c_j \int_{\Omega_{\mathrm{R}}} l_i(r) \cdot l_j(r) dr, \quad i,j = 1, \ldots, n \\
&= \mathbf{c}^T \mathbf{M} \mathbf{c},
\end{aligned}
\tag{B.1}
$$

where $\mathbf{c} = [c_1 \ c_2 \ \ldots \ c_n]^T$ are the spline coefficients and $\mathbf{M}$ is known as the mass matrix whose entries are given by $M_{ij} = \int_{\Omega_{\mathrm{R}}} l_i(r) \cdot l_j(r) dr$. Let us determine the specific entries for the stiffness matrix in (B.1). Noting that if $|i - j| > 1$ then $l_i(r) \cdot l_j(r) = 0$ provides the following cases:

1.) i = j:

$$
\begin{aligned}
\int_{\Omega_{\mathrm{R}}} l_i(r) \cdot l_j(r) dr &= \int_{\Omega_{\mathrm{R}}} l_i(r) \cdot l_i(r) dr \\
&= \int_{r_{i-1}}^{r_i} \left(\frac{r - r_{i-1}}{h} \right) \left(\frac{r - r_{i-1}}{h} \right) dr + \int_{r_i}^{r_{i+1}} \left(\frac{r_{i+1} - r}{h} \right) \left(\frac{r_{i+1} - r}{h} \right) dr \\
&= \frac{1}{3}h + \frac{1}{3}h = \frac{2}{3}h
\end{aligned}
$$

2.) |i - j| = 1:

Without loss of generality, let $j = i + 1$ and thus,

$$\int_{\Omega_R} l_i(r) \cdot l_j(r) dr = \int_{\Omega_R} l_i(r) \cdot l_{i+1}(r) dr = \int_{r_i}^{r_{i+1}} \left(\frac{r_{i+1} - r}{h} \right) \left(\frac{r - r_{i-1}}{h} \right) dr = \frac{1}{6} h.$$

Therefore, we have the following mass matrix, where empty entires are zero

$$\mathbf{M} = h \begin{bmatrix} 2/3 & 1/6 & & \\ 1/6 & \ddots & \ddots & \\ & \ddots & \ddots & 1/6 \\ & & 1/6 & 2/3 \end{bmatrix}.$$

Thus, our L^2 regularization function is of the form

$$G_{l^2}(f_n) = \mathbf{c}^T \mathbf{M} \mathbf{c} \tag{B.2}$$

Next, we derive the penalty on the H^1 norm of the PDF given by

$$\begin{aligned} \int_{\Omega_R} |\nabla f_n(r)|^2 dr &= \int_{\Omega_R} \nabla f_n(r) \cdot \nabla f_n(r) dr \\ &= \sum_i \sum_j c_i c_j \int_{\Omega_R} \nabla l_i(r) \cdot \nabla l_j(r) dr, \quad i, j = 1, \ldots, n \\ &= \mathbf{c}^T \mathbf{K} \mathbf{c}, \end{aligned}$$

where here $\mathbf{K}$ is known as the stiffness matrix whose entries are given by $K_{ij} = \int_{\Omega_R} \nabla l_i(r) \cdot \nabla l_j(r) dr$. Note that for linear splines we have the following:

$$l_i'(r) = \begin{cases} \frac{1}{h}, & r \in [r_{i-1}, r_i] \\ \frac{-1}{h}, & r \in [r_i, r_{i+1}] \\ 0, & \text{elsewhere} \end{cases}$$

and therefore consider again the following cases:

1.) $i = j$

$$\begin{aligned} \int_{\Omega_R} \nabla l_i(r) \cdot \nabla l_j(r) dr &= \int_{\Omega_R} l_i'(r) \cdot l_i'(r) dr \\ &= \int_{r_{i-1}}^{r_i} \left(\frac{-1}{h} \right) \left(\frac{-1}{h} \right) dr + \int_{r_i}^{r_{i+1}} \left(\frac{1}{h} \right) \left(\frac{1}{h} \right) dr \\ &= \frac{1}{h} + \frac{1}{h} = \frac{2}{h} \end{aligned}$$

2.) $|i - j| = 1$ Again, without loss of generality consider $j = i + 1$

$$\begin{aligned}
\int_{\Omega_{\mathrm{R}}} \nabla l_i(r) \cdot \nabla l_j(r) dr &= \int_{\Omega_{\mathrm{R}}} l_i'(r) \cdot l_{i+1}'(r) dr \\
&= \int_{r_i}^{r_{i+1}} \left(\frac{1}{h}\right)\left(\frac{-1}{h}\right) dr \\
&= \frac{-1}{h}.
\end{aligned}$$

Thus, we have that the stiffness matrix is given by

$$\mathbf{K} = \frac{1}{h}
\begin{bmatrix}
2 & -1 & & \\
-1 & \ddots & \ddots & \\
& \ddots & \ddots & -1 \\
& & -1 & 2
\end{bmatrix}.$$

This provides the following regularization function

$$G_{h^1}(f_n) = \mathbf{c}^T \mathbf{K} \mathbf{c}.$$